Universidade do Vale do Paraíba
Instituto de Pesquisa e Desenvolvimento
Programa de Pós-Graduação em Astronomia e Física

Vera Yesutor Tsali-Brown

A STUDY OF TIDAL AND PLANETARY WAVES IN THE AMERICAN AND AFRICAN SECTORS

São José dos Campos, SP.
2022

Vera Yesutor Tsali-Brown

A STUDY OF TIDAL AND PLANETARY WAVES IN THE AMERICAN AND AFRICAN SECTORS

A thesis submitted to the Graduate Program in Physics and Astronomy at Universidade do Vale do Paraíba, as a complement to credits necessary to obtain the title of Doctor in Physics and Astronomy.

Supervisors: Drs. Paulo Roberto Fagundes and Valdir Gil Pillat.

São José dos Campos, SP.
2022

Fundação Valeparaibana de Ensino

BIBLIOTECA

TERMO DE AUTORIZAÇÃO DE DIVULGAÇÃO DA OBRA

Ficha catalográfica

Tsali-Brown, Vera Yesutor
A study of tidal and planetary waves in the American and African sectors / Vera Yesutor Tsali-Brown; orientador, Paulo Roberto Fagundes; co-orientador Valdir Gil Pillat. - São José dos Campos, SP, 2022.
1 CD-ROM, 158 p.

Tese (Doutorado) - Universidade do Vale do Paraíba, São José dos Campos. Programa de Pós-Graduação em Física e Astronomia.

Inclui referências

1. Física e Astronomia. 2. Tides. 3. Planetary waves. 4. Geomagnetic field. 5. Ionosonde data. I. Fagundes, Paulo Roberto, orient. II. Pillat, Valdir Gil , co-orient. III. Universidade do Vale do Paraíba. Programa de Pós-Graduação em Física e Astronomia. IV. Título.

Eu, Vera Yesutor Tsali-Brown, autor(a) da obra acima referenciada:

Autorizo a divulgação total ou parcial da obra impressa, digital ou fixada em outro tipo de mídia, bem como, a sua reprodução total ou parcial, devendo o usuário da reprodução atribuir os créditos ao autor da obra, citando a fonte.

Declaro, para todos os fins e efeitos de direito, que o Trabalho foi elaborado respeitando os princípios da moral e da ética e não violou qualquer direito de propriedade intelectual sob pena de responder civil, criminal, ética e profissionalmente por meus atos.

São José dos Campos, 13 de Março de 2023.

Vera Yesutor

Autor(a) da Obra

Data da defesa: 18 / 11 / 2022

VERA YESUTOR TSALI-BROWN

"A STUDY OF TIDAL AND PLANETARY WAVES IN THE AMERICAN AND AFRICAN SECTORS."

Tese aprovada como requisito parcial à obtenção do grau de Doutor, do Programa de Pós-Graduação em Física e Astronomia, do Instituto de Pesquisa e Desenvolvimento da Universidade do Vale do Paraíba, São José dos Campos, SP, pela seguinte banca examinadora:

Prof. Dr. Marcio Tadeu de Assis Honorato Muella	Marcio Tadeu de A. H. Muella
Prof. Dr. Paulo Roberto Fagundes	Paulo Roberto Fagundes
Prof. Dr. Valdir Gil Pillat	Valdir Gil Pillat
Prof. Dr. Alexandre Tardelli	Alexandre Tardelli
Prof.ª Dr.ª Ana Roberta da Silva Paulino - UEPB	Ana Roberta S. Paulino
Prof. Dr. Lourivaldo Mota Lima - UEPB	Lourivaldo Mota Lima

Prof.ª Dr.ª Lúcia Vieira

Diretora do IP&D – Univap

São José dos Campos, 18 de novembro de 2022.

DEDICATION

To my Mother ***Georgina Abra Afenyo*** *and Father* ***Emmanuel Brown Tsali*** *(of blessed memory)*

ACKNOWLEDGEMENTS

I would like to thank the Almighty God for His love, care, provision, guidance, and protection throughout the study.

I thank my supervisor, Dr. Paulo Roberto Fagundes for accepting me as a student and guiding me. It has been an opportunity of a lifetime. You are one of a kind supervisor.

To my co-supervisor, Dr. Valdir Gil Pillat for his guidance, comments, and suggestions which gave substance to the work.

To the State of São Paulo Research Foundation, FAPESP, for the financial and institutional support through process number **2018/10679-4**.

To Universidade do Vale do Paraíba, UNIVAP, for allowing me to enroll in the doctoral program in Physics and Astronomy.

To the board of examiners who took time off their busy schedules to vet and scrutinize this work. Your comments and suggestions made this work better.

To the lecturers and students of the Physics and Astronomy group of UNIVAP.

To my dear friends/sisters Semefa, Samilia, Phoebe, Esi Pentsiwa, and Eunice and all my dear friends/family in Brazil who have supported me in diverse ways.

To Pastor Bismark Nyamekye and Miss Mawulorm Adzo Adika.

To my brother-in-law Mr. Mohammed Sayuti Nyassor who took time off his busy schedule to sit through a mock defense with me. Thank you for your time and input.

To my siblings Fo Dodzi, Ernest, Evans, Gideon, Dominic, and Emmanuella. You have all been supportive and have cheered me on.

To my dear father Emmanuel Brown Tsali (of blessed memory) who was excited at his daughter beginning her Ph.D. but sadly he was not around to see it becoming a reality. Daddy by God's Grace, your daughter made it. Glory to God.

To my dearest mother Georgina Abra Afenyo who has been my support and biggest cheerleader like no other. Always encouraging me anytime I run out of steam.

A special thanks to my dearest husband Prosper Kwamla Nyassor (Ph.D.) who has been there to help me from start to finish of this work. You have been and are a great support to me.

*The fear of the **LORD** is the beginning of wisdom, and the knowledge of the **Holy One** is understanding.*

(Proverbs 9:10 NKJV)

A STUDY OF TIDAL AND PLANETARY WAVES IN THE AMERICAN AND AFRICAN SECTORS

ABSTRACT

Observed data were obtained from magnetometers measuring the horizontal field intensity H(nT) of the geomagnetic field in the American and African sectors. These magnetometers were located in São José dos Campos, Eusébio, and São Luís, in the American Sector and Tamanrasset, Hermanus, and Tsumeb in the African sector. The datasets were analyzed and periods relating to solar and lunar tidal oscillations were extracted using the least square fit method. Results showed the presence of solar tidal oscillations (diurnal, semidiurnal, and terdiurnal) and semidiurnal lunar tidal oscillations present in both sectors. The latitudinal response of the three solar tidal components at three stations to the sudden stratospheric warming (SSW) of 2018 was also studied. It was observed that the low latitude station nearest the geomagnetic equator presented enhancements in the three components during the event. However, an anomaly was observed in the semidiurnal lunar tide in the African sector which could not be explained. Furthermore, wavelike oscillations between 3 to 32 days and relating to planetary waves were observed in the geomagnetic field. These wavelike oscillations between 3 to 32 days were also seen in the virtual height (h′F) of the ionosphere measured by ionosondes located at São José dos Campos and Araguatins in the American sector. PW results in the ΔH were in good agreement with the F10.7 solar flux. Additionally, during the geomagnetic storm of September 7-11, 2017, ΔH component variations in the American and African sectors (selected stations) showed different responses suggesting the presence of longitudinal dependence.

Keywords: tides; planetary waves; geomagnetic field; ionosonde data; SSW.

RESUMO

Os dados observados foram obtidos de magnetômetros que medem a intensidade do campo horizontal H(nT) do campo geomagnético nos setores americano e africano. Esses magnetômetros estão localizados no setor americano (São José dos Campos, Eusébio e São Luís) e no setor africano (Tamanrasset, Hermanus e Tsumeb). Deste conjunto de dados foi analisado e extraído, usando o método de ajuste de mínimos quadrados, os períodos relativos às oscilações de maré solar e lunar. Os resultados mostraram a presença de oscilações de maré solar (diurnas, semidiurnas e terdiurnas) e oscilações de maré lunar semidiurnas presentes em ambos os setores. Também foi apresentada a resposta latitudinal das três componentes de maré solar ao aquecimento estratosférico súbito (SSW) de 2018 nas estações selecionadas. Durante o evento observou-se que a estação de baixa latitude mais próxima do equador geomagnético apresentou aumento nas três componentes. No entanto, foi observada uma anomalia na maré lunar semidiurna no setor africano que não pôde ser explicada. Além disso, oscilações ondulatórias entre 3 e 32 dias e relacionadas a ondas planetárias (PW) foram observadas no campo geomagnético. Essas oscilações ondulatórias entre 3 e 32 dias também foram observadas na altura virtual (h´F) da ionosfera medida por ionossondas localizadas no setor americano (São José dos Campos e Araguatins). Os resultados de PW no ΔH estavam em boa concordância com o fluxo solar F10.7. Adicionalmente foi apresentada a variação do componente ΔH nos setores americano e africano (em estações selecionadas) durante a tempestade geomagnética de 7-11 de setembro de 2017 mostrando respostas diferentes nos setores, sugerindo a presença de uma dependência longitudinal.

Palavras-chave: marés; ondas planetárias; PRE; campo geomagnético; dados de ionossonda; SSW.

LIST OF FIGURES

LIST OF TABLES

LIST OF ABBREVIATIONS AND ACRONYMS

AFR - African

ARA - Araguantins

BEL - Belém

BRL - Brazilian

CXP - Cachoeira Paulista

CADI - Canadian Advanced Digital Ionosonde

COI - Cone of influence

CUI - Cuiaba

DOY - Day of Year

Dst - Disturbance Storm Time

DT - Disturbed Time

EMBRACE - Programa De Estudo e Monitoramento Brasileiro De Clima Espacial

EIA - Equatorial Ionization Anomaly

EUS - Eusebio

EUV - Extreme ultraviolet

HBK - Hartebeesthoek

HER - Hermanus

HF - High Frequency

IMO - INTERMAGNET Magnetic Observatories

INTERMAGNET - International Real-Time Magnetic Observatory Network

Kp - Planetarishe Kennziffer /Planetary index

L-S - Lomb-Scargle

LT - Local Time

LTE - Laplace's tidal equation

MBO - Mbour

MLT - Mesosphere and Lower thermosphere

nT - Nano Tesla

PRE - Pre-reversal Enhancement

PWs - Planetary Waves

QDW - Quasi Day Wave

QT - Quiet Time

SABER - Sounding of the Atmosphere using Broadband Emission Radiometry

SJC - São José dos Campos

SLT - Semidiurnal Lunar Tide

SLZ - São Luís

SSC - Sudden Storm Commencement

SSW - Sudden Stratosphere Warming

STC - Solar Tidal Components

SW1 - Semidiurnal tide with wavenumber 1

TAM - Tamanrasset

TIMED - Thermosphere, Ionosphere, Mesosphere Energetics and Dynamics

TSU - Tsumeb

UDIDA - UNIVAP Digital Ionosonde Data Analysis

UNIVAP - Universidade do Vale do Paraíba

UT - Universal Time

WPS - Wavelet Power Spectrum

LIST OF SYMBOLS

B	-	Magnetic field
c_p	-	Specific heat at constant pressure
c_v	-	Specific heat at constant volume
C^2	-	Square of the velocity of sound in the atmosphere
e	-	Charge of an electron
ϵ	-	Lamb's parameter
ϵ_0	-	Permissibility constant in the vacuum
ζ	-	Relative vorticity
f	-	Coriolis parameters
f_o	-	Basic state
f'	-	Tidal contribution
f_*	-	Normalized frequency
$\vec{F}$	-	The external force
$\vec{g}$	-	Acceleration due to gravity
H	-	Scale height
ΔH	-	Horizontal geomagnetic field intensity
J	-	Thermal excitation function
K_G	-	Coefficient of absorption
K_1	-	Diurnal lunar-solar
K_2	-	Semidiurnal lunar-solar
m_e	-	Mass of the electron
M_2	-	Semidiurnal lunar
n	-	Sample size
n_e	-	Number of electrons
N_2	-	Elliptical lunar semidiurnal
λ	-	Longitude
O_1	-	Quasi diurnal lunar
ϕ	-	Longitude or latitude
σ	-	Frequency of oscillation
Ω	-	Tidal gravitational potential
P	-	Pressure

ρ	-	Density
p	-	Pressure
P_1	-	Quasi diurnal solar
φ_1	-	Diurnal phase
φ_2	-	Semidiurnal phase
φ_3	-	Terdiurnal phase
R	-	Distance from Earth's center
r	-	Gas Constant
s	-	Sample standard deviation
S_2	-	Semidiurnal solar
T	-	Temperature
T_o	-	Basic temperature distribution
t	-	Time in solar hours
τ	-	Time in lunar hours
u	-	Zonal velocity
v	-	Meridional velocity
w	-	Vertical velocity
ω	-	Frequency
$\vec{\omega}$	-	Angular rotation of the earth
γ	-	Gravitational constant
z	-	Altitude

TABLE OF CONTENTS

1 INTRODUCTION

1.1 General Overview

The region of the Earth's atmosphere where the concentration of free electrons is such that it affects radio waves is known as the ionosphere. This region is formed when electromagnetic and particle radiations from the Sun and space ionize air molecules, creating plasma in the upper atmosphere. However, this plasma is weakly ionized even at altitudes where the number of electrons (n_e) reaches its maximum. The ionosphere is divided into different regions based on the vertical distribution of its electronic density however, the regions are not visibly distinct, but depend on the densities and processes that occur in these regions. They are the D, E, and F regions. The D region is approximately between the altitudes of 60 and 100 km but can descend to around 50 km during intense solar activity. The E region is between 90 km to 150 km altitude during the day. The F region extends from about 150 km to more than 500 km above the Earth's surface and consists of two layers, F1 layer at daytime and F2 layer at nighttime. The F1 layer is the lower part of the F region and lies between 150 and 220 km in altitude. This layer is only present during the daytime because it merges with the F2 layer at nighttime. The F2 layer lies at an altitude of 220 to 800 km. The behavior of the F region is generally dominated by complex thermospheric winds.

The state of the upper atmosphere and ionosphere is known to be influenced and affected by solar activity (KUTIEV et al., 2013; PRÖLSS, 2011 and references therein), magnetospheric and geomagnetic processes/activities (coupling from above or simply space weather) (DENARDINI et al., 2020; XIONG et al., 2006; YIĞIT, 2017), and also meteorological processes from below (coupling from below) (YIĞIT, 2017; YIĞIT et al., 2016). Atmospheric waves (such as planetary, tidal, gravity waves, TIDs, and MSTIDs) generated in the lower atmosphere are the main drivers of the coupling processes from below (YIĞIT, 2017). These generated waves play an important role in determining large-scale circulation (HUANG et al., 2013) and affecting the structure and evolution of the upper atmosphere–ionosphere system (YIĞIT, 2017). As they propagate upward, they convey energy and momentum from their source regions in the lower atmosphere leading to a global redistribution of atmospheric energy and momentum and coupling among various atmospheric layers (HUANG et al., 2013). Atmospheric tides, one of the generated waves from the lower atmosphere are known to modulate and cause day-to-day variabilities in this region.

Tides are global-scale oscillations in wind, temperature, pressure, and density at periods that are subharmonics of a solar or lunar day (FORBES, 1995). Hence, they are waves with well-defined fundamental periods of one solar (or lunar) day (VOLLAND, 1988) or one year with periods that are some integer fraction of a solar or lunar day. The solar diurnal and semidiurnal tides have 24 and 12 h periods, respectively, whereas, the lunar diurnal and semidiurnal tides have 24.8 and 12.4 h periods respectively (OBERHEIDE et al., 2015). They are one of the many physical processes that influence the background characteristics of the thermosphere-ionosphere system and are an ever-present feature in the atmosphere. Generally, tides could propagate either eastwards or westwards. However, the westward propagating or those migrating with the apparent motion of the sun or moon are known to have the largest components (FORBES, 1995). They are also directly or indirectly excited by solar thermal, orographic, and lunar gravitational forcing (VOLLAND, 1988). Due to the dynamics of the atmosphere-ionosphere system, tidal waves interact and couple with other waveforms and features such as planetary waves.

Planetary waves are global-scale oscillations of atmospheric circulation (LAŠTOVIČKA et al., 2003), which extend coherently around a full longitude circle (SMITH; PERLWITZ, 2015) and occur in rotating fluids (BEER, 1974). They have wavelike perturbations in the longitudinal and vertical directions and in the latitudinal direction (SMITH; PERLWITZ, 2015), with dominant zonal wavenumbers of one, two, and three of periods from 2 to 30 days (FAGUNDES et al., 2005 and references therein). PWs usually originate from the troposphere and are stationary or transient by nature (LAŠTOVIČKA et al., 2003). However, in the ionosphere, oscillations with planetary wave periods have been observed although they usually are not able to penetrate to altitudes above the lowermost thermosphere (JACOBI et al., 2007). Hence, these oscillations could originate from planetary waves travelling from below, periodic geomagnetic activity, and sometimes even of unknown origin (FAGUNDES et al., 2005). Laštovička (2006), has also indicated that planetary waves can propagate upwards to the F region heights only indirectly, through various potential ways such as the modulation of upward propagating tides. Other studies (see, examples ABDU et al., 2006; PANCHEVA et al., 2003; PANCHEVA; ALBERCA; LA MORENA, 1994) have also proposed the mechanism for indirect upward transport of the planetary wave-type oscillations into the ionospheric F-region through nonlinear processes. Observational and modeling investigations have demonstrated how planetary waves (PWs) propagate from the lower atmosphere into the dynamo region, where they impose their variability throughout the F region of the ionosphere (ELHAWARY; FORBES, 2016 and references therein).

Laštovička (1997) observed tidal and planetary waves in the atmosphere-ionosphere system. In this study, planetary wave-type oscillations were observed at the F2-region maximum heights, although planetary waves of tropospheric origin detected in the middle atmosphere and lower ionosphere is unable to propagate efficiently deep into the thermosphere. Kohsiek et al. (1995) studied periods of planetary waves in geomagnetic variations. PW periods of 10- and 16-day waves were found in the Fourier analyses of 10-year geomagnetic time series from two mid-latitude stations in the northern hemisphere. (FORBES; LEVERONI, 1992) observed and studied quasi-16-day oscillations in the ionosphere using the magnetometer. Gurubaran and Rajaram (2000) also studied signatures of quasi-2-day planetary waves in the equatorial Electrojet using medium frequency radar and ground-based magnetometers and found a reasonable correlation between the occurrence times of the quasi-2-day oscillation in the EEJ strength and the mesospheric winds.

1.2 Motivation

Planetary and tidal waves are part of the main physical processes that influence the background characteristics of the thermosphere-ionosphere system. They do so by dumping their momentum into the mean flow as they dissipate and by affecting the wind dynamo in the E-region. Hence, they aid in facilitating the vertical coupling between the neutral atmosphere and the ionosphere. They also transport energy and momentum in the atmosphere/ionosphere. However, during geomagnetic quiet and disturbed days, the response and behavior of these waves in the atmosphere/ionosphere tend to change/vary. It is therefore important to study these changes/variations in order to understand how the coupling process is affected during these days. This research is therefore to study atmospheric tides, planetary waves, and their behavior in the ionosphere over the Brazilian and African sectors during geomagnetic disturbed (storm) and quiet days and during an SSW event. This study will help us gain more understanding into the behavior of these waves during both periods and the response of the ionosphere during such days.

1.3 Objective

The main objective of this doctoral work is to study tidal (solar and lunar) and planetary waves in the ionosphere in the American and African sectors, using magnetometer and ionosonde data from selected stations located in both sectors.

1.3.1 Specific Objectives

The specific objectives of this work are to study the:

- Solar tides present in the ionosphere over the Brazilian and African sectors during geomagnetic disturbed and quiet days and their behavior;
- latitudinal response of solar tidal components to the SSW event of February 2018;
- lunar tides (semidiurnal) present in the ionosphere over the Brazilian and African sectors during geomagnetic disturbed and quiet days and their behavior;
- planetary wave-type periods present in the ionosphere over the Brazilian and African sectors during the daytime and PRE;
- solar tidal response in the ionosphere to the September 7-11, 2017 intense geomagnetic storm.

1.4 Chapter Organization

The organization of the chapters in this work are as follows:

- Chapter 2 presents a description of the classical theory of tides. Solar and Lunar excitation function. Furthermore, the planetary wave theory and excitation are looked at. This chapter also presents the bibliographical review where the main features of the solar and lunar tides and planetary waves are presented;
- Chapter 3 presents a summarized presentation of the instruments used and the database used;
- Chapter 4 gives and describes the step-by-step methodology used in this work;
- Chapter 5 presents the results obtained and the discussion;
- Chapter 6 gives the conclusions and suggestions for future work;
- References and Appendix.

2 TIDES AND PLANETARY WAVES

This chapter will describe the theory governing tides taking into consideration solar and lunar tides and discuss the theory governing planetary waves. The characteristics of both waveforms are also presented.

2.1 Classical Theory of Tides

The study of tides began with ocean tides. In 1687, Newton theorized that tides are a consequence of lunar and solar gravitational forces obeying the three laws of mechanics. Hence, tides can be said to be due to the differences between gravitational and centrifugal forces. Both Newton and Laplace also believed that tidal forces must affect the atmosphere as well since the atmosphere can be considered a fluid but thought atmospheric tides even if they occurred would be too small to be detected (CHAPMAN; LINDZEN, 1969). To develop the theory of atmospheric tides, Laplace's theory was adapted although his theory was developed for an incomprehensible fluid. However, for the atmosphere, which can be said to be compressible (PAULINO, 2013), some boundary conditions can be applied. Generally, this theory has been developed through the contributions of various scientists (LAPLACE, 1799; NEWTON, 1687; RAYLEIGH, 1890; THOMSON, 1882). The theory of atmospheric tides, therefore, aims to investigate the sources of periodic excitation, and estimate the atmospheric response to the excitation (CHAPMAN; LINDZEN, 1969). The sources of the excitation could be gravitational or thermal. As pointed out by Chapman and Lindzen (1969), the study of the atmospheric response to the excitations could include a detailed consideration of atmospheric composition and chemistry, solar spectrum, molecular absorption, radiative transfer, turbulent transfer and could in principle concern all problems involved in the general circulation of the atmosphere (includes non-adiabatic, orographic, non-linear, hydromagnetic and numerous other types of processes). This set of considerations gives rise to complex equations. The set of governing equations here are adapted from various researchers (BEER, 1974; CHAPMAN; LINDZEN, 1969; NYASSOR, 2021; PAULINO, 2013).

To develop the theory, the following approximations and assumptions are universally applied:

i. The atmosphere is considered as a compressible gas hence, it is convenient to express the equations in spherical coordinates for a frame of reference rotating with the earth.

ii. The atmosphere is in local thermodynamic equilibrium, therefore, it responds to heating through a continuous sequence of equilibrium state,

iii. Supposing the atmosphere is a perfect gas and homogeneous, it obeys the basic gas law, $p = \rho RT$, where p is pressure, ρ is density, R is the gas constant and T is temperature,

iv. The atmosphere is considered as a geometrically thin fluid layer of small thickness compared with the radius of the earth, *a,* thus the approximation for the shallow atmosphere can be expressed as $r = a + z$, where $z << a$, r is the distance from the earth's center and is the z is the altitude,

v. The earth's ellipticity surface topography are ignored. Hence, the influence of mountains and land-sea distributions are not taken into account.

vi. The dissipative processes and their effects such as ion drag and infrared radiative transfer and conductivity, molecular and turbulent viscosity are ignored.

vii. Tidal fields are regarded as perturbations which can be linearized about some basic state. This is given by $f = f_o + f'$, where f_o is the basic state and f' is the tidal contribution to f . Also, for the tidal equations to be easy to deal with, two assumptions are made; a) the basic field is assumed to be steady and b) basic flow may be set to zero and are independent of latitude and longitude hence T_0 (basic temperature distribution), p_0 and ρ_0 are defined by $p_0 = p_0(0)e^{-x}$, $\rho_0 = \frac{p_0}{gH}$, where $H = \frac{RT_0}{g}$ is the scale height and $x = \int_0^z \frac{dz}{H}$ is the reduced height.

2.1.1 Set of Basic Equations

Atmospheric motions are governed by a set of basic equations. These equations are employed in the development of the tidal theory. These are equation of the conservation of mass or the conservation of mass continuity, conservation of momentum, and conservation of energy. The continuity equation is given by:

$$\frac{D\rho}{Dt} + \rho\nabla.\vec{V} = 0 \qquad (1)$$

Where, $\frac{D}{Dt} = \frac{\partial}{\partial t} + \vec{V}.\nabla$ is the Eulerian derivative, ∇ is the gradient operator (but when ∇ is $\vec{\nabla}$, it is written in the spherical coordinates as $\frac{\partial}{\partial z}\hat{z} + \frac{1}{a}\frac{\partial}{\partial \theta}\hat{\theta} + \frac{1}{asin\phi}\frac{\partial}{\partial \phi}\hat{\phi}$, ρ is the density of the fluid and $\vec{V}$ = (*u, v, w*), where *u, v, w,* are the zonal, meridional, and vertical velocities, respectively.

The continuity equation shows that the substantive change in the mass of the fluid per volume unit is equal to the advection of the fluid, that is, the mass of the fluid has neither source (generation point) nor sink (dissipation point). Please refer to (GOSSARD; HOOKE, 1975) for more details regarding the mathematical description of the continuity equation as well as the main forces that act in the atmosphere. The next equation is the conservation of momentum given by:

$$\frac{D\vec{V}}{Dt} + 2\left(\vec{\omega} \times \vec{V}\right) = -\frac{1}{\rho}\nabla P + \vec{g} + \vec{F} \qquad (2)$$

finally, the equation of conservation of energy is given by:

$$\frac{DP}{Dt} - C^2\frac{D\rho}{Dt} = (\gamma\text{-}1)\rho^J \qquad (3)$$

where, P is the pressure, J is the thermal excitation function, $\vec{g}$ is the acceleration due to gravity, $\vec{\omega}$ is the angular rotation of the earth, $\vec{F}$ is the external force, $\gamma = c_p/c_v$ (c_p is specific heat at constant pressure and c_v is the specific heat at constant volume and C^2 $C^2 = \gamma RT$ is the square of the velocity of sound in the atmosphere.

After several mathematical assumptions and substitutions, we arrive at:

$$\frac{dy_n}{dx} + \left(\frac{H}{h_n} - \frac{1}{2}\right)y_n = \frac{i\sigma}{\gamma g h_n}\Omega_n \qquad (4)$$

For further details on the theory, refer to Chapman and Lindzen (1969) and Paulino (2013).

2.2 Solar Tides

Solar tides originate through two major thermal excitation processes, thus, thermal excitation due to;

i. exchange of heat with the ground and
ii. direct atmospheric absorption of insolation.

Brief descriptions of the each of the thermal excitation mechanism are given in the subsequent sections.

2.2.1 Thermal Excitation Due to Exchange of Heat with the Ground

The majority of the incident solar radiation on the Earth and it's atmosphere are absorbed by the ground and sea. The daily cycle of the sun causes daily heating and cooling of the ground, thereby causing daily variation of the ground temperature to be conveyed to the adjacent by radiative (turbulence and infrared) transfer. Various researchers (BRUNT, 2011; GOODY, 1960; KONDRAT'YEV, 2013; KUO, 1968) have studied the exact transfer mechanism. However, most of these studies ignored the response of the atmosphere to the transferred heat since the solution obtained from these studies had temperature oscillations decaying with altitude. Even though this heating can excite oscillations that the atmosphere will transmit upward with a growing amplitude of a factor of yet, this is ignored. Chapman (1924) was the first to estimate the omission of the oscillation of the heating. He later calculated the transfer of the temperature oscillation by neglecting the large-scale dynamic response, after which he derived a heating function that produced this oscillation. The estimation of the heating function approach considered the transport of surface temperature oscillation to the atmosphere by turbulence where the turbulent transfer is modelled by eddy diffusion with the eddy *K* conductivity taken as a constant and no horizontal diffusion. The temperature is then given by

$$\frac{\partial T}{\partial t} = \frac{K\partial^2 T}{\partial z^2}, \tag{5}$$

Where, $T = T_0^{\sigma,S}(\theta)e^{i(\sigma t + s\phi)}$ at $z = 0$. Since Equation 5 does not involve θ explicitly, it has the solution

$$T_n^{\sigma,S} = Ae^{-kz} + Be^{+kz} \tag{6}$$

Where, $k = \sqrt{\sigma/K}\ e^{\phi i/4}$. Assuming that there is no heat flux from above, $B = 0;\ A = T_n(0)$. Then

$$T_n = T_n(0)e^{-kz}. \tag{7}$$

By writing

$$\partial T_n/\partial t = J_n/c_p \tag{8}$$

Then J_n that would give rise to

$$J_n = i\sigma c_p\, T_n(0)\, e^{-kz}\, e^{i(\sigma t + s\phi)} \tag{9}$$

Equation 9 is then used in

$H\frac{d^2L_n^{\sigma,S}}{dz^2} + \left(\frac{dH}{dz} - 1\right)\frac{dL_n^{\sigma,S}}{dz} + \frac{1}{h_n^{\sigma,S}}\left(\frac{dH}{dz} + K\right)L_n^{\sigma,S} = \frac{K}{\gamma g H h_n^{\sigma,S}} J_n^{\sigma,S}$ to retrieve the atmospheric tidal response to the surface heating.

Chapman (1924), Siebert (1961), and Kertz (1956) employed this method in series of estimations and found that surface temperature oscillations excite negligible migrating thermal tides in the surface pressure. Strong oscillations, on the other hand, in the wind and temperature were generated.

2.2.2 Thermal Excitation Due to Direct Atmospheric Absorption of Insolation

Even though most of the incident sunlight insolation is absorbed at the ground, a significant quantity is absorbed in the atmosphere by water vapor, ozone, and O_2 (to a lesser extent). The daily variation in the heating due to this absorption is distributed throughout a large volume of the atmosphere. This absorption is the most important mechanism of tidal and thermotidal excitation.

Considering a gas, G, with a density distribution given as $\varrho_G(\theta, \phi, z, t)$ and whose coefficient of absorption as a function of wavelength is $K_G(\lambda)$,[1] then the heating due to absorption by G, J_G, is given by

$$J_G\,(z, \theta, \phi, t) = \frac{\varrho_G}{\varrho}\int d\lambda\, K_G(\lambda) I_{0,\lambda}\, e^{(-K_G\,(\lambda)\int \varrho_G\, ds')} \tag{10}$$

Here the first integration is over all the absorption bands of G; $I_{0,\lambda}$ is the intensity of radiation of wavelength, λ, incident on the atmosphere; s is the distance from the sun.

During the day, J_G is non-zero, that is, when

$$0 \le |\phi| \le cos^{-1}\left(-\frac{\tan\alpha}{\cot\theta}\right) = \phi_{max}. \tag{11}$$

[1] K_G may be temperature and pressure dependent.

where α represents the angle between the earth's axis and the normal to the plane of the ecliptic (BUTLER; SMALL, 1963). In this case, $I_{0,\lambda}$ is as a function of local time, that is; $I_{0,\lambda} = I_{0,\lambda}\ (\sigma t + \phi)$, where $\sigma = 2\pi/1\ solar\ day$. If time and longitude dependence of ϱ and ϱ_G are neglected, then

$$J_G(x, \theta, \phi, t) = J_G(z, \theta, \sigma t + \phi).$$

Considering Equations 10 and 11, J_G can be expanded as

$$J_G = Re \sum_{n=0}^{\infty} J_G^{n\sigma,s}(z, \theta)\, e^{int'} \tag{12}$$

Where, $t' = \sigma t + \phi$, and the $\{J_G^{n\sigma,s}(z, \theta)\}$ can be complex. The term in Equation 12 for which $n = 0$ corresponds to the steady component of the heating. The atmosphere is assumed to be in a state of quasi-equilibrium wherein there are constant (in time) cooling processes which exactly balance, $J_G^{0,0}$.

In this excitation mechanism, among others only H_2O and O_3 absorption are considered. Sometimes, it is convenient to use $\tau_G^{\sigma,s} = \kappa J_G^{\sigma,s}/i\sigma R$ instead of $J^{\sigma,s}$. Employing similar procedure in Section 2.2.1, $\tau^{\sigma,s}$ corresponds to the temperature oscillation that would be produced by $J_G^{\sigma,s}$ if the dynamic response of the atmosphere were ignored.

Based on some researches, (e.g,, BUTLER; SMALL, 1963; LEOVY, 1964; LINDZEN, 1967; SIEBERT, 1961), *J*'s can be separated into their latitude and altitude dependence; thus

$$\tau = \sum_G \sum_{n=1}^{\infty} \tau_G^{n\sigma,n}(z, \theta) e^{int'}, \tag{13}$$

Where

$$\tau_G^{\sigma,s} = f_G^{\sigma,s}(z) g_G^{\sigma,s}(\theta). \tag{14}$$

These tidal structures are primarily excited through the absorption of solar radiation by water vapor in the troposphere and by ozone in the stratosphere. They experience considerable growth with altitude and achieve their maximum amplitudes in the Mesosphere-Lower Thermosphere (MLT). Because these motions become large at comparable altitudes, they are

also subject to strong mutual interactions with other waveforms, which have important implications, and for the MLT (FRITTS, 1995).

2.3 Lunar Tides

In this section, we address the gravitational excitation mechanism of lunar tides. The lunar tide is mainly generated by the gravitational attraction force of the moon (YAMAZAKI; MAUTE, 2017) acting on the earth-ocean-atmosphere system, with secondary contributions from the gravitational attraction of the Sun.

2.3.1 Gravitational Excitation

The lunar tide forcing can be obtained by the following potential:

$$\Omega = -\frac{3}{2}\frac{\gamma M a^2}{D^3}\left[\frac{3}{2}\left(cos^2\Delta - \frac{1}{3}\right)\left(cos^2\theta - \frac{1}{3}\right) + \frac{1}{2}sin2\Delta sin2\theta\cos(\alpha + \phi) + \frac{1}{2}sin^2\Delta sin^2\theta cos2(\alpha + \phi)\right]. \quad (15)$$

in that, γ is the gravitational constant, M denotes the mass of the moon or the sun, a is the distance between center of the Earth and the point P (as shown in Figure 1), D is the distance between the center of the Earth and the center of the moon and the sun (see Figure 1), α is the hour angle, ϕ is the longitude of point P and Δ is the angle of the moon from the north. Lamb (1932) developed the potential described in Equation 15.

Figure 1 - Geometry used to calculate the tide potentials. O is the center of the Earth; C is the center of the Moon or Sun.

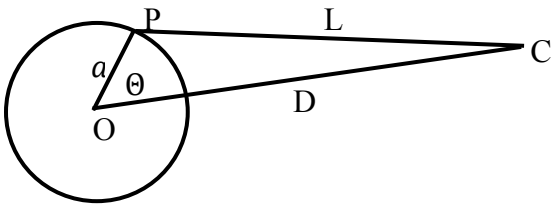

Source: Paulino (2013)

The lunar semidiurnal tidal potential, also known as M_2, is the one with the greatest amplitude among all the tides generated due to the gravitational potential of the Earth and the

Moon. Assuming that the Moon's orbit around the Earth is a perfect circle and is on the same plane as the Earth's equator, the gravitational potential would generate only the semidiurnal component.

However, the Moon's orbit has a small eccentricity and an angle with respect to the plane of the Earth's equator. Therefore, the semidiurnal component is not the only one generated by this force. A similar reasoning can be applied to the case of the gravitational attraction of the Sun in relation to the Earth. Doodson (1921) studied the gravitational potential in detail and, based on this work, Siebert (1961) calculated the periodicities produced by both gravitational potentials. Table 1 describes the main periodicities with potential data in cm^2/s^2:

Table 1 - Main periodicities produced by gravitational potentials.

Tide	**Description**	**Period (hours)**	**Potential (cm^2/s^2)**
O_1	Quasi diurnal lunar	25.819	$-6585.N_2^1(\theta)\sin[(\sigma_0 - 2\sigma_1^L)t + \phi]$
P_1	Quasi diurnal solar	24.04	$-3067.N_2^1(\theta)\sin[(\sigma_0 - 2\sigma_1^L)t + \phi]$
K_1	Diurnal lunar-solar	23.934	$-9268.N_2^1(\theta)\sin(\sigma_0 t - \phi)$
N_2	Elliptical lunar semidiurnal	12.66	$-1518.N_2^2(\theta)\cos[(2\sigma_2^L - \sigma_1^S + \nu)t + 2\phi]$
M_2	Semidiurnal lunar	12.42	$-7933.N_2^2(\theta)\cos[(2\sigma_2^L t + \phi)]$
S_2	Semidiurnal solar	12.00	$-3700.N_2^2(\theta)\cos[(2\sigma_2^S t + \phi)]$
K_2	Semidiurnal lunar-solar	11.97	$-1005.N_2^2(\theta)\cos[(2\sigma_0 t + \phi)]$

Source: Paulino (2013)

In These Expressions, We Have:

$$\sigma_0 = \frac{2\pi}{1\ dia\ sidereal}, \tag{16}$$

$$\sigma_1^L = \frac{2\pi}{1\ lunar\ month}, \tag{17}$$

$$\sigma_1^S = \frac{2\pi}{1\ sidereal\ year}, \tag{18}$$

Where σ_2^L is the angular rotation rate of the Earth around itself with respect to the moon and is given by $\sigma_2^L = \sigma_0 - \sigma_1^L$ and with respect to the sun is $\sigma_2^S = \sigma_0 - \sigma_1^S$. The terms $N_2^1(\theta) = \frac{3}{2}sin2\theta$ and $N_2^2(\theta) = 3sin2\theta$ are the associated Legendre polynomial, t is the time in universal hour and ϕ is the longitude. More information on the gravitational excitation mechanism can be obtained in Chapman and Lindzen (1969).

N_2 is the principal harmonic that depend on the variation of the distance between the moon and earth. Bartels and Johnston (1940) verified the presence of this oscillation in graphical data.

Considering only the symmetrical modes, the gravitational potential expansion for the lunar tidal and semidiurnal becomes:

$$\Omega = (-2366.\Theta_2 - 5615.\Theta_4 - 2603\Theta_6 \ldots\ldots)\cos\,(2(\sigma_2^L t + \phi)) \quad (19)$$

Where Θ_n is the Hough function for each n.

As with the solar semidiurnal tidal oscillation, most of the excitation of the lunar semidiurnal tidal oscillation is concentrated in mode 2. In the case of gravitational tides, the excitation function due to solar absorption is taken equal to zero and Equation 4 then becomes homogeneous. The excitation function only enters the boundary condition of Equation 4, thus, the excitation of gravitational tide is concentrated in only one level.

Variations of tides in atmospheric fields can be represented mathematically as follows:

$$A_{n,s}\cos\big(n\Omega t - s\lambda - \phi_{n,s}\big). \quad (20)$$

with t being the time in days (universal time), $\Omega = 2\pi/day$ the rate of rotation of the Earth, λ the longitude, zonal wave number[2], n denotes the subharmonics of a day Lunar or Solar, that is, $n = 1$ corresponds to the diurnal tide, $n = 2$ to the semidiurnal tide, $n = 3$ to the terdiurnal tide and so on. $A_{n,s}$ (Amplitude) and $\phi_{n,s}$ (phase) are functions of altitude and latitude. At each altitude and latitude, the tidal response is obtained by summing over n and s. Furthermore, in this equation, the tides can be considered propagating westward ($s > 0$), eastward ($s < 0$) and trapped ($s = 0$).

2.4 Planetary waves

Planetary waves influence the thermosphere-ionosphere system by modulating the E-region and F-region dynamo electric fields. The dissipation of planetary waves in the lower thermosphere, on the other hand, modifies the background winds, and induces extra meridional circulation, consequently altering thermospheric constituents, such as O/N_2, and ionospheric electron densities. Planetary waves are classified into three: (i) quasi-stationary midlatitude Rossby waves, (ii) normal modes, and (iii) equatorial waves (PAULINO et al., 2021).

Evidence of PWs in the mesosphere has been studied extensively from wind observations by medium frequency (MF) radars operated at different geographic locations (GURUBARAN; RAJARAM, 2000; HARRIS, 1994; HARRIS; VINCENT, 1993). These waves are very large horizontal scale atmospheric oscillations in neutral wind, density, and pressure that propagate zonally and vertically from their troposphere–stratosphere generation

[2] Wavenumber ($\tilde{v}$) is the number of full cycles in a unit distance. Where $\tilde{v} = \frac{1}{\lambda}$

regions to the MLT region and perhaps beyond. They found the oscillation periods of these waves to range from 2- to 20-day and beyond (FORBES, 1995; FORBES; ZHANG, 1997) with the main periods being near the normal Rossby modes, i.e., 2-, 5-, 10- and 16-days, as well as at other (secondary) periods resulting from the superposition of these periods.

An important characteristic of PW is that their occurrence is episodic so attention needs to be focused on specific intervals. Brown and Williams (1971) have presented the influence of PW on ionospheric parameters, where they showed a correlation between stratospheric pressure variations and electron density.

Quasi-stationary Rossby waves are important to the midlatitude dynamics, because they can largely influence the atmospheric fields like wind and temperature, and they are responsible for the ozone and other trace gases distribution (PAULINO et al., 2021). Most quasi-stationary Rossby waves are known to be forced by tropical convective activity (AMBRIZZI; HOSKINS, 1997; HOSKINS; KAROLY, 1981). Rossby normal modes, also known as free modes, are predicted by the theory as oscillatory solutions of Laplace's tidal equation without forcing. Laplace's theory is constructed over an isothermal and non-damping atmosphere; thus, the real conditions of the atmosphere can produce normal modes with some similarities to the theoretical ones. The class of planetary waves which occur near the equator and the most commonly observed in the MLT region are the Kelvin waves, which are classified as low Kelvin waves (periods of 10–15 days), fast Kelvin waves (periods of 6–10 days) and ultrafast Kelvin waves (periods of 2.5–6 days) (CHEN; MIYAHARA, 2012).

In theory, the effects of the Earth's rotation cannot be neglected when the spatial scales of the movements under study are on the order of thousands of kilometers, and a rotating frame must be considered. The variation of the Coriolis force with latitude acts on the atmosphere as an external force, resulting in waves horizontally transverse waves with lengths of thousands of kilometers, which are called planetary waves, and whose study is carried out taking into account the terrestrial sphericity. The studies of wave movements in a rotating sphere are based on Laplace's theory of tides, also called "shallow water equations" in a sphere, whose origin is the work Mécanique Céleste de Laplace from 1799, in which the main interest was the tidal oscillations in an incompressible ocean of uniform depth. However, Laplace also assumed the existence of equivalent motions in the atmosphere, which was later followed by several researchers, so that Laplace's theory of ocean tides forms the basis for the theory of atmospheric tides.

Planetary waves also known as Rossby waves are considered to drive the planetary vorticity which equals the Coriolis parameter

$$f = 2\Omega sin\phi, \tag{21}$$

where Ω is the Earth's angular speed and ϕ is the latitude.

In a Cartesian frame where the essential effects of sphericity are retained by expanding the latitudinal variation of planetary vorticity (Coriolis parameter) in a Taylor expansion about fixed latitude ϕ (ROSSBY, 1939), thus

$$f = \left(\frac{df}{dy}\right)_0 + \text{asin}(\phi_0)\,(\phi - \phi_0). \tag{22}$$

Assuming a waveform solution $\tilde{A} = A\exp(i\omega - kx)$ and a uniform zonal background flow $\bar{u}$, the dispersion relation and phase velocity are obtained. The group velocity, however, is taken to be $\frac{\partial\omega}{\partial k} = u_g$, where the group velocity is eastward relative to the mean flow.

As mentioned earlier, wave movements in a rotating sphere are based on Laplace's theory of tides, also called "shallow water equations" in a sphere.

Laplace's tidal equations are the linearized equations of motion on a background state of rest for an ideal ocean. If a dependent variable in favor of the geopotential oscillation $\phi' = g\eta$ with $\eta = \zeta + f$. Where, ζ is the relative vorticity, that is defined by the rotational velocity ($\zeta = \nabla \times v$) and f as already mentioned earlier to represent Coriolis parameters. The waveform assumes the solutions of the form

$$\phi'(\phi, \lambda, t) = \Phi(\phi)exp\big(i(\omega t - s\lambda)\big), \tag{23}$$

where s is the zonal wavenumber, and λ is the longitude obtained

$$F\left(\theta^{\omega,s}(\phi)\right) = \epsilon\theta^{\omega,s}(\phi). \tag{24}$$

The operator F is defined as

$$F = \frac{d}{d\mu}\left(\frac{1-\mu^2}{f_*^2-\mu^2}\frac{d}{d\mu}\right) - \frac{1}{f_*^2-\mu^2}\left[\frac{s}{f_*}\left(\frac{f_*^2+\mu^2}{f_*^2-\mu^2}\right) + \frac{s}{1-\mu^2}\right], \tag{25}$$

where $\epsilon = \frac{g\bar{h}}{(2\Omega R_p)^2}$.

The parameter ϵ is known as Lamb's parameter and here and henceforth, except as noted explicitly, f_* is the normalized frequency $f_* = \omega/2\Omega$. The latitudinal coordinate is $\mu = \sin(\phi)$ and $R_p \equiv a$ is the planetary radius. Equation (24) is Laplace's tidal equation (LTE). One solves the LTE subject to boundary conditions as an eigenfunction-eigenvalue problem to obtain the eigenfunction θ and the eigenvalue f_*. The eigenfunctions of the LTE are called Hough functions (HOUGH, 1898). The solutions depend parametrically on s and λ. For every s and λ there is a complete set of modes each with a different frequency and latitudinal structure.

2.5 The Geomagnetic Field

In the upper atmosphere/ionosphere, the earth's external magnetic field affect charged particles. A hydrodynamic dynamo that operates in the Earth's outer fluidic core mainly produces the magnetic field around the Earth. Rocks magnetized in the lithosphere have a secondary contribution. Another contribution to the geomagnetic field is of external origin. Electric current systems in the ionosphere and magnetosphere vary rapidly depending on solar activity. Since the earth's magnetosphere and ionosphere are coupled through the earth's external magnetic field and the strong interaction between charged particles and field lines result in particle capture, the movement of charged particles is restricted and diffusion processes, thermospheric winds, and electric fields drive transport processes.

2.6 Observations of Tides and Planetary Waves from Literature

Several researchers have observed and studied tides (Solar and lunar) and planetary waves in the atmosphere. Hence, this section gives a brief description of the observations and results from some of the studies carried out.

2.6.1 Solar Tides

Greenhow and Neufeld (1961) carried out early analyses of atmospheric daily variations in the upper atmosphere at Jodrell Bank. They used data of about 100 days scattered through the years 1953-1958 to observe winds over 80-100km. Elford (1959) also observed winds in Adelaide, Australia using data from about 400 days from 1952 until 1955 over the same height range as Greenhow and Neufeld (1961). Haurwitz (1962) based on the results obtained by Greenhow and Neufeld (1961), and Elford (1959) to review the tidal phenomena in the upper atmosphere, and prepare convenient displays Haurwitz (1964).

Daily variations in wind at altitudes from about 110 to 120 km, as inferred from dynamo calculations, are somewhat difficult to interpret. Such calculations up until then assumed that winds are independent of altitude (which, as we have seen, is not the case below 110 km). Using electrical conductivities calculated from observations of electron distributions with height and their time variations, Maeda (1955) and Kato (1956) calculated the time varying 'slab' winds giving rise to the observed quiet day daily variations in the geomagnetic field.

2.6.2 Lunar Tides

The investigation of the lunar tides in the atmosphere has a long history. The first studies of the atmospheric lunar tides were based on observations of pressure on the surface. However, many of these studies presented problems due to series of insufficient data. The atmospheric lunar tide was determined for the first time, with good precision, in the middle of the 19th century by Sabine (1847). This oscillation showed a maximum trend in the local time of noon and midnight.

Haurwitz and Cowley (1969) calculated the mean tidal amplitude and lunar semidiurnal on the surface pressure for different zonal wave numbers (s) using 24 barometer measurement points in the latitude range between 50°N and 50°S. A distribution of mean amplitudes ($\bar{A}_s$) on a logarithmic scale with the zonal wave number is shown in Figure 2.2. As expected, the wave with s = 2 has the highest amplitude. Waves with zonal wave numbers 1 and 3 have the second largest amplitude, but amplitudes an order of magnitude smaller than the main one. At next waves that present significant amplitudes are s = 0 and s = −2. The principal component corresponds to a propagating wave with the Moon around of the Earth and the wave with a zonal wave number equal to zero represents a wave stationary. Waves with s 6 = 2 can be generated by the different properties of friction of continental and oceanic surfaces, and by the uneven distribution of temperature and wind systems that can modify the atmosphere's response to lunar potential. Ocean tides can also influence the generation of these waves.

Figure 2 - Average lunar semidiurnal tidal amplitude at surface pressure for different zonal wave numbers.

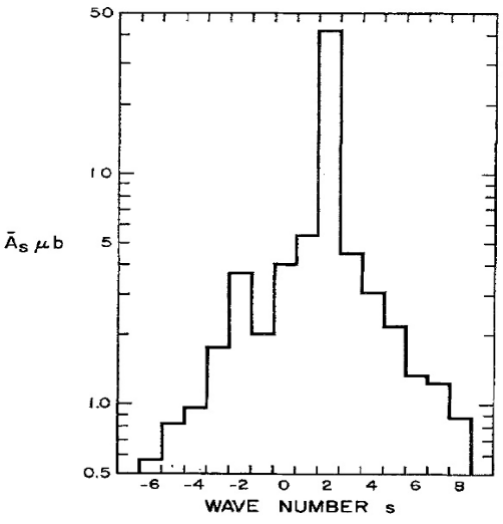

Source: Haurwitz and Cowley (1969)

Lunar tides in the upper atmosphere have been observed in magnetometer data by several researchers (BARTELS; JOHNSTON, 1940a, 1940b; CHAPMAN; BARTELS, 1940; ECCLES et al., 2011; STENING, 1986; TARPLEY; BALSLEY, 1972; YAMAZAKI, 2022; YIZENGAW; CARTER, 2017 and references therein).

Stening (1986) observed and studied the effects of lunar tides in the ionosphere using data from the magnetometer and ionosonde. He determined the diurnal and seasonal variations of lunar tides in the foF2 and explained that the seasonal variations of the amplitudes are sometimes annual and sometimes semiannual.

Figure 3 - Local time variations of lunar tides in March at sunspot minimum at Huancayo. The (a) ΔH variation and (b) foF2 variation. The line with dots is the phase (time of maximum in lunar hours) and the dashed line indicates two standard deviations.

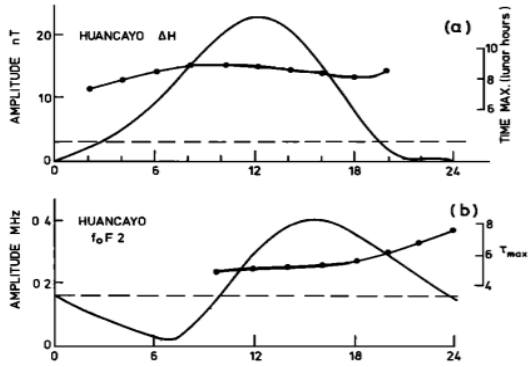

Source: Stening (1986)

Figure 4 - Seasonal variations at Huancayo 12:00 LT, as Figure 3 except the dot-dash line is the phase at 00:00 LT.

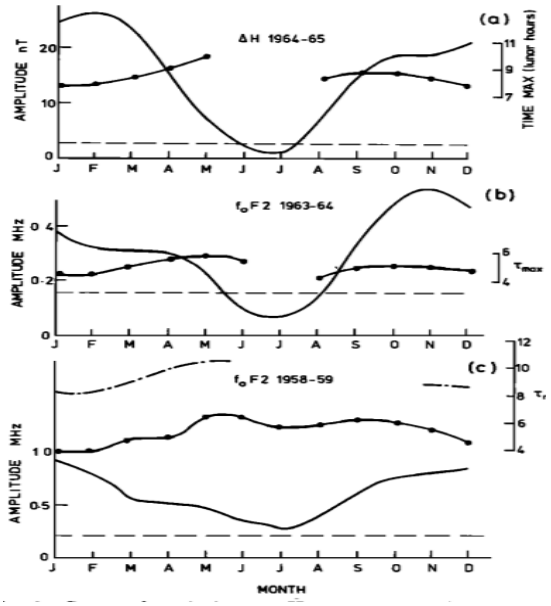

Source: Stening (1986)

Tarpley and Balsley (1972) studied the lunar variation in the Peruvian electrojet. They divided the H-component records into bimonthly intervals and analysed the lunar variations by using the Chapman-Miller method. They found that the lunar variations in the electric field inferred from electron drift data are consistent with those deduced from geomagnetic variations.

2.6.3 Planetary Wave

Sources of ionospheric day-to-day variability in foF2 and NmF2 in the thermosphere and ionosphere community have been examined for decades (e.g., FORBES; PALO; ZHANG, 2000; MENDILLO et al., 2002; RISHBETH; MENDILLO, 2001). Using over 100 ionosonde stations from 1967 to 1989 under quiet geomagnetic conditions, Forbes et al. (2000) found that variations of the 2-30 day period PW have a magnitude of 15-20% in hourly foF2, mainly due to "meteorological influences". Rishbeth and Mendillo (2001) have shown that the daily fluctuations of NmF2 have a standard deviation of 20% by day and 33% by night. Most of the variability was due to geomagnetic activity, whereas the rest were attributed to "meteorological" sources, which were consistent with results of Forbes et al. (2000). The propagation of gravity waves (GWs), tides, and PWs from the lower and middle atmosphere to the upper atmosphere are considered to be of "meteorological" origin (e.g., CHANG; LIU; PALO, 2011; LIU, 2016 and references therein).

Haldoupis and Pancheva (2002) provided direct evidence of the role of PWs on mid-latitude sporadic E-layer generation, based on foEs observation from an extended longitudinal chain of stations. The manifestation of PW effects in the equatorial ionosphere gained wide recognition after Chen (1992) demonstrated 2-day oscillations in the equatorial ionization intensity and Forbes and Leveroni (1992) demonstrated 16-day oscillations in the EEJ intensity and the F2-layer peak density.

They observed and studied quasi-16 day oscillation in the ionosphere in the ΔH. They discovered that this quasi 16-day oscillation in the E- and F-regions of the equatorial ionosphere during January/February 1979 was apparently connected with the upward penetration of a free Rossby mode excited in the winter stratosphere. The observed effects were interpreted in terms of electric fields induced by the ionospheric wind dynamo.

Figure 5 - Hourly values of perturbation in horizontal magnetic intensity (ΔH) at Huancayo for 1979. Inset magnifies data for first 60 days to emphasize quasi 16-day modulation of daytime values.

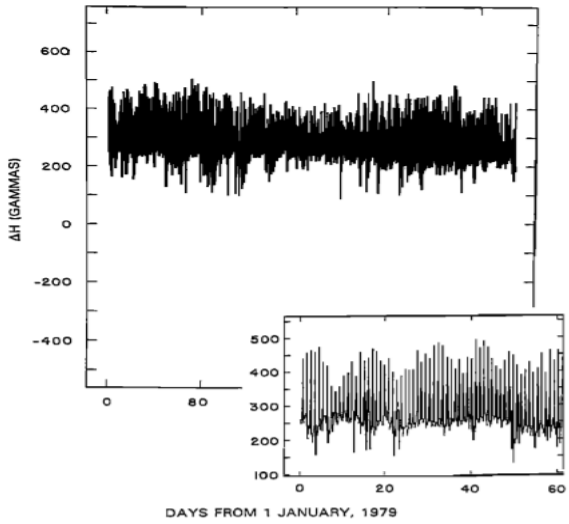

Source: Forbes and Leveroni (1992)

Figure 5 presents the hourly values of perturbations in the horizontal magnetic intensity (ΔH) at Huancayo for 1979. Day-to-day oscillations are clearly observed in the data throughout the whole year. The inset further shows the magnified data for first 60 days. This was done to emphasize the quasi 16-day modulation of daytime values.

Figure 6 - Power spectrum corresponding to first 64 days of hourly measurements of ΔH

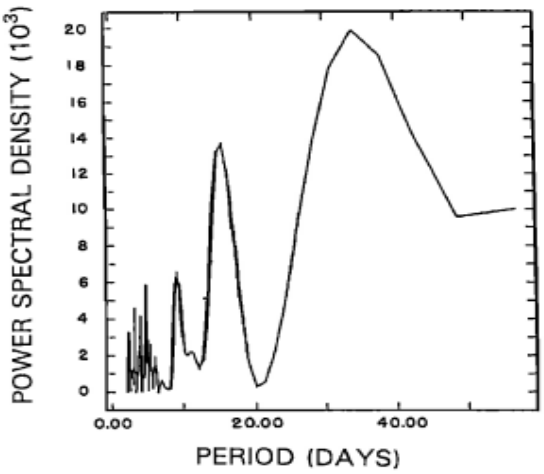

Source: Forbes and Leveroni (1992)

Figure 6 shows the power spectrum for the first 64 days for the hourly measurements of the magnetic field intensity. The quasi 16-day spectrum is clearly prominent in the data.

3 INSTRUMENTATION

This chapter describes observational sites and the principal characteristics of the instruments used in obtaining the data analyzed in this work.

3.1 Observation

Observational data with a temporal resolution of a minute was used in this study. They were acquired from six different magnetometer stations in the American (Brazilian) and African sectors. The magnetometer data for the Brazilian sector were acquired from the EMBRACE website http://www2.inpe.br/climaespacial/portal/en/ and are located at São José dos Campos, São Paulo (23.21ºS, 45.97ºW; Dip latitude 20.4ºS), Eusébio, Ceará (3.89°S, 38.46°W; Dip latitude 08.4ºS), São Luís, Maranhão (2.53°S, 44.30°W; Dip latitude 3.9ºS). The data from the African sector were obtained from the INTERMAGNET network of magnetometers website https://www.intermagnet.org/data-donnee/download-eng.php, and are located at Hermanus, South Africa (34.41° S, 19.23° E; Dip latitude 45.9°S), Tsumeb, Namibia (19.24° S, 17.73° W; Dip latitude 39.1°S) and Tamanrasset, Algeria (22.79° N, 5.52° E; Dip latitude 14.4°N) in the African Sector. In addition, ionosonde data with a temporal resolution of 5 minutes were acquired from ionosonde stations located at São José dos Campos (23.21ºS, 45.97ºW; dip-latitude 20.4ºS) and Araguatins (5.65ºS, 48.07ºW; Dip latitude 4.17ºS), Brazil. These stations/locations were selected because they provide a good dataset (whole year) and are located at different latitudes. For more details, see Figure 7 and Table 2.

Figure 7 - The diamonds (red) show the locations (longitude and latitude) of the magnetometer stations in SJC, EUS, and SLZ in the Brazilian sector and TAM, TSU, and HER in the African sector whilst the circles (blue) show the locations of the ionosonde stations in ARA, JAT, and SJC all in the Brazilian sector. The purple line is the dip-latitude.

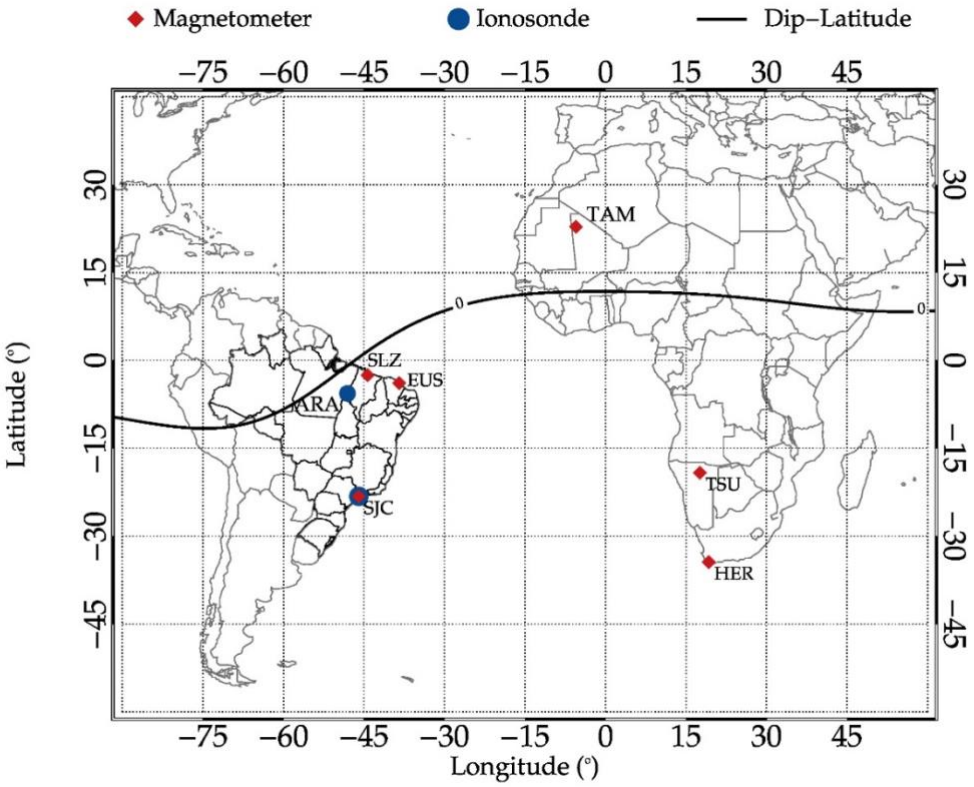

Source: Author

Table 2 - Magnetometer and Ionosonde station names, codes, geographic coordinates, and dip-latitude coordinates over the Brazilian and African sectors.

Magnetometer Station Name	**Station Code**	**Geo. Lat. (+N)**	**Geo. Lon. (+W)**	**Dip. Lat. (+N)**
Brazilian Sector				
Sao Luis	SLZ	-2.6	-44.2	-3.9
Eusebio	EUS	-3.9	-38.4	-8.4
S. J. dos Campos	SJC	-23.2	46.0	-20.4
African Sector				
Tamanrasset	TAM	**22.8**	-5.5	**14.4**
Tsumeb	TSU	-19.2	-17.6	-39.1
Hermanus	HER	-34.4	-19.2	-45.9
Ionosonde station Name	**Station Code**	**Geo. Lat. (+N)**	**Geo. Lon. (+W)**	**Dip. Lat. (+N)**
Brazilian Sector				
Araguatins	ARA	-5.65	48.07	-4.17
S. J. dos Campos	SJC	-23.21	45.97	-20.4

Source: Author

3.2 Magnetometer

Figure 8 - A magnetometer setup and observatory (left and middle panel) and control unit after data acquisition (right panel).

Source: EMBRACE (2021)

The magnetometer is a device that allows the measurement of variations in the geomagnetic field thus it measures the strength and direction of the earth's magnetic field. The operation of the magnetometer is based on a number of different principles with a majority of magnetometers containing a magnetic device sensitive to a magnetic field. Whilst some magnetometers use a permanent magnet and an electromagnet, others make use of the magnetic properties of the atomic nuclei (DENARDINI et al., 2020; EMBRACE, 2021; INTERMAGNET, 2021).

Three quantities are needed for a complete description of the earth's magnetic field. These are either three orthogonal strength components (X, Y, and Z), the total strength and two angles (F, D, and I) or two strength components and an angle (H, Z, and D). Where the H represents the horizontal or magnetic north, D the magnetic declination angle, and Z the downward vertical components. Figure 9 shows the components of the geomagnetic field measurements.

Figure 9 - Components of the geomagnetic field measurements for a sample Northern Hemisphere total field vector **F** inclined into the Earth.

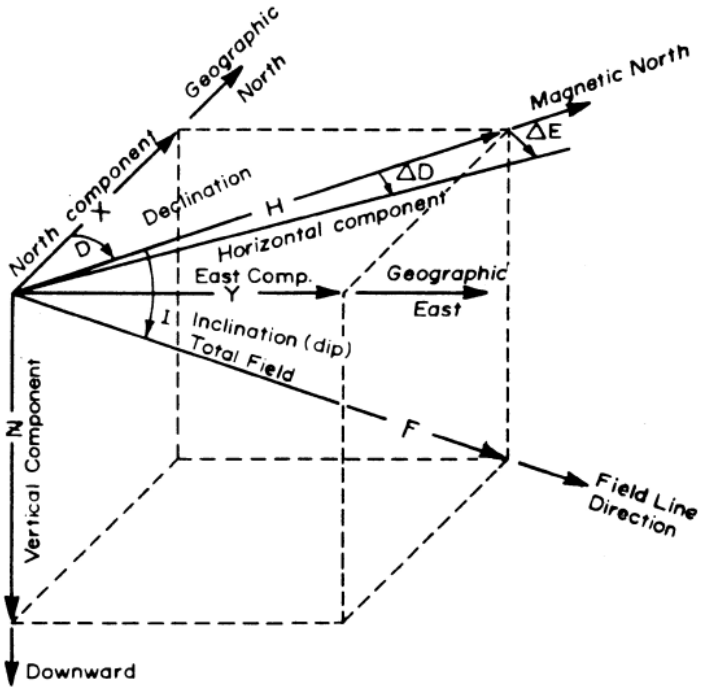

Source: Campbell (2003)

In this study, we use the H-component of the geomagnetic field. This component signifies the Magnetic field component parallel to the earth's surface (Points towards the magnetic south pole).

3.2.1 InterMagnet

This is a consortium of national geomagnetic observatory leaders who have arranged a cooperative, near "real-time" data recovery system, from about 80 observatories, called INTERMAGNET for "INTERNATIONAL Real-time MAGNETIC observatory network". The objective of INTERMAGNET is to establish a global network of cooperating digital magnetic observatories, adopting modern standard specifications for measuring and recording equipment, in order to facilitate data exchange and the production of geomagnetic products in close to real-time.

Figure 10 - Map of the INTERMAGNET Magnetic Observatories (IMOs) in the INTERMAGNET network across the world.

Source: INTERMAGNET (2021)

An IMO is a magnetic observatory which has full absolute control and provides one-minute magnetic field values measured by a vector magnetometer, and an optional scalar magnetometer, all with a resolution of 0.1 nT. Vector measurements performed by a magnetometer must include the best available baseline reference measurement. IMOs must try to meet the following recommendations (INTERMAGNET, 2021):

The definitive data from the IMO must have an accuracy of ±5 nT. The specifications for the vector magnetometer are in Table 3.

Table 3 - Specifications of the Vector Magnetometer from an IMO

Property	**Specifications**
Resolution	0.1 nT
Dynamic Range	8000 nT at High Latitude 6000 nT at Mid/Equatorial Latitude
Band Pass	D.C. to 0.1 Hz
Sampling Rate	1 Hz
Thermal Stability	0.25 nT/°C
Long term stability	5 nT/year

Source: IMO (2021)

Table 4 - Specifications of the Scalar Magnetometer from an IMO

Property	Specifications
Resolution	0.1 nT
Accuracy	1 nT
Sampling Rate	0.033 Hz (30 sec)

Source: IMO (2021)

For a scalar magnetometer, the specifications in Table 3 are required.

3.2.2 EMBRACE MagNet

EMBRACE MagNet which is part of the Programa De Estudo e Monitoramento Brasileiro De Clima Espacial (EMBRACE) established by the Instituto Nacional de Pesquisas Espaciais (INPE), is made up of a network of magnetometer observatories in the South American sector. Figure 11 shows the locations of these magnetometer observatories.

Figure 11 - Map of the EMBRACE MagNET observatories across South America. The blue triangles show the locations whereas the red lines show the geomagnetic field lines with their variations.

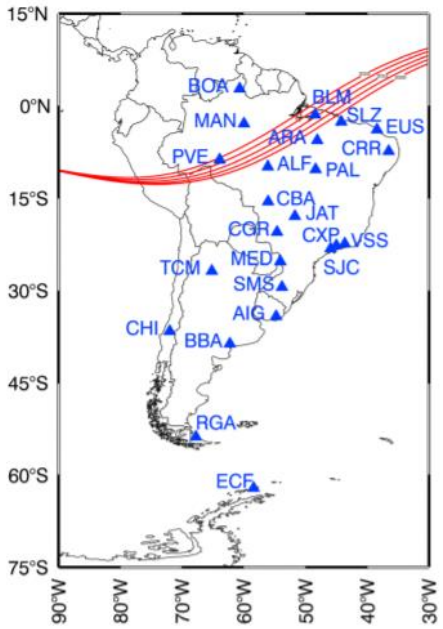

Source: Denardini et al. (2018)

The EMBRACE MagNET magnetometer range is ± 1.000 nanoteslas (nT), and is measured by a 16-bit analog-to-digital converter, providing 0.03 nT sensitivity. With the

temperature compensation of the sensors and electronics, the accuracy of the instrument is 1 nT. The instruments are monitored for correct operation by adding a series of small chains attached to a set of auxiliary windings during calibration and verification of weekly magnetometer proper gain and transient responses (EMBRACE, 2021).

3.3 Ionosonde

The ionosonde is basically a radar system that transmits radio frequency pulses in the range of 1 to 20 MHz and measures the time (Δt) between transmission and reception of the echo. Through the transmitting antenna (delta type) of the ionosonde a radio frequency pulse (ft) is transmitted at a predefined frequency, the pulse travels through the atmosphere until it reaches a region of the ionosphere where the transmitted frequency and plasma frequency are equal (ft = fp). When this condition is obeyed, the wave is reflected and later detected by the reception antennas (dipole type).

The plasma frequency is given by: $f_p = \frac{2}{2\pi}\sqrt{\frac{n_e}{m_e\,\epsilon_0}}$

where "e" is the charge of the electron, "n_e" is the number of electrons, "m_e" is the mass of the electron and "ϵ_0" is the permissibility constant in the vacuum. By performing a frequency sweep and calculating the virtual height for each transmitted frequency you get a spectrum that we call an ionogram. In the ionogram it is possible to identify the ordinary and extraordinary traits. The ionosondes work intermittently for 24 hours and every 5 minutes an ionogram is obtained (See Figure 12).

Figure 12 - For each transmitted radiofrequency pulse, the height at which the pulse reflection occurred ($h = (c\Delta t)/2$).

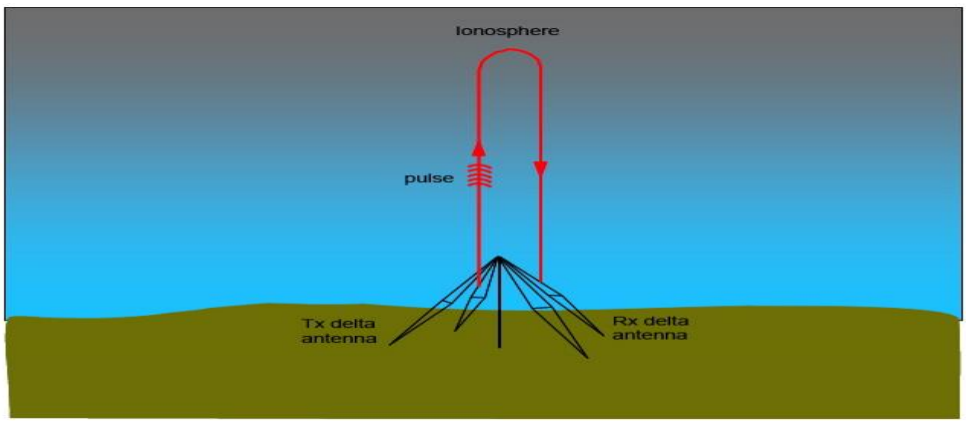

Source: Australian Space Weather Forecasting Centre (2022)

This height is called virtual height, since the pulse propagation velocity is slightly less than the velocity of light in the vacuum. The pairs ordered **Transmitted F × Virtual Height** are used to construct a graph called the ionogram. The ionosphere is a birefringent medium and radiofrequency wave splits into two different modes of propagation (ordinary and extraordinary).

Figure 13 - Transmit antenna system (right side) and reception (left side) of the ionosonde installed in Araguatins with the transmission and reception system (below), respectively.

Source: UNIVAP

The Space Physics research group at UNIVAP uses the CADI-type ionosonde located at three observatories distributed in the Brazilian sector. The instruments are located at São José dos Campos (23.21ºS, 45.97ºW; dip-latitude 20.9ºS), Jataí (17.93ºS, 51.72ºW; dip latitude 12.8ºS), and Araguatins (5.65ºS, 48.07ºW; dip latitude 4.17ºS). The working structure of the ionosonde as already mentioned, is formed by the transmission of radio frequency pulses using a transmitting antenna, and after a short period of the transmitted wave, it is reflected by the ionosphere and received by a receiving antenna. Therefore, after these two processes, it follows that the ionosonde computer calculates the transmission and reception time of the high frequency (HF) pulse, generating at the end of the process information about the height of the ionospheric layer for a given frequency. Furthermore, in the operation of the ionosonde, there

are two frequency sweep modes, corresponding to the transmitted wave pulses with a temporal resolution of 300 seconds and 100 seconds, respectively

Figure 14 - Ionogram obtained in São José dos Campos on August 6, 2018. Showing the extraction of the ionospheric parameters (h´f, foF2 and hpF2).

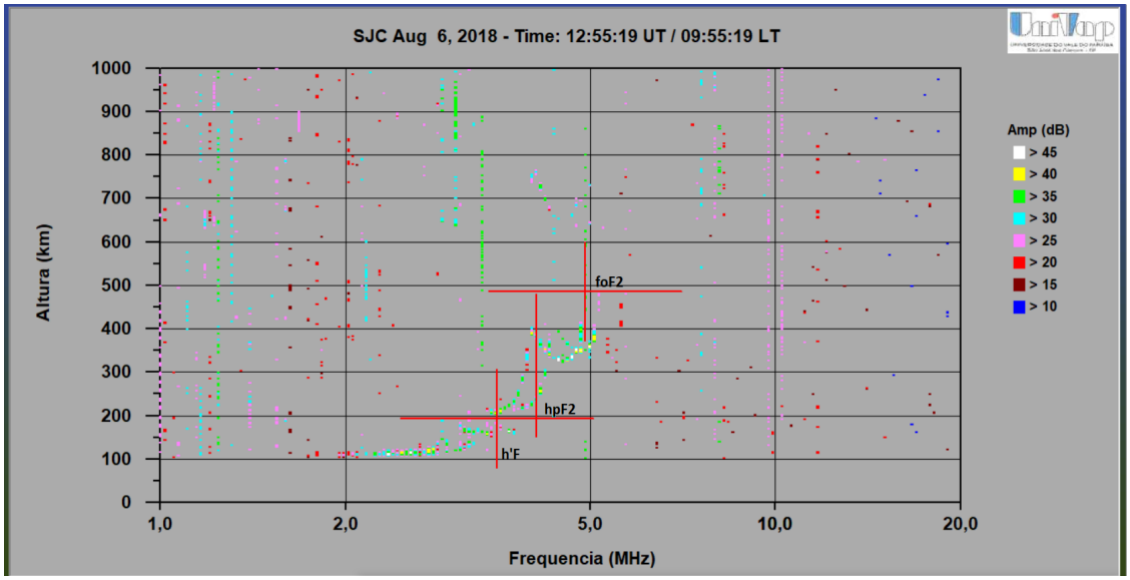

Source: Author

Figure 14 shows the interface of how the data reduction is achieved manually. The data reduction program stores the reduced data (h´F, foF2, and hpF2) and the user can view the reduced data in a table or graph form during the data reduction process.

a) Taking into account that the transmitted wave travelled with the speed of light and using the time (Δt) between the transmission and reception of the pulse, the virtual height is calculated. The minimum height at which reflection of the layer F occurred, we call h´F (given in km).

b) Using the natural frequency of the plasma and the frequency transmitted it is possible to calculate the electronic density. The maximum frequency of the ordinary trace in which an echo was recorded and the critical frequency (foF2, data in MHz).

c) The peak height of the layer (hpF2) is calculated using the critical frequency foF2. Calculate the height where hpF2 is the virtual height where it satisfies foF2 x 0.834, given in km.

This is called data reduction and the extraction of parameters (h´F, foF2, and hpF2). Using data from the ionospheric network, we investigate the spatio-temporal variation of the parameters for 2018.

3.3.1 UDIDA (UNIVAP Digital Ionosonde Data Analysis)

This is the computational tool developed by the space physics research group of UNIVAP which is used in analyzing ionospheric data. The tool makes it possible for the user to visualize the generated ionograms and helps to extract the required ionospheric parameters from the displayed ionograms.

Pillat et al. (2013) indicated that, the extraction of the parameters foF2, h'F, and hpF2 from the ionograms requires the identification of the trace of the ionospheric regions (E and F), in addition, the ionograms present noise, second reflection, and sometimes spread-F. The UDIDA program features a large number of ionospheric research aid functions to be used. However, among all the functions, the main one is data reduction, in which the program allows the user to obtain the ionospheric parameters in a manual process. So, for more details about the program's functionalities and operating instructions, see (PILLAT et al., 2013; PILLAT; GUIMARÃES, 2009). Figure 15 shows the icon and the initial screen of the UDIDA program, which is used to reduce observational data from the UNIVAP ionosonde network, whereas Figure 16 shows the station selection screen and data reduction screens respectively.

Figure 15 - Start screen of the UDIDA program developed by the space physics research group at UNIVAP- IP & D.

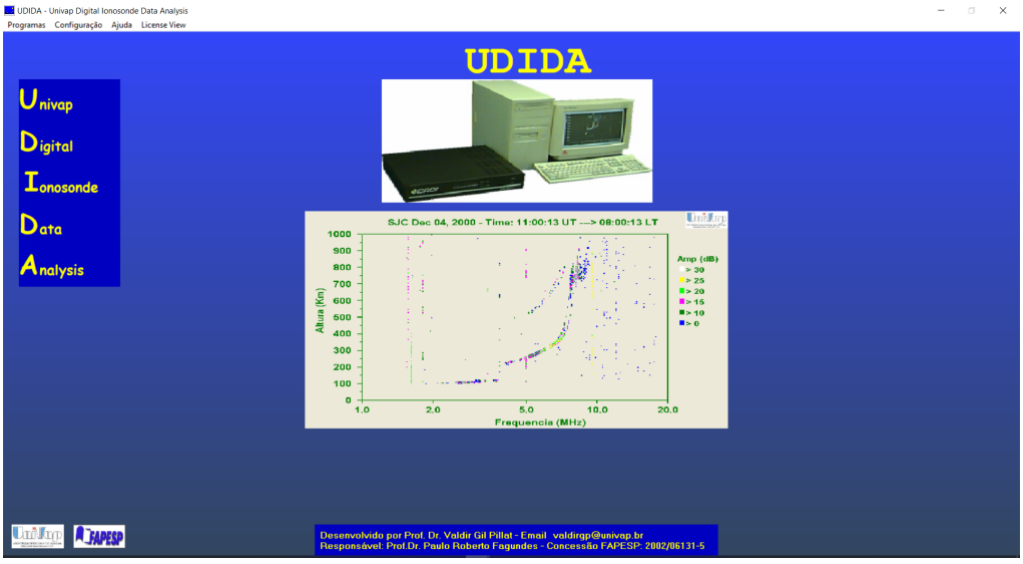

Source: Author

Figure 16 - (left panel) shows the station selection screen and (right side with an ionogram) the data reduction

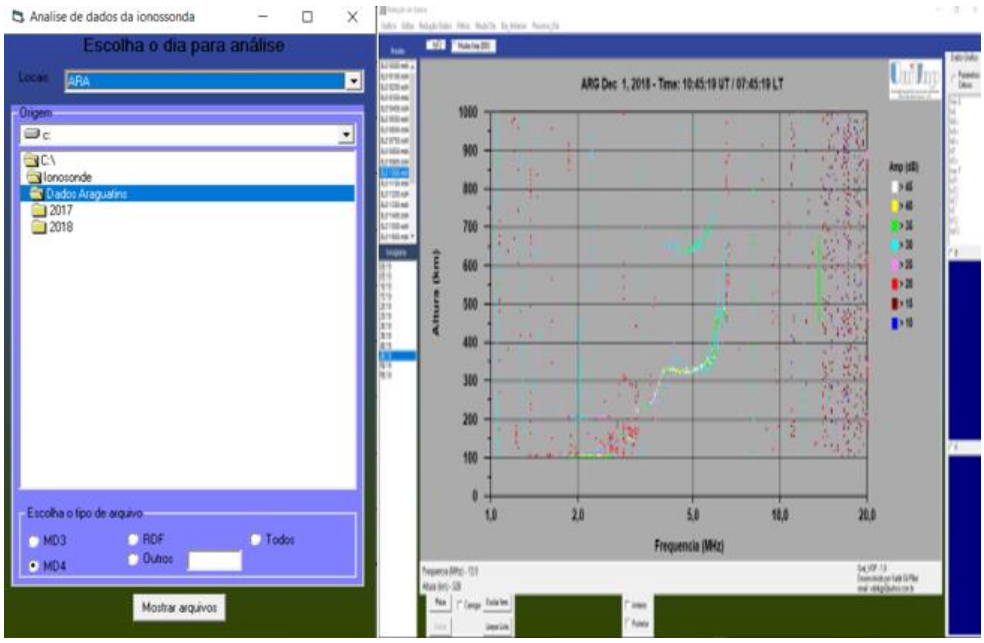

Source: Author

After this short description of some characteristics of UDIDA, it is possible to describe from the development of this research how observational data from ionosondes were used. Therefore, observational data from ionosonde to be used in the making of graphics need the method of data extraction by computational processes. Figures 15 and 16, as already stated, show the available resources of the program that aims to facilitate the reduction of observational data from the ionosonde. Hence, using the UDIDA program the data for this research were manually reduced. This program can however, reduce data automatically and manually. The ionospheric parameter used in this research were h´F (minimum virtual height of the F layer ordinary wave).

4 DATA ANALYSIS AND METHODOLOGY

This chapter outlines and explains the data analysis and methodology used in obtaining the results in the subsequent chapter. It begins with the preliminary processing of the data (magnetometer) to the step-by-step methods used to determine the atmospheric tides and planetary wave results. We also outline the data analysis for the ionosonde in determining planetary wave periods.

4.1 Data Preparation and Pre-processing (Magnetometer)

Table 5 - A matrix of the raw magnetometer data before processing for January 2018. It has the date the data was acquired, time, DOY, and all the parameters (magnetic fields) measured by the magnetometer.

DATE	TIME	DOY	EUSX	EUSY	EUSZ	EUSF
2018-01-01	00:00.0	1	23157.28	-8959.66	-8664.96	26298.61
2018-01-01	01:00.0	1	23157.12	-8959.41	-8665.00	26298.39
2018-01-01	02:00.0	1	23156.99	-8959.35	-8665.18	26298.32
2018-01-01	03:00.0	1	23156.93	-8959.17	-8664.88	26298.10
2018-01-01	04:00.0	1	23156.47	-8958.80	-8664.77	26297.54
2018-01-01	05:00.0	1	23156.09	-8958.61	-8664.92	26297.19
2018-01-01	06:00.0	1	23155.26	-8958.35	-8664.95	26296.37
2018-01-01	07:00.0	1	23154.56	-8957.96	-8664.98	26295.64
2018-01-01	08:00.0	1	23154.11	-8957.71	-8664.88	26295.12
2018-01-01	09:00.0	1	23154.26	-8957.53	-8664.75	26295.15
2018-01-01	10:00.0	1	23154.14	-8957.27	-8664.91	26295.01
2018-01-01	11:00.0	1	23154.3	-8957.05	-8665.11	26295.14
2018-01-01	12:00.0	1	23154.22	-8957	-8665.3	26295.11
2018-01-01	13:00.0	1	23153.82	-8956.75	-8665.27	26294.67
2018-01-01	14:00.0	1	23153.17	-8956.64	-8665.2	26294.04
2018-01-01	15:00.0	1	23152.2	-8956.1	-8665.47	26293.09
2018-01-01	16:00.0	1	23152.04	-8955.53	-8665.59	26292.79
2018-01-01	17:00.0	1	23152.48	-8955.62	-8665.51	26293.19
2018-01-01	18:00.0	1	23152.24	-8955.8	-8665.47	26293.03
2018-01-01	19:00.0	1	23152.48	-8955.85	-8665.64	26293.3
2018-01-01	20:00.0	1	23152.69	-8956.3	-8665.38	26293.56

Source: Author

The description of the magnetometer together with the parameters it measures have been addressed in Chapter 3 of this thesis. The data we used usually came in the format shown in Table 5. This gave the data in columns of date, time, DOY, and then the X, Y, Z, and F components of the magnetometer. We converted the time and day to DOY in order to see the graphical representation in Figure 17A. Thus, we plotted the DOY against the H(nT) parameter taking into consideration the minutes, hours, and day. Three magnetometer stations from Brazil in the South American sector and three magnetometer stations from three countries in the

African Sector were used in this study. A routine was written in Python to open each file since the original files came for each day of the month. The program therefore writes and compiles the data into a single file containing data for the entire year under study. We then convert Day of the Year (DOY) format (where DOY is not given in the data). We then identify if there are linear trends in our dataset by representing our data graphically using the Interactive Data Language (IDL). Linear trends give a tilted pattern to the dataset when represented graphically. After the graphical representation shown in Figure 17A, linear trends were seen in the time series hence, the data were further processed by the removal of the linear trend effects shown in Figure 17B. This was done by performing linear regression analysis using a routine written in Python on the raw dataset. The removal of these linear trend effects helped us to focus our analysis on the fluctuations about the trend.

Figure 17 - (A) *BH* day-to-day variation with linear trend effects (black) and (B) ΔH day-to-day variation after linear trend effects were removed (red) for EUS in the Brazilian sector in 2018.

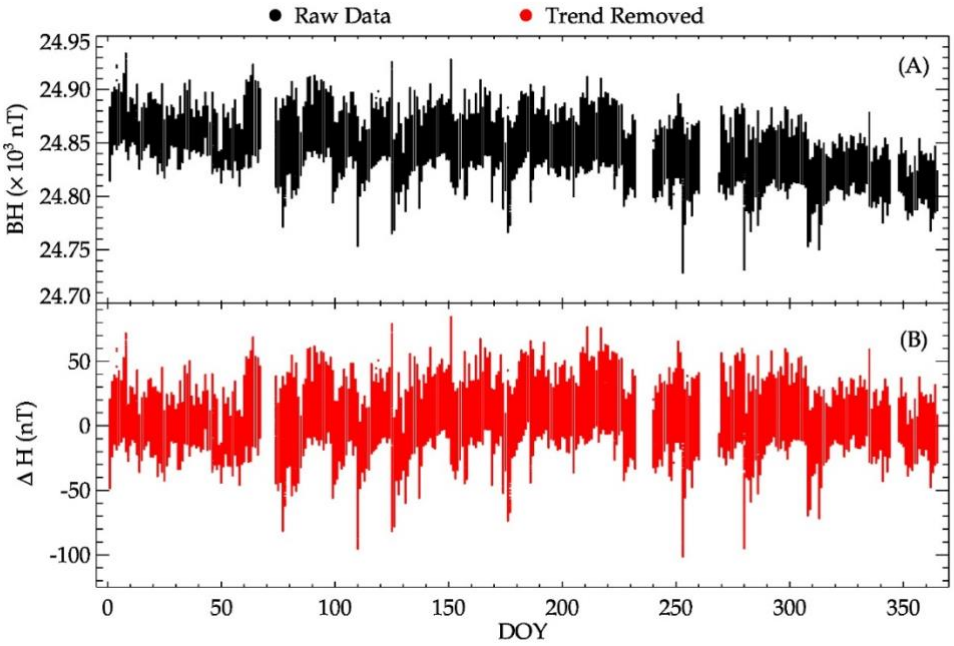

Source: Author

Figure 17A presents the *BH* (black) day-to-day variation before the linear trend effects were removed. The plot presents a tilted pattern especially towards the end of the year. Figure 17B shows the ΔH daily variation after linear trend effects were removed (red). Figure 17 generally gives us an idea on the wave activities present in our time series. After removing the linear trends, the tilted nature of the plot becomes linearized. We further for the purpose of this

study, remove the disturbed days from the dataset. This is done by using the Dst index described briefly in section 4.1.

4.1.1 Geomagnetic index (Dst) and Solar Flux 10.7

4.1.1.1 Geomagnetic index (Dst)

Dst index which stands for Disturbance Storm Time index is one of several geomagnetic indices and was developed by Sugiura (1964). It gives information about the strength of the ring current around the earth magnetosphere caused by solar protons and electrons and hence used to characterize the progression and intensity of the behavior of geomagnetic activities in the Earth's atmosphere. With reference to Dst, four terrestrial magnetic field observatories are used to characterize the variations of the magnetic field in the horizontal component (H) for the calm period. The observatories are selected based on the conditions of the measurements and their locations. In addition, the unit of the Dst index is given in nanotesla (nT) and represents the magnetic measurements obtained by the chain of magnetometers located in the equatorial region, along the globe. Gonzalez et al. (1994) classified the storms based on threshold values (intensity) and are given in Table 6. A negative Dst value implies that the Earth's magnetic field is weakened caused particularly during solar storms.

Table 6 - Threshold for storm values at 80% occurrence

Storm Classification	Dst
Small or Minor (typical substorm)	-30
Moderate	-50
Intense	-100

Source: Gonzalez et al. (1994)

For the purpose of the quiet time analysis carried out in this study, only days in the dataset which fell in the category -30 >Dst > -50 were considered. We however, used the entire dataset without any removal for the quiet time + Disturbed time analysis.

4.1.1.2 Solar Flux 10.7

The solar radiation flux at 10.7 cm is an indicator of solar activity, and often called the F10.7 index. It is one of the oldest ways used to record solar activity. According to Tapping (2013), the solar radiation flux of 10.7 cm (F10.7) is one of the most widely used indices of solar activity. Thus, a measurement of the solar flux of 10.7 cm is a determination of the intensity of the emission of solar radiation in a band 100 MHz wide centered at 2800 MHz (a wavelength of 10.7 cm) with an average of one hour. It is measured daily at local noon at the Penticton-Dominion Radio Astrophysical Observatory (DRAO) in Canada, which takes three measurements per day lasting around an hour each. The solar flux radiation unit is expressed in sfu (solar flux units), where 1 sfu = 10^{-22} W m^{-2} Hz^{-1}. The F10.7 data was obtained from the website https://omniweb.gsfc.nasa.gov/form/dx1.html.

We then apply spectral analysis which is explained in section 4.1.2 to investigate the periods present in our dataset. An example is given in Figure 19.

4.1.2 Spectral Analysis

Rayner (2001) defines spectral analysis as involving the calculation of waves or oscillations in a set of sequenced data. It also refers to the decomposition of a sequence into oscillations of different lengths and scales. It is known to be one of the several statistical techniques necessary for characterizing and analyzing sequenced data. To investigate and detect the predominant oscillations in our dataset, we apply Lomb-Scargle Periodogram (LOMB, 1976; SCARGLE, 1982) and wavelet (TORRENCE; COMPO, 1998) analysis.

4.1.2.1 Lomb-Scargle Periodogram

Lomb-Scargle Periodogram (HORNE; BALIUNAS, 1986; LOMB, 1976; SCARGLE, 1982) analysis is a very useful statistical tool commonly used to detect periodic signals in unequally spaced observations. It is equivalent to the least-square fitting of sine waves (ZECHMEISTER; KÜRSTER, 2009). However, according to Zechmeister and Kürster (2009) while standard fitting procedures require the solution of a set of linear equations for each sampled frequency, the Lomb-Scargle method provides an analytic solution and is, therefore, both convenient to use and efficient. Also, interpolation is not needed in Lomb-Scargle analysis when there are gaps in the dataset. Lomb Scargle is used to estimate the contribution of

frequency (ω) to every signal (wave) for a time series (Xt_i), where i=1,2,3,. . . . . .N_o is the number of data shown by:

$$P_x(\omega) = \frac{1}{2}\left[\frac{\left[\sum_{j=1}^{N_o} X_j cos\omega(t_j-\tau)\right]^2}{\sum_{j=1}^{N_o} X_j cos\omega^2(t_j-\tau)} + \frac{\left[\sum_{j=1}^{N_o} X_j sin\omega(t_j-\tau)\right]^2}{\sum_{j=1}^{N_o} X_j sin\omega^2(t_j-\tau)}\right] \quad (26)$$

Where τ is expressed as:

$$tan(2\omega\tau) = \frac{\left(\sum_{j=1}^{N_o} X_j sin\, 2\omega t_j\right)}{\left(\sum_{j=1}^{N_o} X_j cos\, 2\omega t_j\right)} \quad (27)$$

The τ term causes the equivalence between the periodogram fitting the functions sine and cosine of a dataset for a given frequency "ω" by a least squares method makes the periodogram invariant with respect to the original time displacement (LOMB, 1976). Although, Lomb-Scargle is a very useful method when applied to many time series, not all are sampled at equal time intervals, so there are some problems that have to be reduced. A possible problem is that the spectral leakage occurs when the spectral energy associated with a certain ω_o often escapes other frequencies due to finite length of data with irregularities in data spacing (HORNE; BALIUNAS, 1986). The spectral leak that occurs at low frequency (long period) is known as "aliasing".

4.1.2.2 Wavelet analysis

Wavelet analysis (TORRENCE; COMPO, 1998) is also a powerful tool for analyzing localized variations of power within a time series. This technique allows for the decomposition of one-dimensional series into the time-period space, where it is possible to determine both the dominant modes of variability and how those modes vary with time. Time series obtained from any natural physical system present non-stationary characteristics where all statistical moment varies all the time (LAŠTOVIČKA et al., 2003). Thus, the use of the Wavelet Transform (WT) as a unique mathematical tool enables us to analyze these time-series which gives us the temporal variability of the power spectral density. The term “Wavelet” indicates a set of functions with the form of small waves created by dilation (FARGE, 1992), $\psi(t) = \Psi(at)$ and translations, $(t) = \Psi(t+b)$, where *a* and *b* are integers applied on a simple generator function, $\psi(t)$, called the mother-wavelet (DAUBECHIES, 1992). The wavelet function, with a scale a and at position *b*, is given by

$$\psi_{a,b}(t) = a^{\frac{-1}{2}}\psi\left(\frac{t-b}{a}\right), \quad (28)$$

where a and b are real value variables and $a > 0$. The wavelet transform is defined by

$$W_\psi f(a,b) = \frac{1}{\sqrt{2}}\int f(t)\psi^*{}_{a,b}(t)dt \quad (29)$$

where $f(t)$ the temporal function is any time series and $\psi^*{}_{a,b}(t)$ is the complex conjugate of the wavelet function (TORRENCE; COMPO, 1998). According to Daubechies (1992) there are two types of wavelet functions: orthogonal and non-orthogonal wavelets where the use of each depends on the necessity (BOLZAN; FRANCO; ECHER, 2020 and references therein). For this study, we used the Morlet function because it is a wavelet function able to give us the temporal variability of the energy for each scale (frequencies). The wavelet analysis was used together with the Lomb-Scargle in order for one technique to compensate where the other falls short.

4.1.3 Atmospheric Tides (Analysis)

Atmospheric tides are important in influencing the background characteristics of the thermosphere-ionosphere system therefore are very important. Studying their effects are therefore important as they provide high-precision satellite positioning systems and solve problems associated with the propagation of radio waves, since the state of the ionosphere depends to a large extent on the wind system and, consequently, the atmospheric pressure gradients at the thermospheric heights (RIABOVA; SPIVAK, 2019). The need to study the atmospheric tide is also due to a number of other reasons. Using information on tidal fluctuations in the atmosphere, one can consider the problems associated with the possibility of detecting and monitoring weather, or even climate changes, caused by natural and man-made impacts on the Earth's atmosphere. It is also not excluded that the knowledge of the temporal and spatial variations of tidal effects will make it possible to approach the establishment of mechanisms for the formation of cyclones and anticyclones (RIABOVA; SPIVAK, 2019).

Hence, an objective of this study is to determine atmospheric tides present in our time series. The theory of these tides have been described in chapter two of this text. Although solar tides have larger amplitudes compared to lunar tides, in order to retrieve or determine both types of tides, we begin the analysis by using similar methods. Let us, first, begin with extracting our

solar tides (diurnal, semidiurnal, and terdiurnal) and thereafter, determine the lunar tide (semidiurnal). Figure 18 shows a wavelet power spectrum, which gives us the visible atmospheric tidal periods/components present in our magnetometer data.

Figure 18 - The wavelet power spectrum for EUS for 2018.

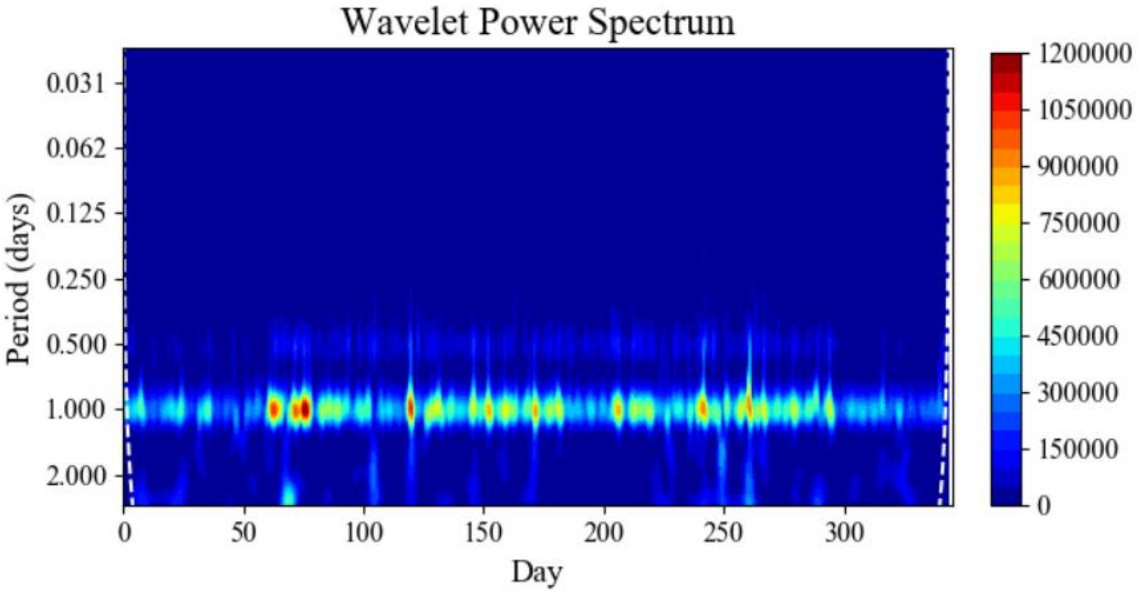

Source: Author

The wavelet analysis in Figure 18 shows that the solar diurnal tide is very strong. In addition, there is a presence of the solar semidiurnal tide in our dataset. Lunar tides are also present, however, due to their smaller amplitudes with respect to solar tides, their periods are not clearly visible in the wavelet power spectrum but with further analysis, they can be determined and retrieved. Section 4.1.3.1 deals with the determination of the solar tides whereas section 4.1.3.2 deals with the determination and retrieval of lunar tides in this case the semidiurnal tide.

4.1.3.1 Solar Tides

Solar tides are oscillations, which tend to have periods that are some integer fraction of a solar day with the solar diurnal and semidiurnal tides having 24 and 12 h periods. In addition, there is the solar terdiurnal tide which tends to have an 8 h period. This study looks at these three solar tidal oscillations. To develop the methodology, February 2018 dataset from EUS in the Brazilian sector was selected.

Figure 19 - Day-to-day variation for EUS in the geomagnetic field (H-component) in January 2018.

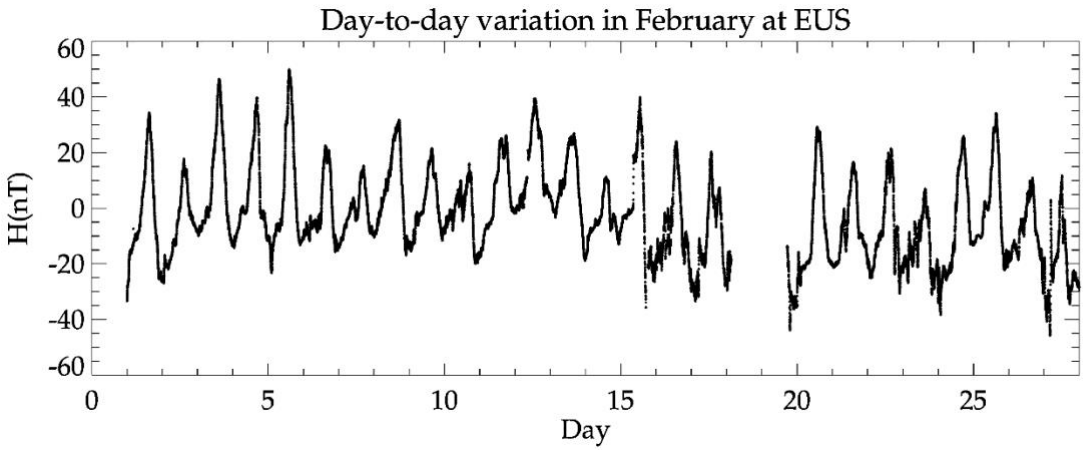

Source: Author

Figure 19 gives the day-to-day variation of the geomagnetic field at EUS for February 2018. Solar diurnal and semidiurnal variations are clearly visible in our plot. In addition, other wave components are also presented although, not visible. To identify and extract the periods present spectral analysis is applied to this data. Figure 20 gives us the wavelet power spectrum. The 'nans' in the dataset are interpolated and used to plot the wavelet power spectrum. These values, however, are not used in the tidal component analysis.

Figure 20 - Wavelet power spectrum for EUS in February 2018

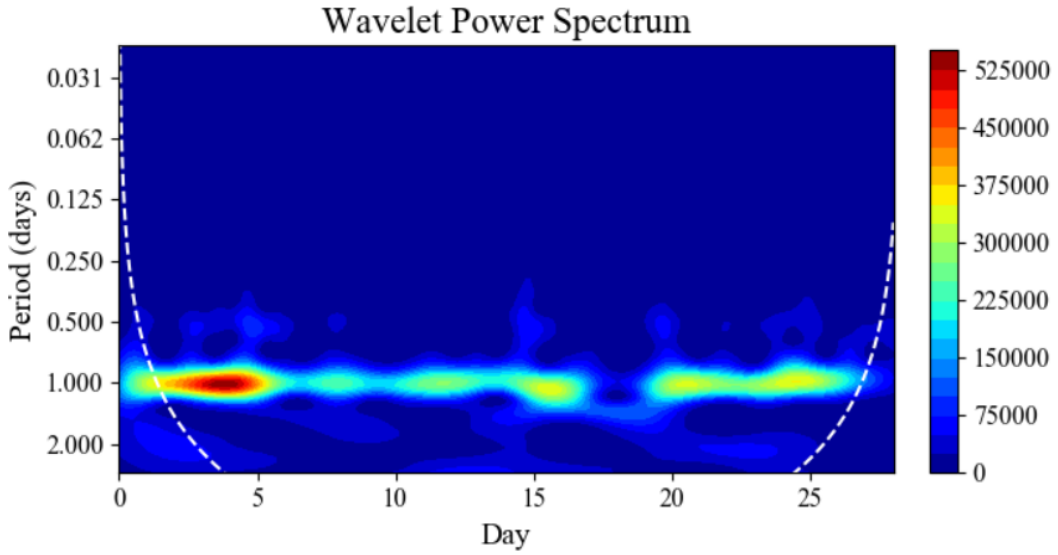

Source: Author

The wavelet power spectrum shown in Figure 20 shows a clear and strong presence of solar diurnal (24 h) wave activity and though not too strong, the presence of the solar

semidiurnal (12 h) wave activity. Lunar tides however cannot be clearly seen since their amplitudes are far less than the solar tides. They can however, be determined by further analysis. Other periods can be seen around two days but these are not of interest to us hence they would be removed before further analysis. Figure 21 shows the Lomb-Scargle Periodogram after further analysis.

Figure 21 - Lomb-Scargle Periodogram for the geomagnetic field for EUS in February 2018.

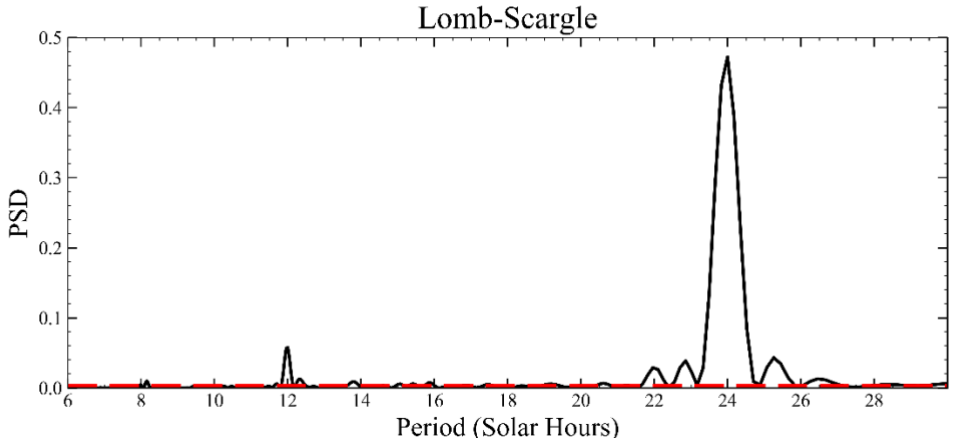

Source: Author

Lomb-Scargle Periodogram analysis in Figure 21 also like Figure 20 shows a very strong presence of the solar diurnal (24 h) tidal oscillation. The solar semidiurnal (12 h) component can also be seen clearly here although its amplitude is far lesser than the diurnal component. Other peaks can also be seen especially two prominent peaks close to the diurnal component. The red dashed line shows the 95% confidence level.

Since we have a clear picture of the periods present in our dataset, we proceed further to determine and retrieve our solar tide component after which we shall deal with the lunar tide components. To determine our components, we first group our dataset into daily averages; hence, we find the average by binning them into hours. This then gives us the hourly variation for the entire day for the entire month. The graphical representation of the daily variation is shown in Figure 22.

Figure 22 - Daily variation for EUS in February 2018.

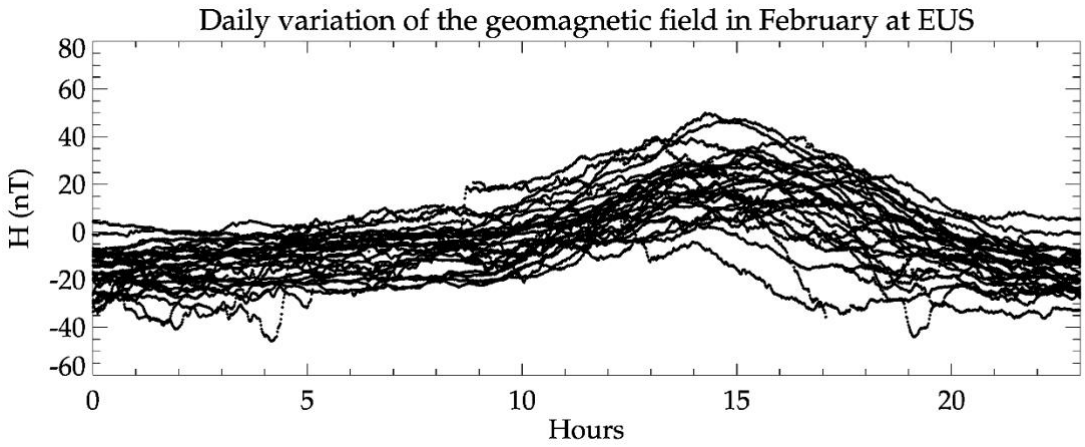

Source: Author

The plot in Figure 22 shows the Daily variation for EUS for the entire month of February 2018. The solar diurnal component is observed strongly in this dataset whereby we can see one prominent peak (strong diurnal variation). This is seen as a trend throughout the whole month of February 2018. The next step after we average our dataset is to, average all hours in the day for the entire month into an hour each in order to obtain a composite solar day. This was done because the periods we are searching for are within a solar day hence using the composite method. This we do by taking the average for hour 3 for the whole of January. Thus, we then find the average value for all the hour 3s from January 1 to 31 (if data is available for all days) therefore getting a single value to represent that particular hour in the day. This then gives us a single daily variation plot for the whole month in a day. A least square fitting analysis was then applied using the relation:

$$V = A + Bcos\left(\frac{2\pi}{24}t + \varphi_1\right) + Ccos\left(\frac{2\pi}{12}t + \varphi_2\right) + Dcos\left(\frac{2\pi}{8}t + \varphi_3\right) \qquad (30)$$

Where:

A is an unknown constant, B, C, and D are unknown amplitudes and are related to the unknown phases φ_1 , φ_2, and φ_3. Also, t is the time in solar hours. This was done in order to obtain the amplitudes and phases for the solar tide. The results of this analysis is fully given and discussed in chapter 5 of this thesis. Figure 23 shows the Least Square fit and the average daily variation for EUS in January 2018.

Figure 23 - Least square fit for the February 2018. The black stars are the average values for each time of the day whereas the red line (curve) is the fit for the points using the three solar tide components.

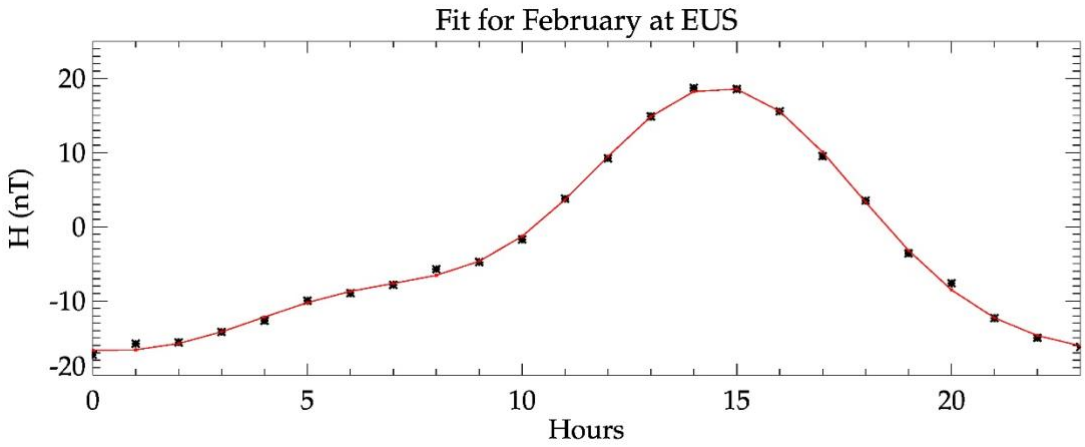

Source: Author

Figure 23 gives the least square fit for February 2018. One strong peak is observed which represents the solar diurnal variation. In the equation however, we considered three components, ie: Diurnal, semidiurnal, and terdiurnal components. We included all three components in the fit in order to remove it from the component since we would use the residual obtained after this step to determine (calculate for) the lunar tide. The results giving the three solar tidal components are in Appendix A. The next section deals with the determination and retrieval of the semidiurnal lunar tide component.

4.1.3.2 Lunar Tide (Semidiurnal)

In order to obtain the lunar tide which has amplitudes far less than solar tides, the fit values (solar tides) obtained were then subtracted from the actual data in order to obtain the residuals. This was done to remove any solar tidal effect present from the data. We then convert the solar time to lunar time because lunar tides are "Moon following" rather than "Sun following", which means they will not repeat from day to day with the same phase as measured in local time. Instead, an analysis must be applied that relates the tidal phase to the position of the Moon in the sky (SANDFORD; MULLER; MITCHELL, 2006). This conversion is achieved using the relation (PAULINO; BATISTA; CLEMESHA, 2012):

$$t = \tau + v \quad \text{Which becomes} \quad \tau = t\text{-}v \tag{31}$$

Where:

τ is the lunar time, t is the local apparent solar time and v is the age of the moon.

A fit for the semidiurnal lunar tide is then constructed for the residual data in lunar time. The amplitude and phase of the semidiurnal tide were then obtained by applying the least square fit using the relation:

$$V = A + Bcos\left(\frac{2\pi}{12}\tau + \varphi\right) \quad (32)$$

Where:

A is a constant; B is the unknown amplitude, τ the time in lunar hours, φ is the semidiurnal phase. This was done in order to obtain the amplitude and phase of the component. In this relation, only the semi-diurnal component was fitted since that was our interest.

Figure 24 - Lunar tide variation in February 2018 after the residual was determined by removing any solar tide effect. The black circles are the residuals whereas the red line is the fitted component

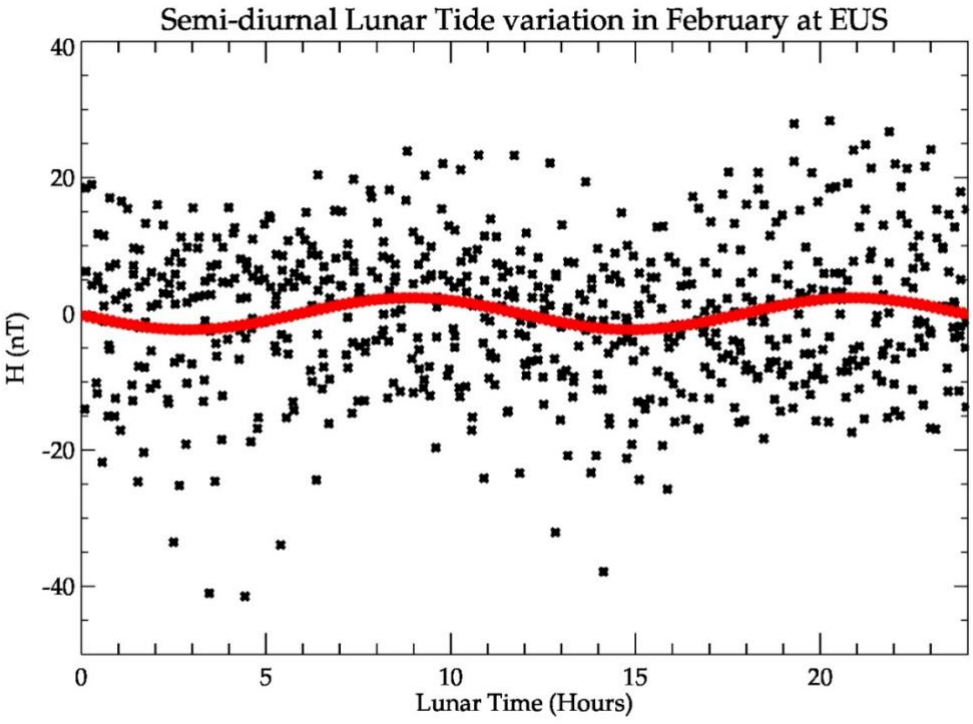

Source: Author

The semidiurnal lunar tide is seen as two peaks (red) in Figure 24. This was obtained after the semidiurnal tide was fit to the residuals in lunar time. The black crosses are the residuals after the solar effects were subtracted.

In order to verify the periods present after the fitting, spectral analysis was applied once more on the residual dataset. Figure 25 shows the result for the Lomb-Scargle Periodogram.

Figure 25 - Lomb-Scargle Periodogram for the semidiurnal lunar tide component in February 2018.

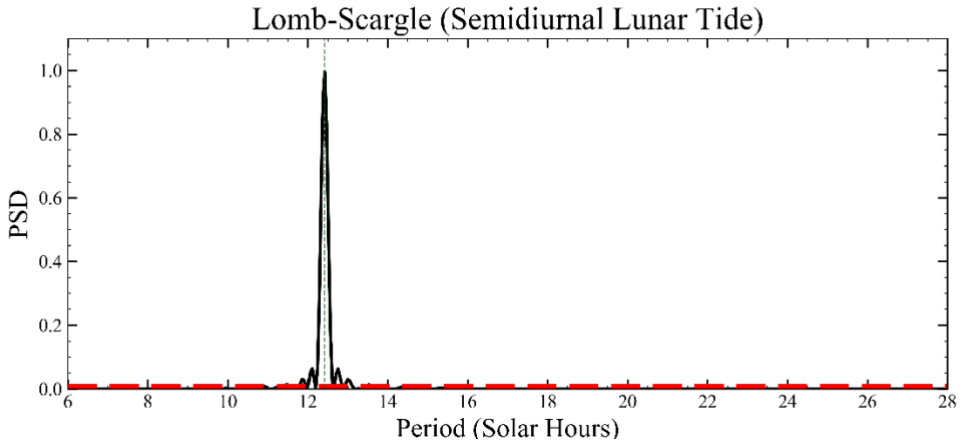

Source: Author

Figure 25 shows a good presence of the semidiurnal lunar tide in the geomagnetic field at EUS which is at 12.42 h. This plot however, was obtained after the conversion of our lunar time to solar time. This was done so we can see the lunar tide on the solar time frame where it has a period at 12.42 h. The dark-green dashed line running vertical clearly shows that our peak is at 12.42 h. The red dashed line running horizontal gives the 95% confidence level of our peak. This methodology was then applied to the 2018 dataset.. Also, this analysis was conducted without taking into consideration the effects of the disturbed days on the components hence, all the dataset including the disturbed time was used in this present analysis. In order to see the effect of the disturbed storm time on these components, we also further removed the disturbed days from the dataset by considering the Dst (Disturbed time index) index and after, applied the same methodology. The quiet time results are presented and discussed together with the disturbed plus quiet time (disturbed + quiet time) results in chapter 5.

4.1.3.3 Error bars (Standard Error)

Error bars were plotted on the points of the plotted amplitudes and phases. They represent the uncertainty or error of the corresponding coordinate of the point. In this study, we used the standard error which is calculated as:

$$\text{Standard error} = s / \sqrt{n} \quad (33)$$

Where:

‘s’ is the sample standard deviation and ‘n’ is the sample size

The next sections detail the step-by-step method used in determining planetary wave periods using magnetometer and ionosonde datasets.

4.1.4 Planetary Waves

These are global scale oscillations of atmospheric circulation (LAŠTOVIČKA et al., 2003), which extend coherently around a full longitude circle (SMITH; PERLWITZ, 2015) and occur in rotating fluids (BEER, 1974). They tend to have wavelike perturbations in the longitudinal and vertical directions and are mostly in the latitudinal direction (SMITH; PERLWITZ, 2015), with dominant zonal wave numbers of 1, 2, and 3 of periods from 2 to 30 days (FAGUNDES et al., 2005 and references therein)**.**

The next objective in this study is to determine the planetary wave periods present in the dataset. Hence, for a clear and graphical interpretation of the day-to-day variability within the time series, we select two days of data from the entire dataset for all stations in the African and Brazilian sectors and analyze. Figure 26 shows the ΔH daily variation for the two selected days.

Figure 26 - Daily ΔH variations on November 19 and November 20, 2018 for the Brazilian (upper panels) and African (bottom panels) in the low latitude, equatorial, and mid-latitude regions. The red, black, and blue line plots in the upper panel represent EUS, SJC, and SLZ respectively while, the red, black, and blue line plots in the lower panel represent HER, TAM, and TSU respectively. The dotted vertical lines give the daytime and evening hours during which this study was carried out.

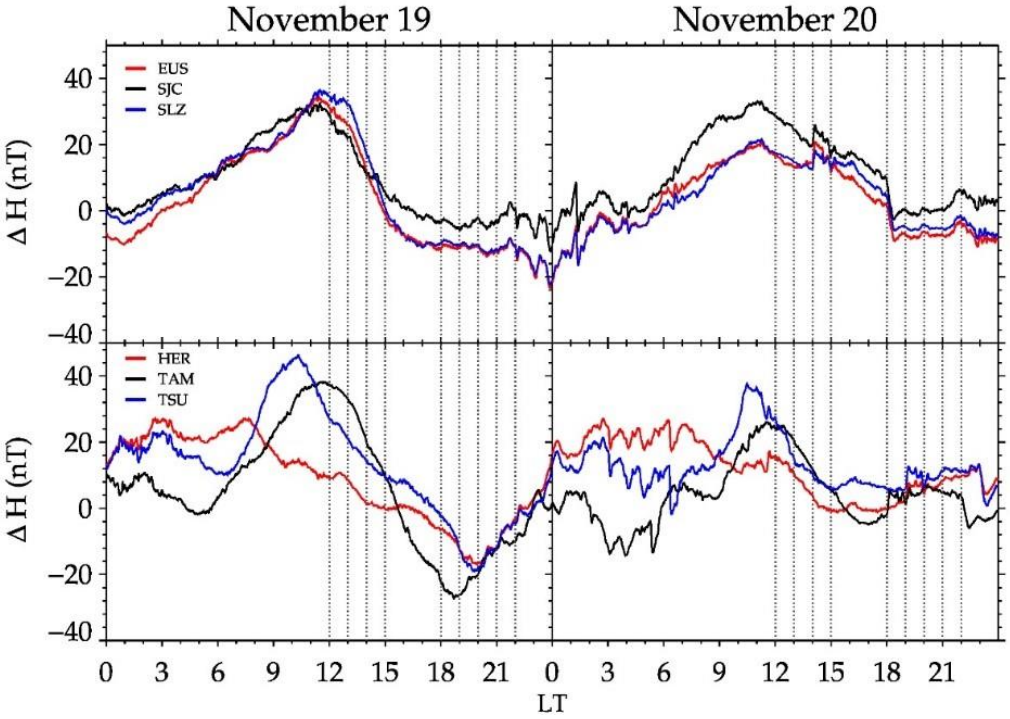

Source: Author

Figure 26, shows the daily ΔH variations for November 19 and November 20, 2018 for the Brazilian and African sectors. These two days with complete datasets for all stations were selected as a representation of a typical day-to-day variation of the selected period under study. In the upper panel, the red, black, and blue solid lines give the daily ΔH variations for EUS, SJC, and SLZ in the Brazilian sector respectively whilst in the lower panel, the red, black, and blue solid lines present the daily ΔH variations for HER, TAM, and TSU in the African sector respectively. The dotted lines running vertical in both panels give the daytime and evening hours during which we carried out this study. It can be seen that in the Brazilian sector, the daily variation for EUS, SJC, and SLZ during both November 19 and November 20 were in phase for the entire period. In the African sector also, the variations generally were in phase although some stations were out of phase during some hours. Furthermore, diurnal oscillations can be observed at almost all the stations for the two selected days in both sectors. These observed oscillations could be attributed to tidal components and also the superimposition of

short-period oscillations such as gravity waves (GW) or medium-scale traveling ionospheric disturbances (MSTIDs) and also long-period oscillations such as planetary waves (FAGUNDES et al., 2005).

In addition, we can see from Figure 26 that, the ΔH variations present synchronized wavelike oscillations especially in the Brazilian sector. These oscillations are neither flat nor random but tend to oscillate with specific periods, which relate to planetary waves and other waveforms. This gives us a good justification to proceed with our study because wave activities are present. Since the focus of this study is on planetary waves, the ΔH of the geomagnetic field is further organized into hourly bins for each day for the entire year under study which is a technique adapted from Fagundes et al. (2005). This was done because planetary waves are long-period oscillations with periods of days. Although this method of representing one value per day for each hour allows us to determine long-term series of daily ΔH variations independent of tidal components (FAGUNDES et al., 2005), it can be used to identify waves with periods of 3 days and above (CHEN, 1992; FAGUNDES et al., 2005; FORBES; ZHANG, 1997).

Figure 27 - ΔH daily variation at evening (18:00LT) from September to December 2018 (A) For the EUS (red), SJC (black), and SLZ (blue) at evening (18:00LT). (B) For the HER (red), TAM (black), and TSU (blue).

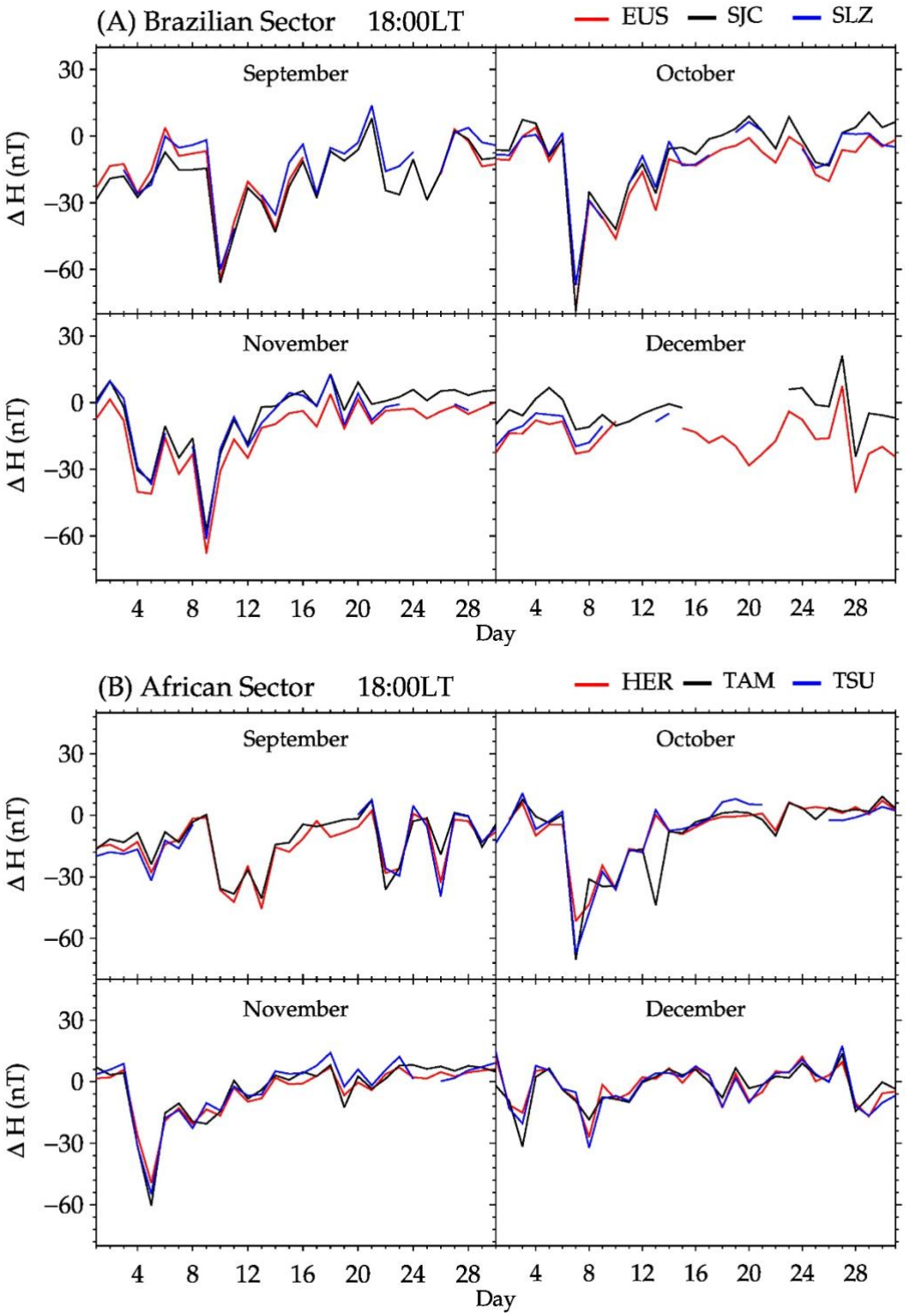

Source: Author

Figure 27 shows the ΔH daily variation for the Brazilian (EUS, SJC, and SLZ) and the African (HER, TAM, and TSU) sectors at evening (18:00LT) from September to December 2018. These four months were selected as an example to represent the oscillations on a daily basis as they had a more complete set of data for the stations used in the study. In both sectors as shown in Figure 27, periods of days are observed. These periods of days tend to present planetary wave-type oscillations. From September to December, very strong day-to-day ΔH variations are presented by both sectors. Furthermore, all the stations in both sectors are seen to be in phase. This trend makes it possible for us to proceed in calculating the average for all the stations in both sectors in order for us to get a general view of the day-to-day variability and behavior of planetary wave-type oscillations during 2018 and for the selected hours under study. However, for confidence in the method of averaging, we firstly investigated the periods present at each individual station. This enabled us to see the range of periods present at each station especially in the African sector where TAM is located in the northern hemisphere (see Figure 8). Generally, similar periods were presented by each station. In the African sector, we noted that although TAM is in the northern hemisphere, the periods it presented were similar to those presented by HER and TSU (in the southern hemisphere) which indicates that PW propagates in both hemispheres with similar periods. Figure 28 shows the wavelet spectrum for the average daily variation from Figure 27.

Figure 28 - ΔH daily average variation at evening (18:00LT) from September to December 2018 the (A) Brazilian and (B) African sectors

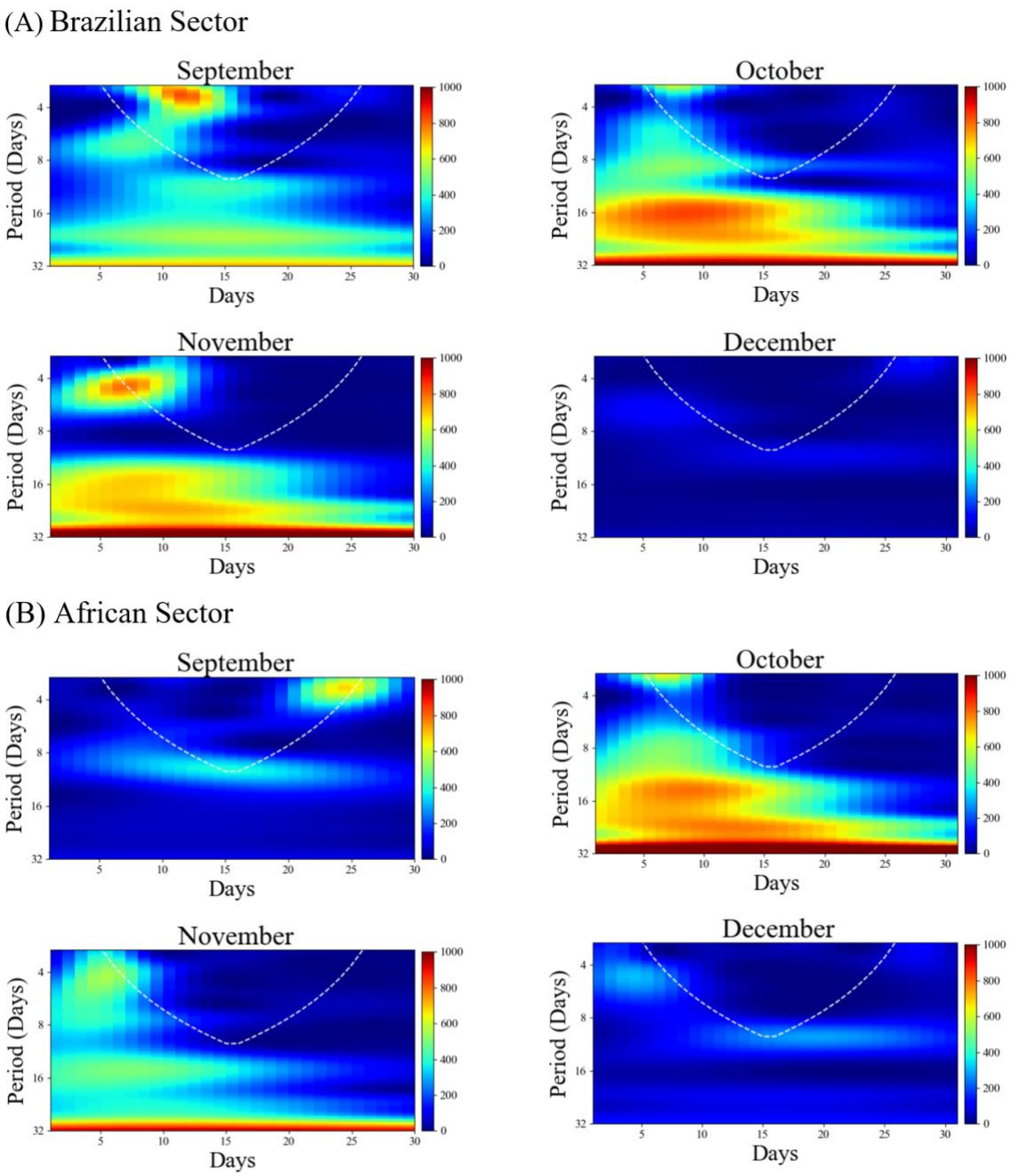

Source: Author

The wavelet results in Figures 28A and 28B show the periods present in the each of the selected month after we averaged the ΔH daily variation at evening (18:00LT) in Figures 27A and 27B. As observed in Figure 27, the oscillations presented by the stations were in phase, hence this made it possible for us to calculate the average for each sector in order to observe the periods present in each of the selected month at 18:00LT.

In this study, we considered selected daytime and evening (when PRE occurred) hours in Local Time (LT). PRE is an enhancement of the vertical E × B plasma drift that occurs around the equatorial region. This is due to the eastward electric field enhancement during the evening (post-sunset) around the magnetic equator (ABADI; OTSUKA; TSUGAWA, 2015; ABDU, 2012; FAGUNDES et al., 2009; GHOSH et al., 2020). Eccles et al. (2015) indicated that this enhancement can lift the F-region to higher altitudes. During and after the occurrence of PRE, its effects extend to the low and beyond EIA crest latitudes. Since the hours for the occurrence of PRE differed from station to station in Universal Time (UT) due to the differences in local time UT hours were converted to local times of 18:00 LT, 19:00 LT, 20:00 LT, 21:00 LT, and 22:00 LT (evening). The daytime hours were also converted into local time. This can be seen in Figure 27 where the time (18:00 LT) used for the plot is in LT. After the analysis, we determine the periods present in the analyzed data using spectral analysis. The results are presented in chapter 5.

This next section records the step-by-step methodology used to determine the planetary wave-type periods in the ionosonde installed at ARA and SJC (these stations are located at different latitudes) in the Brazilian sector. According to Takahashi et al. (2005), ionospheric F-layer base virtual height is sensitive to the local electric field. Particularly in the magnetic equator region, where the magnetic field is horizontal, the E×B effect is mainly responsible for the vertical movement of the virtual height. Therefore, based on this relationship, we employ the use of the ionosonde together with the magnetometer.

4.2 Ionosonde

To investigate the presence of wave-type oscillations with a period of days in the F-region which coincided with typical periods of PWs, the software known as UDIDA (UNIVAP Digital Ionosonde Data Analysis) which was developed by the Universidade do Vale do Paraíba is used. With this software, it is possible to visualize ionograms on a PC screen, perform scaling on the ionospheric parameters, and analyze the observed data. For this study, a tool provided by UDIDA, which provides the height variations at six fixed frequencies (3, 4, 5, 6, 7, and 8MHz) obtained in higher time resolution (100 s) was used (FAGUNDES et al., 2005). The 5 MHz fixed frequency was utilized in this study because it provided us with a very good dataset. The daytime and nighttime hours selected for the ionosonde analysis corresponded with the hours considered for the magnetometer. Also, for this study, the averages of the soundings recorded for each day were used. The *E* and *F* region second reflections were filtered out. This

technique was used because it allowed the determination of long-term time series of the daily height variations at fixed frequencies independent of the solar zenith angle effect and tidal components. The ionosonde data was also analyzed for us to see if the oscillations recorded in the virtual height variations were related to the oscillations in the magnetic field variations observed by the magnetometer in the ionosphere.

Figure 29 - Iso frequency obtained in São José dos Campos on May, 2018, showing the extraction of the PW parameters at 18:00LT at a frequency of 5MHz.

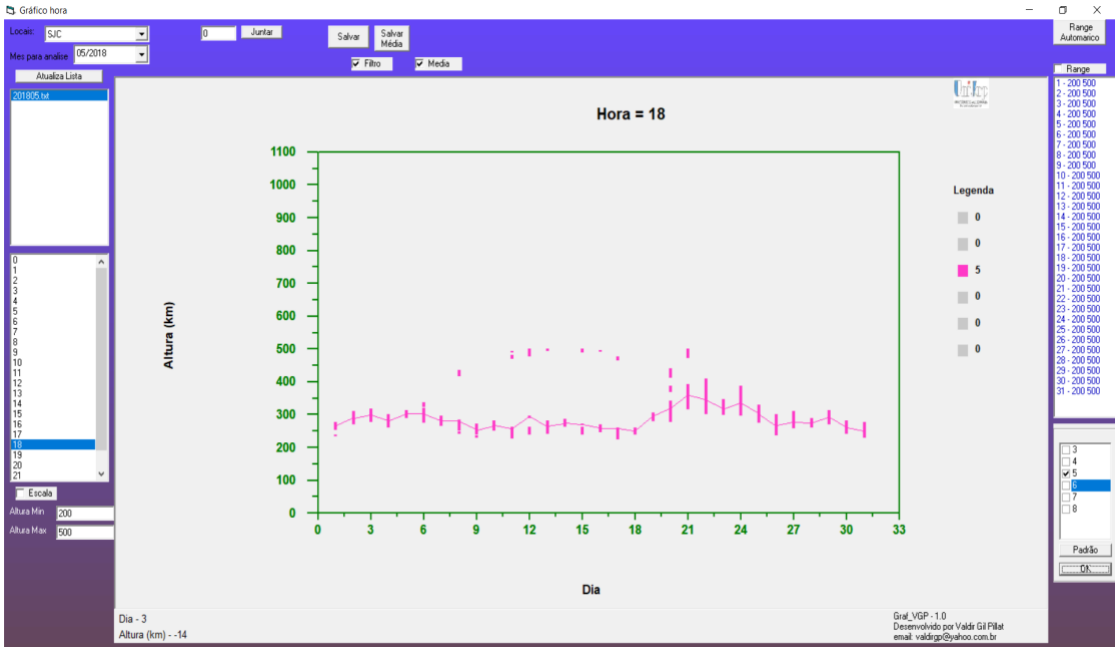

Source: Author

An Iso frequency describes points at/having the same frequency.

Figure 30 - The daily virtual height variation at evening (18:00LT) from September to December 2018 for ARA (red) and SJC (black) in the Brazilian sector.

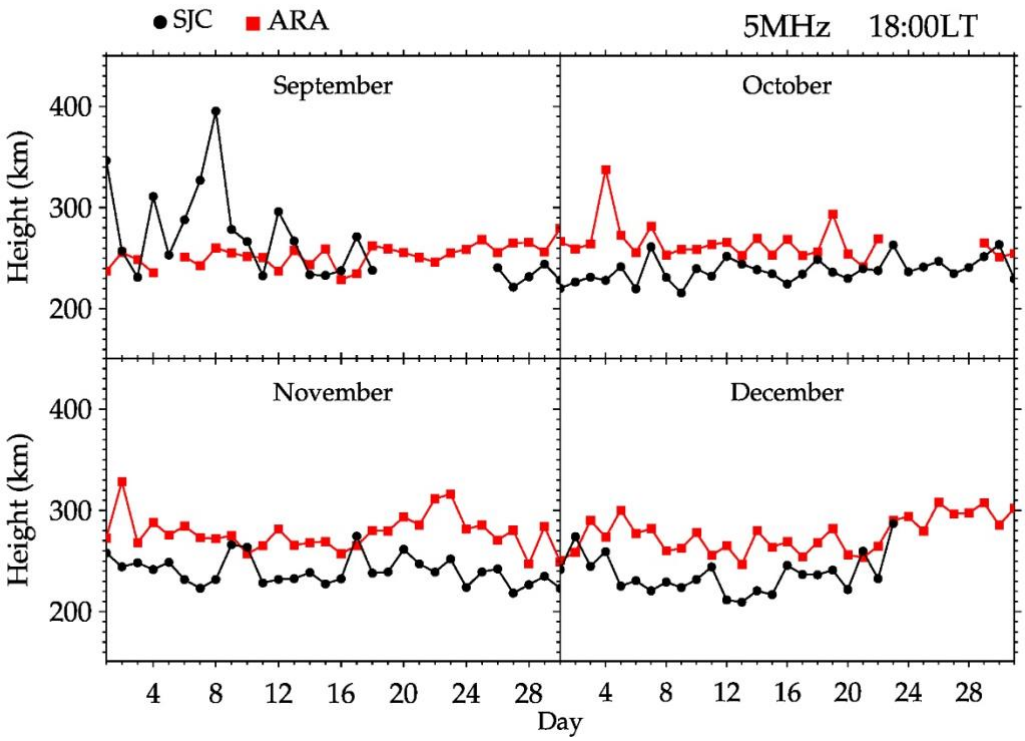

Source: Author

Figure 30 shows the day-to-day virtual height variation at evening from September to December, 2018 for ARA and SJC. Day-to-day height variations, which are not random but wave-like, can be seen in Figure 30. According to Fagundes et al. (2005), when the day-to-day height variations present random changes, it is possible that no wave activity is present; however, when wavy oscillations are present, the virtual height modulations could possibly be associated with planetary wave activities. Wavelet and Lomb-Scargle analysis were next applied to the results in order to identify the PW-type periods present.

The results of the analysis are presented in the subsequent Chapter.

5 RESULTS AND DISCUSSION

This chapter presents the results obtained from the step-by-step analysis carried out in the previous chapter. It further discusses these obtained results. Tidal wave results are first presented followed by results of planetary waves.

5.1 Atmospheric Tides

This section presents the results and discussion for atmospheric tides (solar and lunar (semidiurnal)).

5.1.1 Solar Tidal Results

Diurnal, Semidiurnal, and Terdiurnal components in the Brazilian and African sectors are presented and discussed in this section.

5.1.1.1 Brazilian Sector

Figure 31 - (A) Diurnal solar-tide amplitudes variation for quiet time (QT), (B) Diurnal solar-tide phase variation for quiet time (QT), (C) Diurnal solar-tide amplitude variation for disturbed + quiet time (D+QT), and (D) Diurnal solar-tide phase variation for disturbed + quiet time (D+QT) for three stations; SJC (solid black line), EUS (solid blue line), and SLZ (solid red line) in the Brazilian sector in 2018.

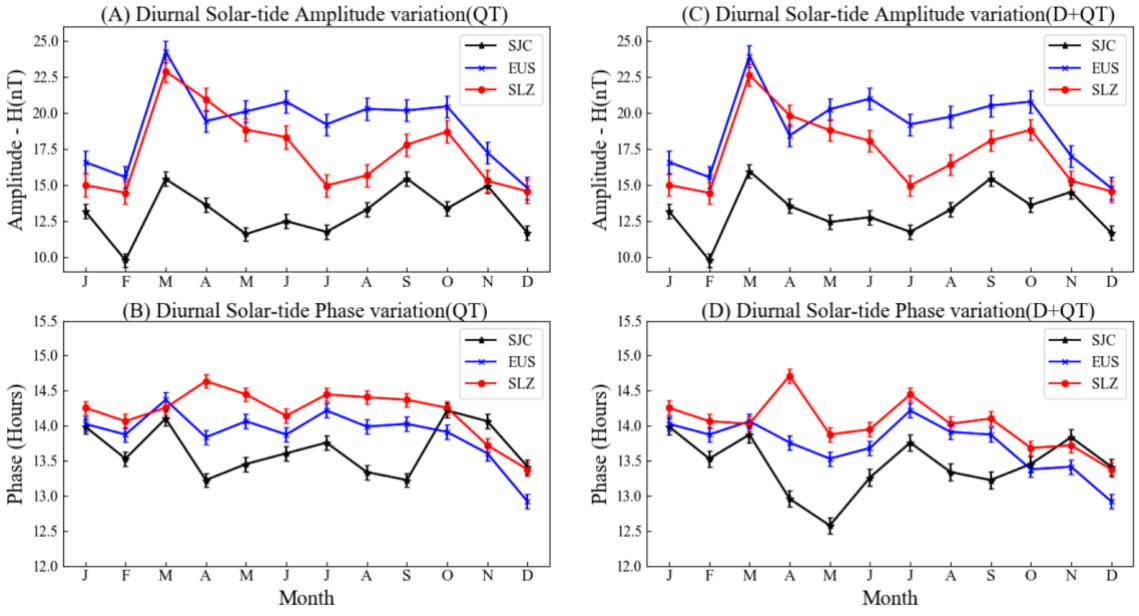

Source: Author

Figures 31A and 31B show the diurnal solar-tide amplitude and phase variations for the quiet time (QT) period in the magnetic field for SJC (solid black line), EUS (solid blue line), and SLZ (solid red line) in the Brazilian sector. The bars are the standard errors. The amplitudes (Figure 31A) for the QT present variabilities throughout the year with EUS attaining the maximum amplitude of around 24.3 nT in March which corresponded to a phase close to 14.5 hours in Figure 31B. SLZ also recorded the closest maximum amplitude variation of around 22.9 nT in March 2018. The minimum amplitude recorded during the QT was around 9.8 nT and with a phase of around 13.5 hours at SJC in February. In general, SJC registered the lowest amplitude values throughout the year, which was expected since EUS, and SLZ are located close to the geomagnetic equator (EEJ) whereas SJC is located away from it.

Figures 31C and 31D also give the diurnal solar-tide amplitude and phase variations for both the disturbed and quiet time (D+QT) for the aforementioned stations. For this D+QT, EUS still registers the maximum amplitude of around 24.0 nT, with SLZ also presenting 22.7 nT, in March and SJC registering the minimum amplitude of 9.8 nT in February 2018. It can be seen that there were little or no differences in amplitudes between the QT and the D+QT periods during the period of study. The amplitudes for SJC, EUS, and SLZ were in phase for most of the year except for some months. Fagundes et al. (2022) showed that during the storm time, amplitudes in this sector were in phase. The phases of both the QT and the D+QT periods are shown in Figure 31B and Figure 31D respectively with the maximum and minimum oscillating between 15 hours and 12.5 hours. The phases for the QT and D+QT in EUS and SLZ were mostly in phase. Generally, SJC led EUS and SLZ in phase, especially between April and September during the quiet time.

Figure 32 - (A) Semidiurnal solar-tide amplitudes variation for quiet time (QT), (B) Semidiurnal solar-tide phase variation for quiet time (QT), (C) Semidiurnal solar-tide amplitude variation for disturbed + quiet time (D+QT), and (D) Semidiurnal solar-tide phase variation for disturbed + quiet time (D+QT) for three stations; in SJC (dashed black line), EUS (solid blue line), and SLZ (solid red line) in the Brazilian sector in 2018.

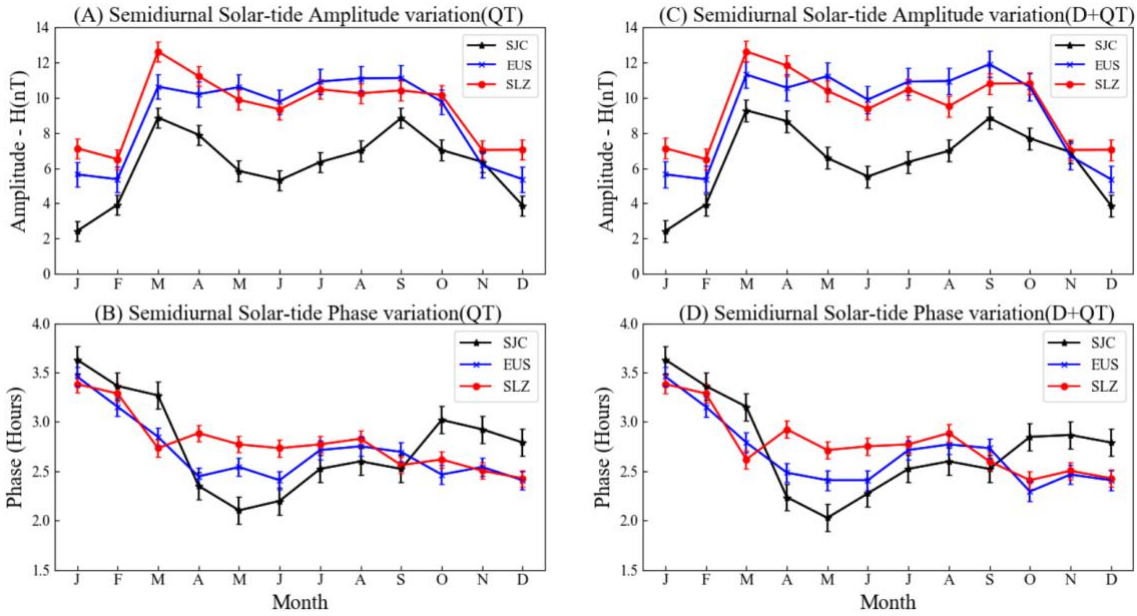

Source: Author

Figure 32A shows the semidiurnal solar-tide amplitude variation for the quiet time (QT) period in the magnetic field for SJC (dashed black line), EUS (solid blue line), and SLZ (solid red line) in the Brazilian sector. The amplitudes for the QT present variabilities throughout the year with SLZ attaining the maximum amplitude of around 12.6 nT in March. EUS also recorded the next maximum amplitude variation of around 10.6 nT in March 2018. The minimum amplitude recorded during the QT was around 2.4 nT at SJC in January 2018. In general, SJC also registered the lowest amplitude recordings throughout the year understudy for the semidiurnal components. Figure 32C gives the three stations' semidiurnal solar-tide amplitude variation for both the disturbed and quiet time (D+QT). During D+QT, SLZ still registers the maximum amplitude of around 11.3 nT, with EUS also presenting 9.3 nT, in March and SJC registering the minimum amplitude of 2.4 nT in January 2018. It can be seen that there are little or no differences in amplitudes between the QT and the D+QT periods. The three stations' amplitudes for the QT and the D+QT periods were all in phase throughout the year. The phases of both the QT and the D+QT periods are shown in Figure 32B and Figure 32D respectively with the maximum and minimum oscillating between 3.75 hours in January and

2.0 hours in May. The phases of the three stations for both the QT and the D+QT are seen to be in phase, especially SJC and EUS.

Figure 33 - (A) Terdiurnal solar-tide amplitudes variation for quiet time (QT), (B) Terdiurnal solar-tide phase variation for quiet time (QT), (C) Terdiurnal solar-tide amplitude variation for disturbed + quiet time (D+QT), and (D) Terdiurnal solar-tide phase variation for disturbed + quiet time (D+QT) for three stations; in SJC (solid black line), EUS (solid blue line), and SLZ (solid red line) in the Brazilian sector in 2018.

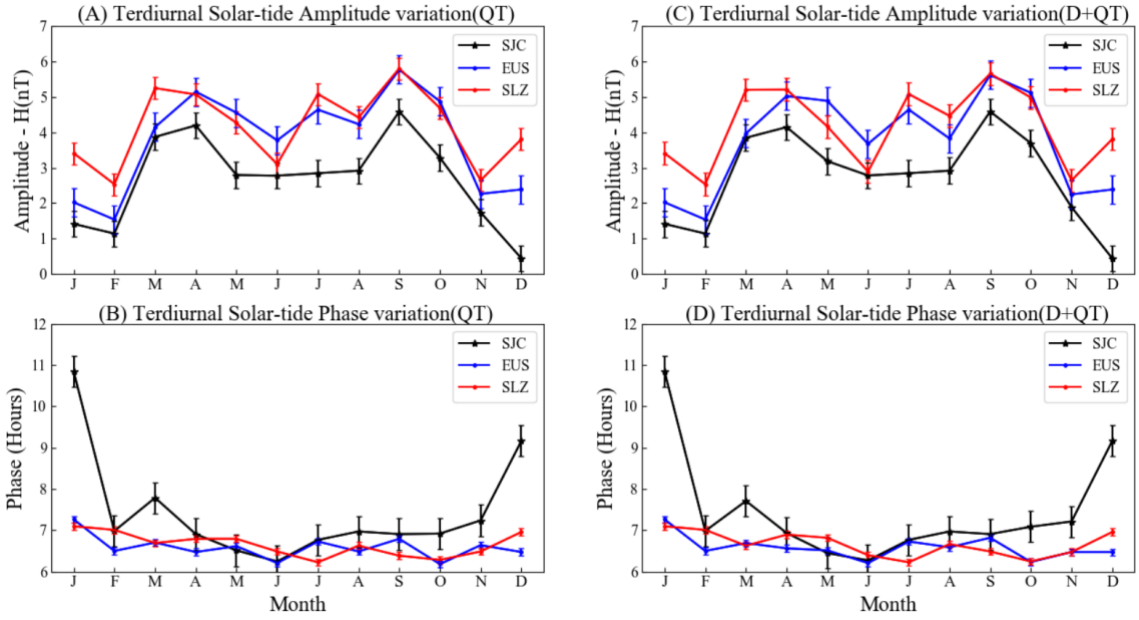

Source: Author

Figure 33A shows the terdiurnal solar-tide amplitude variation for the quiet time (QT) period in the magnetic field for SJC (dashed black line), EUS (solid blue line), and SLZ (solid red line) in the Brazilian sector. The amplitudes for the QT present variabilities throughout the year with SLZ attaining the maximum amplitude of around 5.8 nT in September. EUS recorded the next maximum amplitude variation of around 5.7 nT in September 2018. The minimum amplitude recorded during the QT was around 0.5 nT at SJC in December 2018. Throughout the year, SJC recorded the lowest amplitudes for the terdiurnal components during QT. Figure 33C presents the terdiurnal solar-tide amplitude variation for both the disturbed and quiet time (D+QT) for the three stations in the Brazilian sector. During the D+QT, SLZ still registers the maximum amplitude of around 11.3 nT, with EUS also presenting 9.3 nT, in March and SJC registering the minimum amplitude of 2.4 nT in January 2018. We can see clearly this trend in both the QT and QT+DT and this has been explained in the preceding sections. From Figure

33A and Figure 33C, it is seen that there are little differences in amplitudes between the QT and the D+QT periods. The phases of both the QT and the D+QT periods are shown in Figure 33B and Figure 33D respectively with the maximum and minimum oscillating between 11.0 hours in January and 6.0 hours in June. The highest phase occurred at SJC at 10.8 hours and the lowest phase occurred at EUS at 6.2 hours.

Since SLZ and EUS (near-equatorial stations) are located close to the geomagnetic equator, it is not unexpected that we observe such strong solar tidal oscillations in the magnetic field all year round. Although SJC (low latitude station) recorded interesting amplitudes also, it was seen as smaller which is also not unexpected since SJC is located further away from the magnetic field. This pattern is seen in all solar tidal oscillations observed in this study.

5.1.1.2 African Sector

Figure 34 - Diurnal solar-tide amplitudes variation for quiet time (QT), (B) Terdiurnal solar-tide phase variation for quiet time (QT), (C) Diurnal solar-tide amplitude variation for disturbed + quiet time (D+QT), and (D) Diurnal solar-tide phase variation for disturbed + quiet time (D+QT) for three stations; in HER (solid black line), TAM (solid blue line), and TSU (solid red line) in the African sector in 2018.

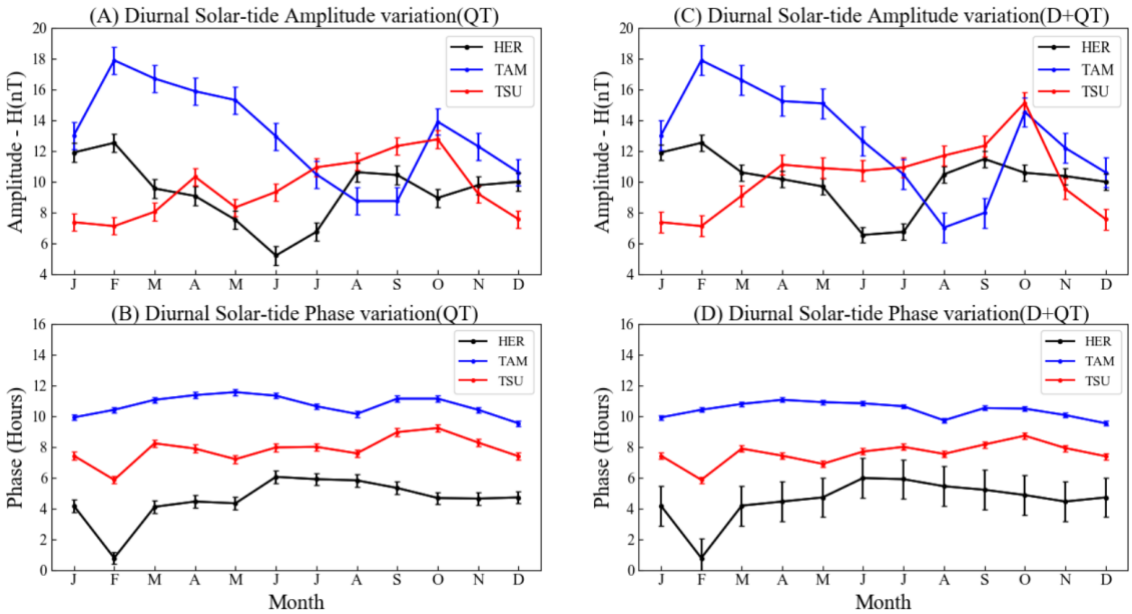

Source: Author

Figure 34A shows the diurnal solar-tide amplitude variation for the quiet time (QT) period in the magnetic field for HER (dashed black line), TAM (solid blue line), and TSU (solid red line) in the African sector. The amplitudes for the QT present variabilities throughout the

year with TAM obtaining the maximum amplitude of around 17.9 nT in February. TSU also recorded the next maximum amplitude variation of around 12.8 nT in October 2018. HER also attained a maximum amplitude of 12.6 nT which occurred in February. The minimum amplitude recorded during the QT was around 5.2 nT at HER in June 2018. In general, HER registered the lowest amplitude values throughout the year. Figure 34C gives the diurnal solar-tide amplitude variation for both the disturbed and quiet time (D+QT) for the aforementioned stations. For the D+QT, TAM registered the maximum amplitude of around 17.9 nT in February, with TSU also presenting 15.2 nT, in November and HER registering the minimum amplitude of 6.6 nT in June 2018. It can be seen that there are little differences in amplitudes between the QT and the D+QT periods. The phases of both the QT and the D+QT periods are shown in Figure 34B and Figure 34D with the maximum and minimum phases oscillating between 12 hours and 0.2 hours respectively.

Figure 35 - (A) Semidiurnal solar-tide amplitudes variation for quiet time (QT), (B) Terdiurnal solar-tide phase variation for quiet time (QT), (C) Semidiurnal solar-tide amplitude variation for disturbed + quiet time (D+QT), and (D) Semidiurnal solar-tide phase variation for disturbed + quiet time (D+QT) for three stations; in HER (solid black line), TAM (solid blue line), and TSU (solid red line) in the African sector in 2018.

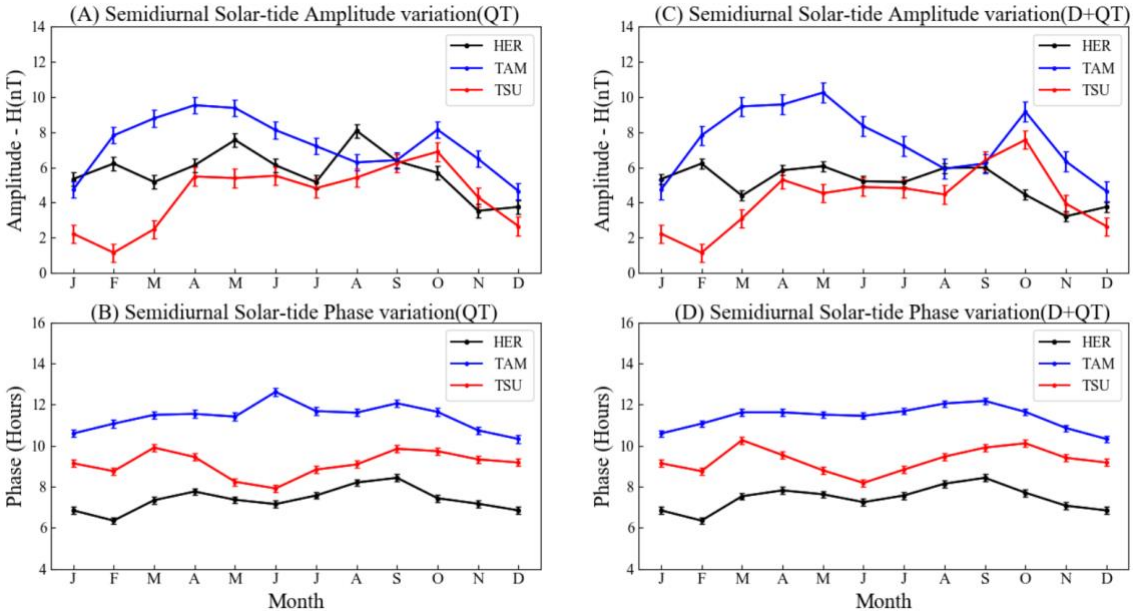

Source: Author

Figure 35A presents the semidiurnal solar-tide amplitude variation for the quiet time (QT) period in the magnetic field for HER (dashed black line), TAM (solid blue line), and TSU (solid red line) in the African sector. The amplitudes for the QT show variabilities throughout

the year with TAM obtaining the maximum amplitude of around 9.5 nT in April. HER recorded the second highest maximum amplitude variation of around 8.1 nT in August 2018. TSU also attained a maximum amplitude of 6.9 nT which occurred in October. The minimum amplitude recorded during the QT was around 1.2 nT at TSU in February 2018. During this QT period, TSU registered the lowest amplitude values for the year for this component. Figure 35C gives the diurnal solar-tide amplitude variation for both the disturbed and quiet time (D+QT) for the aforementioned stations. For the D+QT, TAM still registered the maximum amplitude of around 10.3 nT in May, with TSU also presenting 7.6 nT, in October and HER registering the maximum amplitude of 6.2 nT in February. The minimum amplitude for this period was recorded at TSU and was 1.2 nT in June 2018. It can be seen that, similarities in amplitudes between the QT and the D+QT periods. The phases of both the QT and the D+QT periods are shown in Figure 35B and Figure 35D with the maximum and minimum phases oscillating between 12.5 hours and 6.0 hours respectively.

Figure 36 - (A) Terdiurnal solar-tide amplitudes variation for quiet time (QT), (B) Terdiurnal solar-tide phase variation for quiet time (QT), (C) Terdiurnal solar-tide amplitude variation for disturbed + quiet time (D+QT), and (D) Terdiurnal solar-tide phase variation for disturbed + quiet time (D+QT) for three stations; in HER (solid black line), TAM (solid blue line), and TSU (solid red line) in the African sector in 2018.

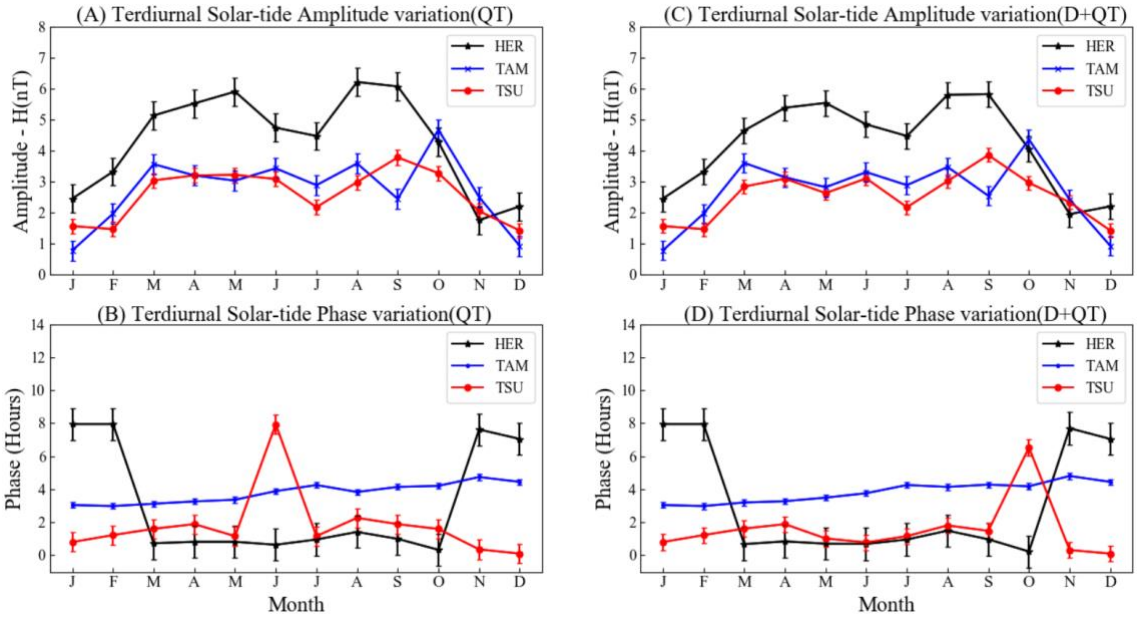

Source: Author

Figure 36A presents the Terdiurnal solar-tide amplitude variation for the quiet time (QT) period in the magnetic field for HER (dashed black line), TAM (solid blue line), and TSU (solid

red line) in the African sector. The amplitudes for the QT show variabilities throughout the year with HER obtaining the maximum amplitude of around 6.2 nT in August. TAM also had a maximum amplitude variation of around 4.7 nT in October 2018. TSU also attained its maximum amplitude of 3.8 nT in September. The minimum amplitude recorded during the QT was around 0.78 nT at TAM in January 2018. During this QT period, TSU registered consistently low amplitude values for the year for this component. Figure 36C gives the diurnal solar-tide amplitude variation for both the disturbed and quiet time (D+QT) for the aforementioned stations. For this D+QT, HER still registered the maximum amplitude of around 6.2 nT in August, with TAM also presenting 4.7 nT in October, and TSU registering its maximum amplitude of 3.8 nT in September. The minimum amplitude for this period was recorded at TSU and was 0.8 nT in January 2018. It can be seen that, similarities in amplitudes between the QT and the D+QT periods. The phases of both the QT and the D+QT periods are shown in Figure 36B and Figure 36D with the maximum and minimum phases oscillating between 8.0 hours and 0.2 hours respectively.

5.1.1.3 Solar Tidal variation in 2018 for the Brazilian and African Sectors during geomagnetic quiet time (QT) and geomagnetic disturbed and quiet time (D+QT)

Figure 37 - (A) Diurnal Solar-tide amplitudes variation for quiet time (QT), (B) Diurnal Solar-tide phase variation for quiet time (QT), (C) Diurnal Solar-tide amplitude variation for disturbed + quiet time (D+QT) and (D) Diurnal Solar-tide phase variation for disturbed + quiet time (D+QT) for six stations; TSU (solid black line), TAM (solid blue line), and HER (solid red line) in the African sector and SLZ (dashed Maroon line), EUS (dashed yellow line), and SJC (dashed green line) in the Brazilian sector in 2018.

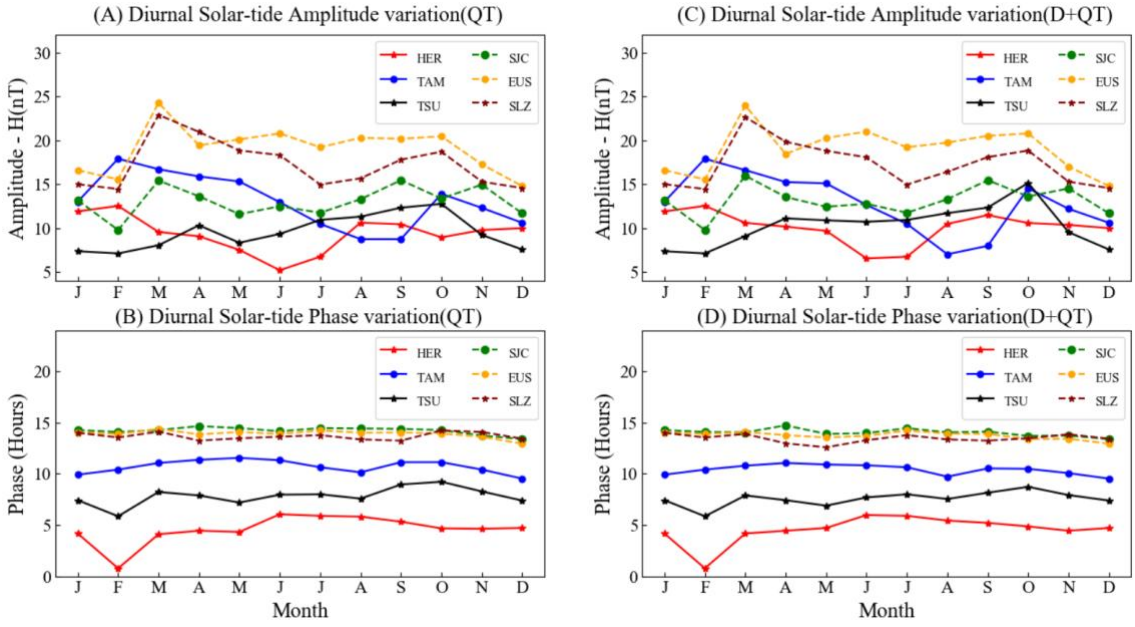

Source: Author.

Figure 37 shows the diurnal solar-tide amplitude variation for the quiet time QT and QT+DT period also their phases in the magnetic field. TSU (solid black line), TAM (solid blue line), and HER (solid red line) in the African sector, and SLZ (dashed Maroon line), EUS (dashed yellow line), and SJC (dashed green line) in the Brazilian sector in 2018.

Figure 38 - (A) Semidiurnal Solar-tide amplitudes variation for quiet time (QT), (B) Semidiurnal Solar-tide phase variation for quiet time (QT), (C) Semidiurnal Solar-tide amplitude variation for disturbed + quiet time (D+QT) and (D) Semidiurnal Solar-tide phase variation for disturbed + quiet time (D+QT) for six stations; TSU (solid black line), TAM (solid blue line), and HER (solid red line) in the African sector and SLZ (dashed Maroon line), EUS (dashed yellow line), and SJC (dashed green line) in the Brazilian sector in 2018.

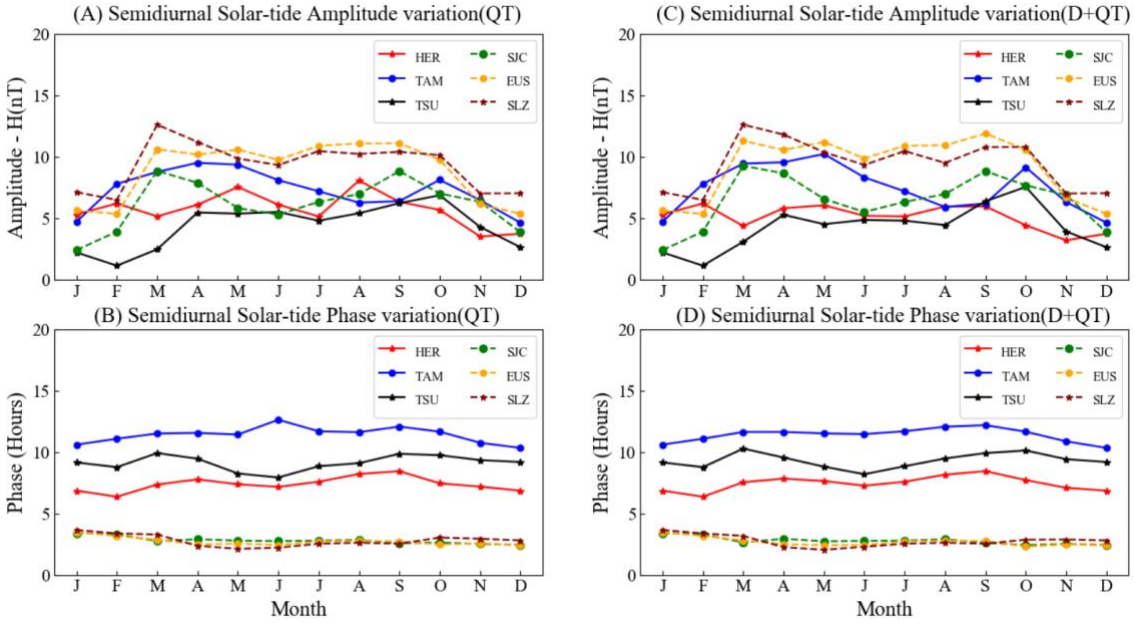

Source: Author

Figure 38 presents the semidiurnal solar-tide amplitude variation for the quiet time QT and QT+DT period also their phases in the magnetic field for TSU (solid black line), TAM (solid blue line), and HER (solid red line) in the African sector and SLZ (dashed Maroon line), EUS (dashed yellow line), and SJC (dashed green line) in the Brazilian sector in 2018.

Figure 39 - (A) Terdiurnal Solar-tide amplitudes variation for quiet time (QT), (B) Semidiurnal Solar-tide phase variation for quiet time (QT), (C) Terdiurnal Solar-tide amplitude variation for disturbed + quiet time (D+QT) and (D) Terdiurnal Solar-tide phase variation for disturbed + quiet time (D+QT) for six stations; TSU (solid black line), TAM (solid blue line), and HER (solid red line) in the African sector and SLZ (dashed Maroon line), EUS (dashed yellow line), and SJC (dashed green line) in the Brazilian sector in 2018.

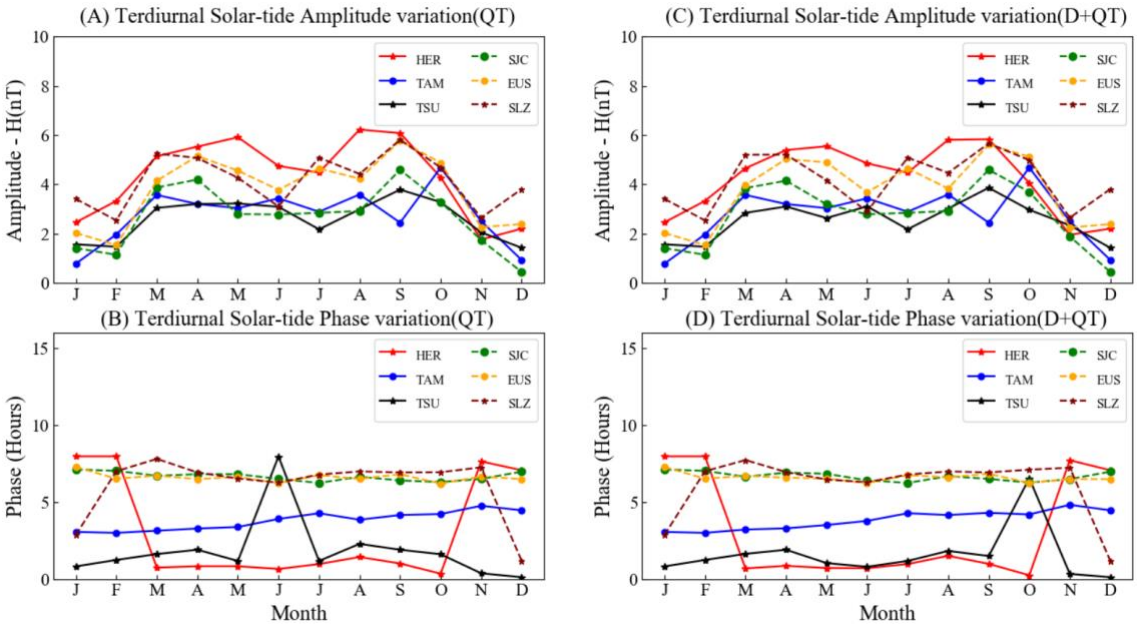

Source: Author

Figure 39 shows the terdiurnal solar-tide amplitude variation for the quiet time QT and QT+DT period also their phases in the magnetic field for TSU (solid black line), TAM (solid blue line), and HER (solid red line) in the African sector, and SLZ (dashed Maroon line), EUS (dashed yellow line), and SJC (dashed green line) in the Brazilian sector in 2018.

Solar tides, which are thermal in origin, are known to dominate atmospheric (ionospheric) tides (LAŠTOVIČKA, 1997). The most important of these tidal oscillations are the solar diurnal (24-hours) and the solar semidiurnal (12-hours) tides although the terdiurnal (8-hours) tide and other higher harmonics also play a role in the coupling of the atmosphere/ionosphere. However, although the terdiurnal amplitudes are usually smaller, they can reach large amplitudes at times (THAYAPARAN, 1997). The diurnal tidal oscillations usually dominate in the atmosphere but between 90-100 km, the semidiurnal tide seems to dominate (LAŠTOVIČKA, 1997; TITHERIDGE, 1995). Also, according to Laštovička (1997), at low latitudes and below 150 km, the diurnal tide is the component that generally dominates with the semidiurnal tide usually dominating at middle to high latitudes with terdiurnal tide

contributions (MANSON et al., 2009). In the ionosphere, these tides are very important, as they are known to drive the dynamo process/currents. In this present study, we consider the three solar tidal components and their amplitudes and phases as recorded by the ground-based magnetometer installed at six different stations in the Brazilian and African sectors. The diurnal solar-tide variation in Figure 32 for the three Brazilian stations during both the QT and QT+DT showed very high amplitudes compared with the semidiurnal solar-tide amplitudes in Figure 33 for the same sector. This result is expected since according to tidal theory diurnal solar tides usually dominate atmospheric tides and therefore usually present much larger amplitudes than the semidiurnal tidal amplitudes. The values for both the QT and QT+DT however oscillated around the same range since the solar activity during 2018 was mostly quiet hence the little difference. The semidiurnal solar tide variations also generally presented higher amplitude values compared with the terdiurnal solar tide, which was also expected since the terdiurnal solar tide usually only, dominates in the high-latitude ionospheric E-region (HOCKE, 1996; LAŠTOVIČKA, 1997). In the African sector also, a similar trend can be seen. The diurnal solar-tide amplitudes for both the QT and QT+DT were also larger than the semidiurnal solar-tide QT and QT+DT amplitudes and also the semidiurnal solar-tide QT and QT+DT amplitudes were also higher than the terdiurnal solar-tide QT and QT+DT. EUS and SJC presented the highest amplitudes among the six stations with TAM also presenting the third-highest amplitudes. A similar trend is observed throughout the year for QT+DT for all stations. Phases presented by the Brazilian sector oscillated between 0 to 24 hours for both the QT and QT+DT whereas, for the African sector, the phases oscillated between 0 to 20 hours. The semidiurnal solar tide also presented similar oscillations as the diurnal oscillation whereby the highest amplitudes were recorded at EUS and SJC, both in the Brazilian sector while TAM in the African sector presented the third-highest oscillation. Also, TSU in the African sector presented the lowest amplitude values. These trends were the same for the QT and QT+DT. However, the phases presented a reverse trend whereby the phases in the African sector oscillated between 0 to 10 hours whereas the Brazilian sector oscillated between 2 to 12 hours. For the terdiurnal amplitude variation, HER in the African sector and EUS and SJC in the Brazilian sector presented the highest values whereas TSU in the African sector consistently presented the lowest amplitude variations both for the QT and QT+DT throughout the year 2018. Various studies have established that tidal amplitudes vary with latitudes (CHAPMAN; LINDZEN, 1969; FORBES, 1995; FRIEDMAN et al., 2009). For the diurnal components studied, the low latitude stations (EUS and SLZ in the Brazilian sector and TAM in the African sector) presented the highest amplitude variations all year which Manson et al. (1989) found in their study.

However, although the semidiurnal tide in the low latitude sector (EUS, SLZ, and TAM) also presented high amplitude variations during the period of our study, Manson et al. (1989) stated this behavior was seen in the middle and high latitude sectors. It is also important to point out that, all the three components almost presented semiannual variations in all the sectors.

It is also well known that, the closer a station is to the geomagnetic equator, the larger the range of variation recorded (REDDY, 1989), and this characteristic has been attributed to the existence of a band of an intense electrical current centered at the dip equator and flowing 90-130 km height range known as the Equatorial Electrojet (REDDY, 1989). Hence the trend seen in two Brazilian stations closest to the geomagnetic equator. Also, in the African sector, a similar trend can be seen where, TAM which is also closest to the geomagnetic equator, presented higher amplitude values in the diurnal and semidiurnal solar tidal components. However, it is interesting to note that, this trend was not seen in the terdiurnal component in the African sector. The behavior of the terdiurnal solar tide at HER was unexpected since, it happened to be the station furthest from the geomagnetic equator in this study. However, the highest solar tidal terdiurnal amplitude variations during the entire year for both the QT and QT+DT were observed at this station. We do not have an explanation however, for why this deviation from the norm was seen.

Seasonal variations can be seen in both sectors throughout the year. The maximum (QT and QT+DT) amplitude (diurnal solar-tide) for all six stations which was recorded in the Brazilian sector occurred during autumn (March) whereas the QT and QT+DT minimum amplitude values which were recorded in the African sector occurred during winter (June and July). For all the stations in this study, the maximum semidiurnal solar tide amplitude reached was recorded in the Brazilian sector during autumn (March) for both the QT and QT+DT. Additionally, the minimum amplitude attained was recorded in the African sector during the summer month of February. It can be seen that the maximum for the diurnal and the semidiurnal solar tide both occurred during the autumn season (March). In the terdiurnal component for all stations in both sectors, the maximum amplitude was attained in the African sector during winter (August) for both the QT and QT+DT whereas the minimum amplitude reached occurred in the Brazilian sector during summer (December) for both the QT and QT+DT. Interestingly, the minimum amplitudes for both the semidiurnal and terdiurnal components occurred during summer i.e. February and December respectively, however, in different sectors. Also, the three stations in the Brazilian sector and two stations in the African sector presented two distinct peaks throughout the year for all three stations for both the QT and QT+DT. The phases presented for both sectors for the terdiurnal component showed the Brazilian sectors presenting

lower phase values compared to the phases presented by the African sector with TAM in the northern hemisphere leading in phase throughout the year.

5.1.1.4 Latitudinal response of Solar Tidal components to the Sudden Stratospheric Warming (SSW) Event of February 2018

In February 2018 (year of Low Solar Activity), a major SSW occurred after a four-year hiatus in the Northern Hemisphere. Sudden Stratospheric Warmings (SSW) are known to be large-scale impressive and spectacular fluid dynamical polar wintertime events that occur during extended winter and almost exclusively at high latitudes (BALDWIN et al., 2021; SIDDIQUI et al., 2018; VIEIRA et al., 2022). The breaking of planetary-scale waves that propagate upwards from the troposphere cause these SSWs. During SSWs, the normally strong wintertime westerly stratospheric circulation breaks down in a few days and is replaced by weak easterly winds (BALDWIN et al., 2021). Also, there are large and rapid temperature increases in the winter polar stratosphere (~10–50 km) and are associated with a complete reversal of the climatological wintertime westerly winds.

Figure 40 shows the evolution of the vortex in the stratosphere, before, during, and after the SSW event of 2018. The MERRA 2 reanalysis data was obtained online from the website https://daac.gsfc.nasa.gov**.**

Figure 40 – Temperature and Wind Evolution of the Stratosphere before, during, and after the SSW event of 2018. (A) DOY 36-before event, (B) DOY 43-onset of event, (C) DOY 49-during event, and (D) DOY 64-after event. The black arrows give the wind direction.

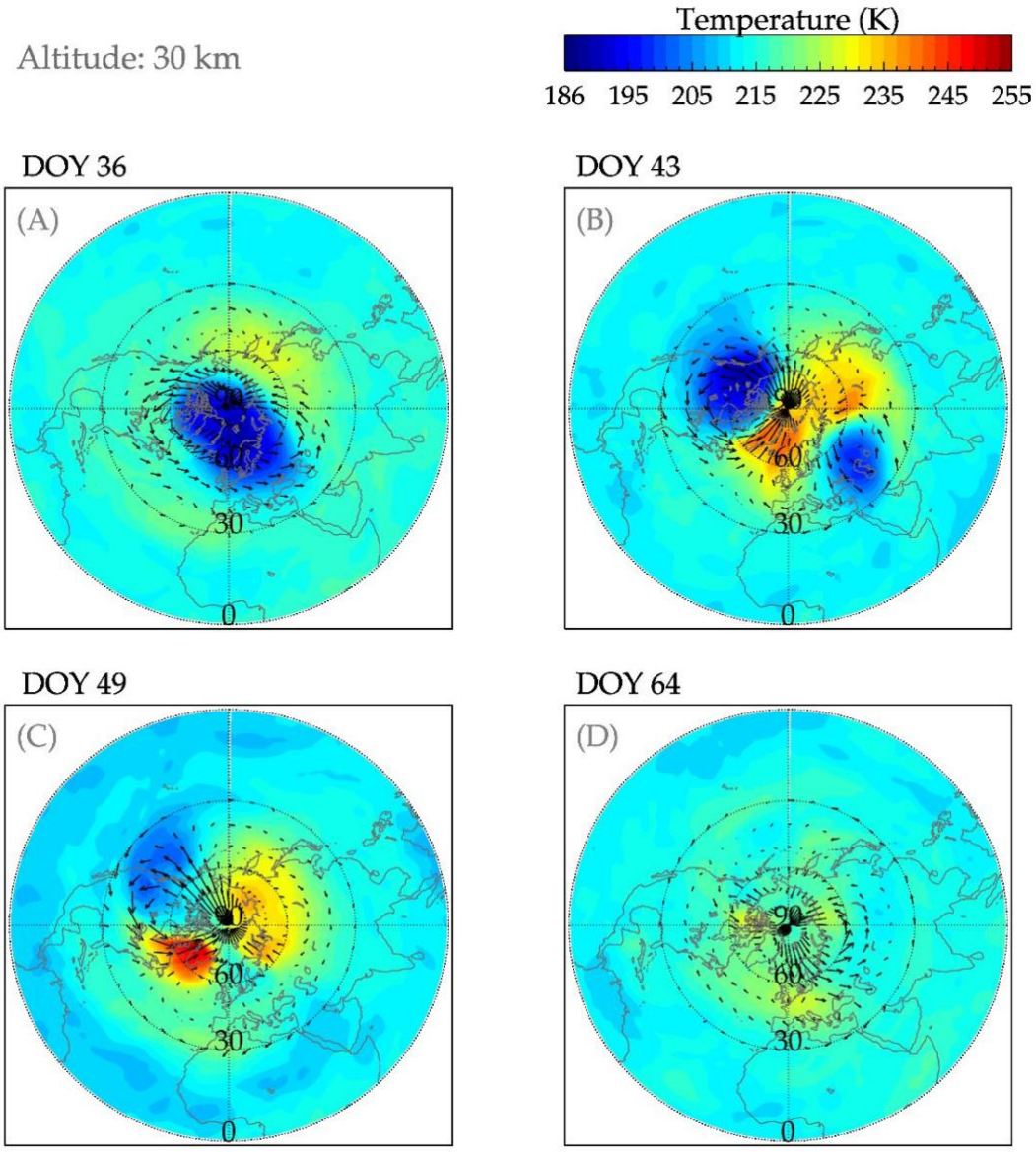

Source: Author

During winter in the Northern Hemisphere, as the temperature drops so does the pressure. With these colder temperatures over the pole, the temperature difference towards the south increases. This causes a strong pressure difference, and a large low-pressure cyclone-like circulation starts to develop across the Northern Hemisphere. This extends from the surface layers, far up into the stratosphere and is known as the polar vortex. This cyclone-like circulation together with the temperature before the onset of the SSW is shown in Figure 40A (depicted by the arrows going counter-clockwise) on DOY 36. During an SSW, the polar vortex

breaks down, accompanied by rapid descent and warming of air in polar latitudes, mirrored by ascent and cooling above the warming. SSWs affect the atmosphere above the stratosphere, producing widespread effects on atmospheric chemistry, temperatures, winds, neutral (non-ionized) particles and electron densities, and electric fields. These effects span both hemispheres and are observed across many different regions of the atmosphere (BALDWIN et al., 2021; PEDATELLA et al., 2018; SIDDIQUI et al., 2018).

In Figure 40C, a split in the vortex can still be seen as the temperature peaked on DOY 49. Figure 40D shows the gradual cooling of the stratosphere after the SSW event on DOY 64.

Figure 41 – Day-to-Day variations of the stratospheric parameters and geomagnetic indices during the SSW 2018 from DOY 36 to DOY 64. Panel 1- The temperature at 90°N and the historical mean temperature at 10 hPa (~30 km), Panel 2-Zonal wind speed, Panel 3 - PW1 and PW2 amplitude at 60°N, Panel 4 - F10.7 index, Panel 5 - Dst index, and Panel 6 - Kp index.

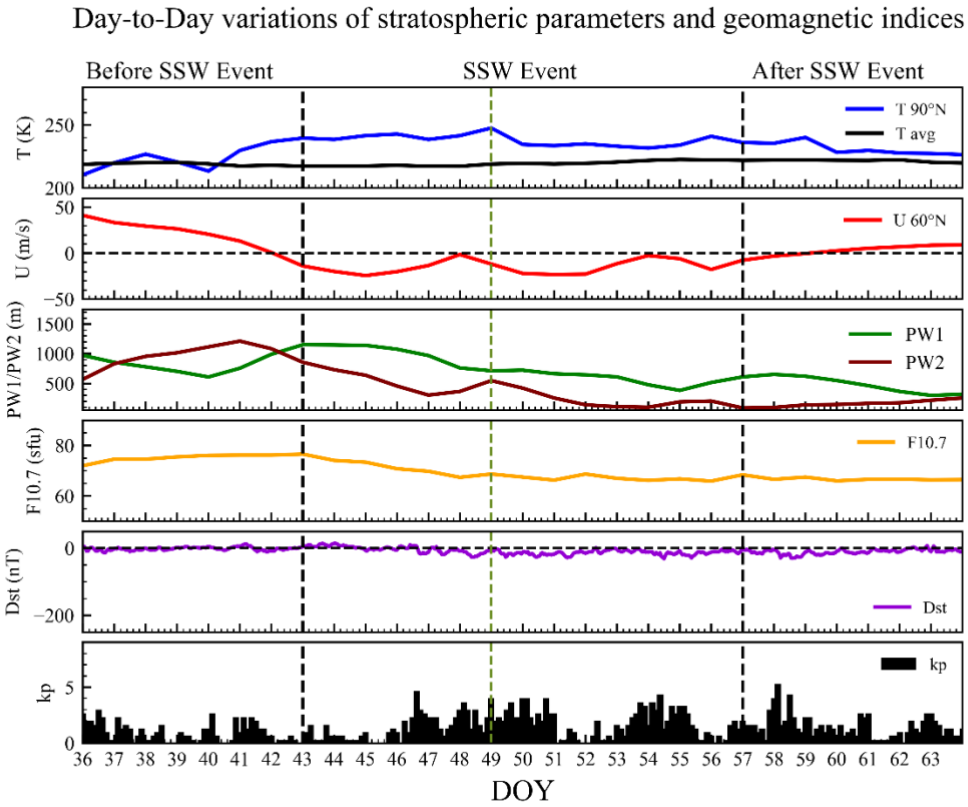

Source: Author

Panels one to six in Figure 41 show the day-to-day variations of the stratospheric temperature at 90°N and the historical mean/average temperature at 10hPa(~30 km). Zonal wind speed at 60°N (10 hPa), planetary waves 1 and 2 amplitudes of Geopotential Height at 60°, F10.7 solar flux, Dst index, and Kp index from DOY 36 to DOY 64 (February 05, 2018–

March 05, 2018). The data were obtained online from the websites, http://acdb-ext.gsfc.nasa.gov/Data_services/met/ann_data.html, http://omniweb.gsfc.nasa.gov/form/dx1.html, and http://wdc.kugi.kyoto-u.ac.jp/.

The black dashed lines running vertical indicate the beginning (DOY 43) and ending (DOY 57) of the SSW 2018, and the olive-drab dashed line indicates the date when the temperature at 90° N reached its peak value (DOY 49). The black dashed line running horizontal through panels 2 and 5 are the zero mark. This shows us the oscillations of the zonal mean wind and Dst index with respect to the zero mark. The 2018 SSW event corresponded to low solar activity (mean F10.7 = 69.6 sfu). According to Vieira et al. (2022), the criteria that decides the onset and end of an SSW event is the time when the temperature at 90°N crosses the historical mean temperature. The 2018 SSW can be classified as a major/strong event. Researchers have indicated that, minor warmings should only slow down the circulation but not reverse it, thus if the zonal wind is negative (easterlies), then a change in circulation took place and the polar vortex broke down (e.g., BLUME; MATTHES; HORENKO, 2012; LIMA et al., 2012 and references therein). This breakdown is shown in Figure 40B and Figure 41 (panel 2) where the zonal wind speed reversed from west to east. A split is seen in the vortex in 40B as the temperature at 90°N increased by about 32 K above the historical mean temperature (Figure 41-panel 1). Figure 41-panel 3 shows the PW1 and PW2 variations before, during, and after the SSW occurrence. This is another important parameter used to classify SSWs. This is because the formation of SSWs have been attributed to the upward growth of propagating transient planetary waves and their interaction with the zonal mean flow (LIMA et al., 2012). Therefore, predominantly wave 1 and wave 2 patterns tend to precede SSWs (BALDWIN et al., 2021; COHEN; JONES, 2011; GARFINKEL; BENEDICT; MALONEY, 2014; TUNG; LINDZEN, 1979; WOOLLINGS et al., 2010). It is noticed from panel 3 that, before the SSW, the PW1 is stronger than the PW2, however, both present enhancements, suggesting that the PW1 and PW2 intensifications triggered the SSW. During the SSW the PW1 and PW2 activity decreased steadily. Furthermore, during the SSW 2018 event no strong geomagnetic storms occurred, therefore, we can suggest that any ionospheric space-time disturbance during this period may be due to the SSW (VIEIRA et al., 2022).

SSWs are known to be strongly associated with diverse wave activities, such as planetary waves, lunar, and solar tides (e.g., CHAU et al., 2012; PEDATELLA; FORBES, 2010) hence, we proceed to study the latitudinal response/behavior of the solar tidal components to the SSW event of February, 2018. This is achieved by utilizing the methodology/approach by Bolzan et al. (2020) to separate the first three solar tidal

components/harmonics. The SSW occurred during a geomagnetically quiet time. The diurnal, semidiurnal, and terdiurnal solar tidal components calculated using wavelet analysis are presented in the first, second, and third rows respectively in Figures 42 and 43. These components were calculated using Daubechies (db4) wavelet functions. This technique splits and removes different periodicities based on interesting physical properties. Thus, in this work, we removed ripples and longer periodicities in the time series in order to enhance the tidal scales that are difficult to observe in the presence of these ripples and long-term periodicities. This technique has proved efficient in extracting the periodicities with greater energies compared with some other techniques.

Figure 42 – Panel 1 shows the latitudinal evolution of the diurnal solar tidal components at three latitudes (one Brazilian latitude and two African latitudes) with TAM as the blue line, SJC as the red line, and HER as the black line. Panel 2 is same as panel 1 but for the semidiurnal tidal component. Panel 3 is the same as panel 1 but for the terdiurnal tidal component.

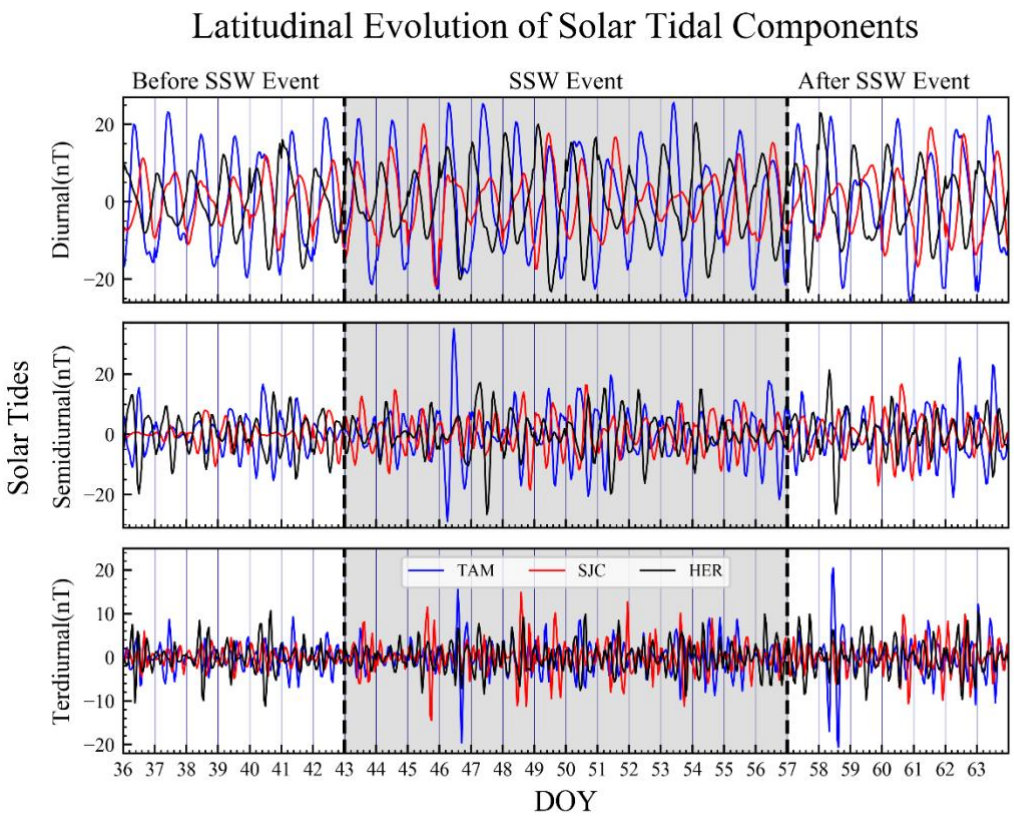

Source: Author

Figure 42, panels 1, 2, and 3 present the diurnal, semidiurnal, and terdiurnal solar tidal oscillations before, during, and after the SSW event of February 2018. These represent TAM, SJC, and HER which were chosen since they had an almost complete dataset for the SSW

occurrence period. Also, they all lie in different latitudes although SJC and HER are close (by latitude). TAM presents the strongest oscillations for all three components with some prominent and interesting peaks seen after the occurrence of the SSW event. This result can be seen in the wavelet power spectrum analysis in Figure 43.

Figure 43 – Wavelet Spectrum of STC's at three different latitudinal stations.

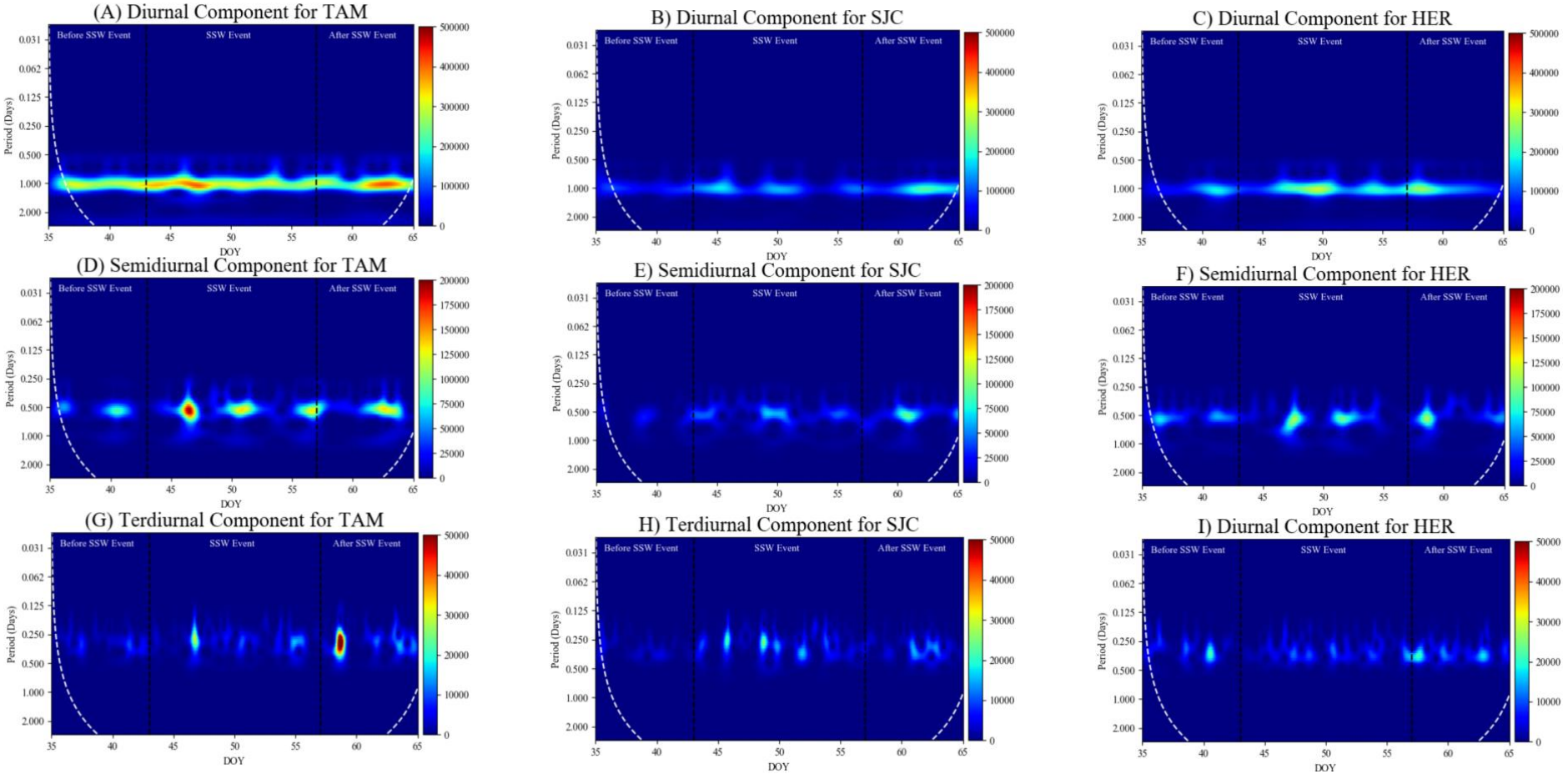

Source: Author

In Figure 43, the diurnal components are presented in the first row. Figure 43A is the wavelet spectrum of TAM, which is at the low-latitude same as SJC but different from HER. We look at the response of each of these different latitudinal stations. It is seen that TAM, which is close to the geomagnetic equator, presents some interesting solar diurnal response before, during, and after the SSW event of 2018. In Figure 43A, very strong diurnal responses are seen throughout the period under study compared to the oscillations in Figures 43B and 43C. A strong enhancement can be seen at the commencement of the SSW event in Figure 43A. This continues into some days after the commencement and then normalizes. After the SSW event, a strong enhancement is seen from about day 61 to 64. This behavior could be attributed to the occurrence of the SSW affecting the Equatorial Electrojet (EEJ) since Siddiqui et al. (2018), found that there is a solar tidal amplitude amplification prior to the onset of warmings, a reduction during the deceleration of the zonal mean zonal wind, and a second enhancement a few days after the peak reversal. Pedatella et al. (2016) have also reported an enhancement presented during SSWs by diurnal and semidiurnal solar tidal components, which is seen in Figures 43A, 43C, 43D, and 43F. In the diurnal and semidiurnal components at all the stations, enhancements however small are seen after the SSW occurrence which can be explained by Siddiqui et al. (2018), who found a second enhancement a few days after the peak reversal. The terdiurnal component at TAM presented an interesting feature whereby the strongest enhancement was seen after the SSW event.

5.1.2 Semidiurnal Lunar Tidal variation in the Brazilian and African Sectors

Lunar tides produce modifications in atmospheric pressure, magnetic and electric fields, electron density, and ionospheric (CHAPMAN; BARTELS, 1940; CHAPMAN; LINDZEN, 1969b; MATSUSHITA, 1967). These modifications considerably affect the dynamics of the atmosphere. The two types of lunar tides, which are usually studied, are the diurnal lunar tide and the semidiurnal lunar tide. However, the most important of these two occurs at the lunar semidiurnal period of 12.42 hours (FORBES; ZHANG, 2019) and can reach larger amplitudes. The study of the influence of the lunar semidiurnal tide in the ionosphere is important because it can increase and decrease the amplitude of the pre-reversal enhancement and the reversal time of the evening upward drifts in the equatorial ionosphere (PAULINO; BATISTA; CLEMESHA, 2012). These effects can change the raising of the evening F region layer height; therefore, they can modify the probability of occurrence of equatorial spread F, and change the amplitude of the Appleton anomaly (STENING; FEJER, 2001). In addition, during solar

minimum, much of the variabilities in the ionosphere were found to be caused by lunar tides (ECCLES et al., 2011). It is important to note however that, it is difficult to study these tides since other oscillations such as planetary waves, gravity waves, and solar tides can overlap with the lunar tides (DE MORAES et al., 2017). Atmospheric lunar tides are responsible for the ionospheric currents that produce the Lunar (*L)* variations on the ground (MAEDA; FUJIWARA, 1967; TARPLEY, 1970) hence our use of the magnetometer in this study.

In this section, we present and discuss the results for the semidiurnal lunar tide for stations in the Brazilian and African sectors.

5.1.2.1 Brazilian Sector

We group the into seasons of the year, that is summer, autumn, winter, and spring in order to see the behavior of lunar tides at the various stations.

Figure 44 - (A) Semidiurnal lunar-tide amplitudes variation for quiet time (QT), (B) Semidiurnal lunar-tide phase variation for quiet time (QT), (C) Semidiurnal lunar-tide amplitude variation for disturbed + quiet time (D+QT), and (D) Semidiurnal lunar-tide phase variation for disturbed + quiet time (D+QT) for three stations; in SJC (dashed black line), EUS (solid blue line), and SLZ (solid red line) in the Brazilian sector in 2018.

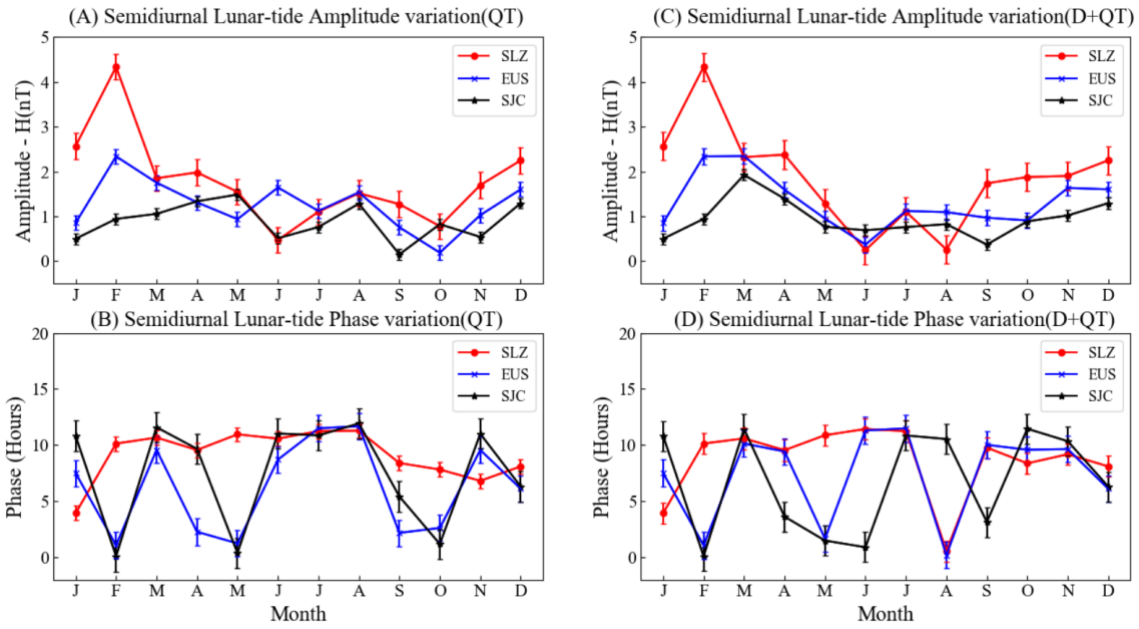

Source: Author

Figure 44A shows the annual semidiurnal lunar-tidal amplitude variation for the quiet time (QT) period in the magnetic field for SJC (dashed black line), EUS (solid blue line), and

SLZ (solid red line) in the Brazilian sector. The amplitudes for the QT present variations throughout the year with SLZ attaining the maximum amplitude of around 4.3 nT in February which is during the Summer month. EUS also attained its maximum amplitude value at around 2.3 nT in February 2018 with SJC attaining a maximum at 1.5 nT in May (Autumn). Both SLZ and EUS are located near the geomagnetic equator whereas the SJC is further away. According to Schlapp and Malin (1979)), amplitudes of the horizontal component will be affected by the distance of a station from the focus of a current system. In March and April (Autumn), a sharp reversal is seen at SLZ and EUS whereas, there is a gradual enhancement in the semidiurnal lunar tidal amplitude at SJC during the QT. Although the maximum amplitude was not recorded in January as reported by (BARTELS; JOHNSTON, 1940b; SCHLAPP, 1978), for SLZ and EUS, it was still during summer whereas for SJC it was during autumn. Changes in the magnetic variations with seasons are said to largely be due changes in the lunar atmospheric tide at ionospheric heights (STENING; RASTOGI, 2002). The minimum amplitude recorded during the QT for all the stations was around 0.2 nT at SJC in September 2018 which can be due to the fact that SJC is further away from the magnetic equator hence the latitudinal differences. Generally, SJC recorded the lowest amplitudes for the semidiurnal components during the QT.

Figure 44C presents the semidiurnal lunar-tidal amplitude variation for both the geomagnetically disturbed and quiet time (D+QT) period for the three stations in the Brazilian sector. During the D+QT, SLZ still registers the maximum amplitude of around 4.3 nT, with EUS also presenting 2.3 nT, in March and SJC registering a maximum of 1.9 nT in March. A minimum amplitude of 0.3 nT was recorded at SLZ in August 2018. This was the minimum-recorded value at D+QT for all the stations in the year under study. From Figure 44A and Figure 44C, it is seen that there are little differences in amplitudes between the QT and the D+QT periods since the amplitudes oscillated around the same values.

The phases of both the QT and the D+QT periods are shown in Figure 44B and Figure 44D respectively with the maximum and minimum oscillating between 0 hours and 12.5 hours. The phases at all the stations show seasonal variations whereby EUS and SJC are more in phase for the most part of the year during the QT. There is a gradual increase in phase during winter and a decline during autumn and an increase and decline in summer at EUS and SJC. At SLZ, the phase consistently lags EUS and SJC for the most part of the year except for some months. The results for the African sector are presented in the next section.

5.1.2.2 African Sector

Figure 45 - (A) Semidiurnal lunar-tide amplitudes variation for quiet time (QT), (B) Semidiurnal lunar-tide phase variation for quiet time (QT), (C) Semidiurnal lunar-tide amplitude variation for disturbed + quiet time (D+QT) and (D) Semidiurnal lunar-tide phase variation for disturbed + quiet time (D+QT) for three stations; in TSU (solid black line), TAM (solid blue line), and HER (solid red line) in the African sector in 2018.

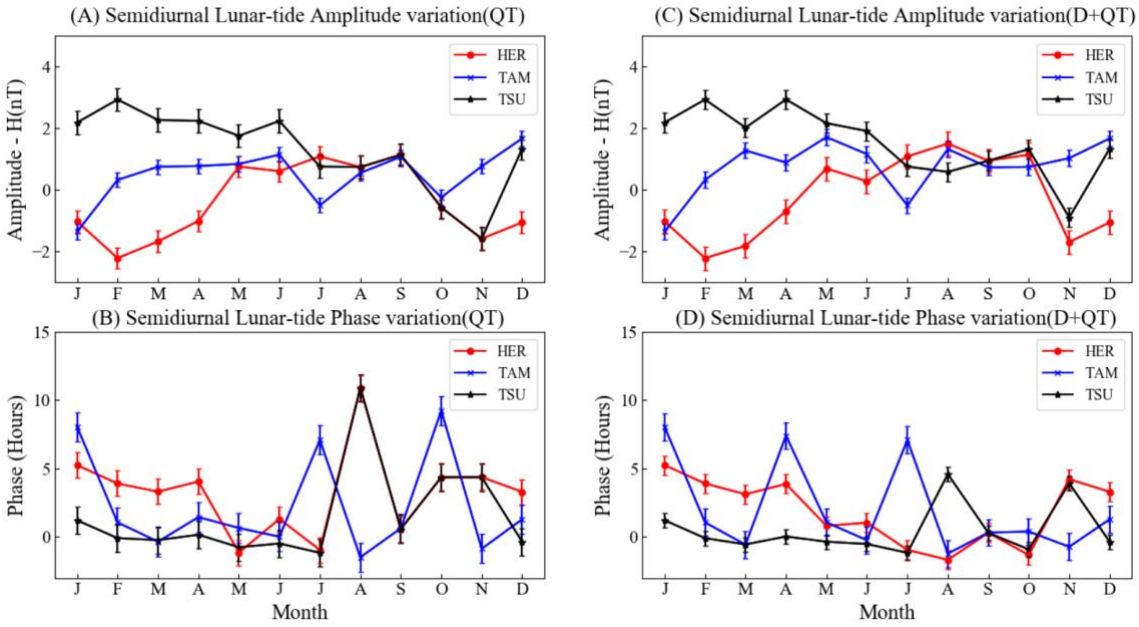

Source: Author

Figure 45A shows the semidiurnal lunar-tide amplitude variation for the quiet time (QT) period in the magnetic field for TSU (solid black line), TAM (solid blue line), and HER (solid red line) in the African sector. The amplitudes for the QT present variabilities throughout the year with TSU attaining the maximum amplitude of around 2.9 nT in February. In HER also, lunar tidal variations have been observed as did Currie (1975), with the maximum obtained amplitude variation around 1.2 nT in March 2018 with TAM attaining a maximum of 1.6 nT in December. The minimum amplitude recorded during the QT for all the stations was around -2.2 nT at HER in February 2018.

Figure 45C presents the semidiurnal lunar-tidal amplitude variation for both the geomagnetically disturbed and quiet time (D+QT) for the three stations in the African sector. During the D+QT, TSU still registered the maximum amplitude of around 1.9 nT, with HER also presenting 1.8 nT, in March and TAM registering a maximum of 1.7 nT in May. A minimum amplitude of 0.3 nT was recorded at HER in June and also for TSU in June 2018.

This was the minimum recorded amplitude at D+QT for all the stations in the year under study. The sudden increase in the amplitude variation during the D+QT, can be attributed to contributions from disturbances in the geomagnetic field (such as from geomagnetic storms etc.). This behavior is seen in all the stations during the D+QT. From Figure 45A and Figure 45C, it is seen that there are little differences in amplitudes between the QT and the D+QT periods since the amplitudes oscillated around the same values. The phases of both the QT and the D+QT periods are shown in Figure 45B and Figure 45D respectively with the maximum and minimum oscillating between 0 lunar hours and 12.5 lunar hours. The highest phase occurred at HER at 12.7 hours and the lowest phase occurred at TAM at 0.25 hours during the QT. Figure 45 gives a comparison between the Brazilian and African sectors.

5.1.2.3 Comparison between the Brazilian and African Sectors

Figure 46 - (A) Semidiurnal lunar-tide amplitudes variation for quiet time (QT), (B) Semidiurnal lunar-tide phase variation for quiet time (QT), (C) Semidiurnal lunar-tide amplitude variation for disturbed + quiet time (D+QT), and (D) Semidiurnal lunar-tide phase variation for disturbed + quiet time (D+QT) for six stations; TSU (solid black line), TAM (solid blue line), and HER (solid red line) in the African sector and SLZ (dashed Maroon line), EUS (dashed yellow line), and SJC (dashed green line) in the Brazilian sector in 2018.

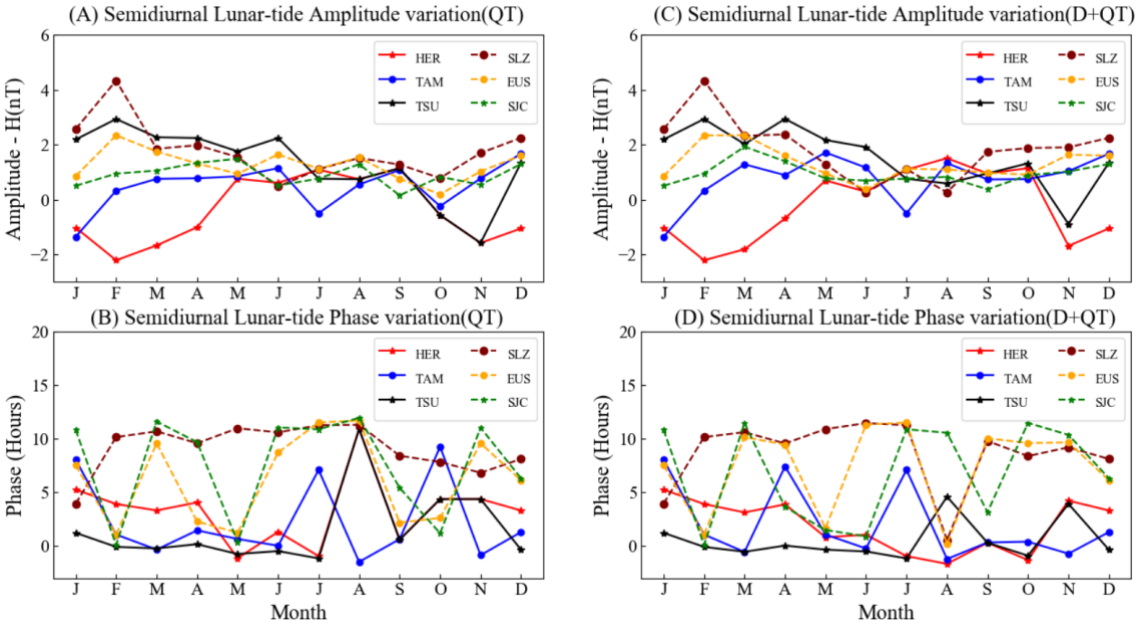

Source: Author.

Figure 46A shows the semidiurnal lunar-tide amplitude variation for the quiet time (QT) period in the magnetic field for TSU (solid black line), TAM (solid blue line), and HER (solid red line) in the African sector, and SLZ (dashed Maroon line), EUS (dashed yellow line) and

SJC (dashed green line) in the Brazilian sector in 2018. The amplitudes for the QT present variations throughout the year with SLZ in the Brazilian sector attaining the maximum amplitude. Hence, the African sector presented lower amplitude variations during this period. In Figure 46C, the results for the disturbed + quiet time (D+QT) are presented. The highest amplitude values recorded for this period were in the Brazilian sector at SLZ in February with EUS also recording the next maximum amplitude in March. The African stations, alternately recorded minimum amplitude values throughout the year. Figures 46B and 46D present the phases for the semidiurnal component for the QT and the D+QT.

TAM in the Northern hemisphere, recorded the highest amplitude during summer. In the Southern hemisphere also, the highest amplitudes were recorded also recorded during summer, which have been observed by others (BARTELS; JOHNSTON, 1940b; SCHLAPP, 1978). The semidiurnal lunar tidal amplitudes in the Brazilian sector generally, presented higher amplitude variation during QT, which has also been reported by (YIZENGAW; CARTER, 2017) in the EEJ who saw lower amplitudes at the African stations studied. They attributed it to the fact that generally, the further a station's location is from the geomagnetic latitude, the weaker the lunar tidal strength. It has been established that the magnetic effect of the semidiurnal tide is most evident near the magnetic equator, where horizontal magnetic perturbations are enhanced due to the equatorial electrojet (BARTELS; JOHNSTON, 1940a; ONWUMECHILLI; ALEXANDER, 1959; RAO; SIVARAMAN, 1958). In this study, TSU (African station), located away from the geomagnetic equator presented higher amplitudes, however, TAM (African station), which was closer to the geomagnetic equator, presented lower amplitude variations. The Brazilian sector, however, presented clear latitudinal differences whereby at the stations closest to the geomagnetic equator, higher amplitude variations were observed. These differences could be due to the contributions from the disturbed EEJ.

A seasonal variation in the semidiurnal lunar tide can be seen in both sectors and this behavior has been predicted in classical theory and has been observed in surface pressure, ionospheric F-layer, geomagnetic observation, and lower atmospheric winds (GELLER; SCHOEBERL, 1973; JONES; JONES, 1950; TARPLEY, 1971). Using simulations, Vial and Forbes (1994) showed the existence of seasonal behavior for the lunar semidiurnal tide in the MLT region and predicted a latitudinal variation along the year. Although it is expected that the amplitudes during the summer months should be higher than the amplitudes during the winter months (ONWUMECHILLI; ALEXANDER, 1959), an interesting trend is seen at HER,

where the highest amplitudes were recorded in June, July, and August, which happen to be winter months. The summer months presented lower amplitude variations, however.

A semiannual variation can further be seen in the semidiurnal lunar tide at most of the stations studied, however, HER presented a distinct annual variation where the peak was around the winter months. The annual variation can be attributed to that of lunar tidal forcing at E-region heights (e.g., PEDATELLA, 2014; YAMAZAKI, 2022). The semiannual and annual characteristics have also been observed (PAULINO et al., 2015; SANDFORD et al., 2007; STENING; VINCENT, 1989) in wind. Paulino et al. (2021) mentioned in their paper that triannual variations have also been observed and simulated in some atmospheric fields as well (e.g., PEDATELLA, 2014; PEDATELLA; LIU; RICHMOND, 2012).

Studies have also shown that the semidiurnal lunar tide can be amplified during SSW (e.g., PEDATELLA; LIU; RICHMOND, 2012; STENING et al., 1997; ZHANG; FORBES, 2014), which leads to an enhancement of L currents at mid and low latitudes (e.g., FEJER et al., 2010; YAMAZAKI, 2014). This study covers major SSW in February 2018 (RAO et al., 2018) and therefore could account for the high amplitudes observed in February at some stations.

It can generally be seen from this study that, the DT+QT results presented higher amplitude variations in both sectors compared with the QT results. The difference in the amplitude variations could be due to the disturbance in the geomagnetic field since Raja Rao and Jeevananda Reddy (1973) concluded in their study that magnetic activities affect both solar and lunar tidal amplitudes. It has also been observed that during disturbances the ring current closes over the ionosphere on the night side (AKASOFU; CHAPMAN, 1964). Raja Rao and Jeevananda Reddy (1973) further showed from the disturbance variations at Huancayo and Koror that the DR current partly flows in the ionosphere and Cahill JR (1966) observed and confirmed the asymmetric inflation of the magnetosphere with the satellite Explorer 26.

The subsequent section presents the results and discussion for the planetary analysis.

5.2 Planetary Waves

This section gives the results and discussion obtained for planetary waves using data from the magnetometer and the ionosonde. We first present the result of the F10.7 flux, which gives us the solar activity during the period of the study. Figure 47 Below presents the day-to-day variation, the wavelet power spectrum analysis and the Lomb-Scargle results for the F10.7 flux.

Figure 47 - (A) Day-to-Day variation (B) Wavelet power spectrum, and (C) Lomb-Scargle results for the F10.7 flux in 2018. This gives the solar activity for 2018.

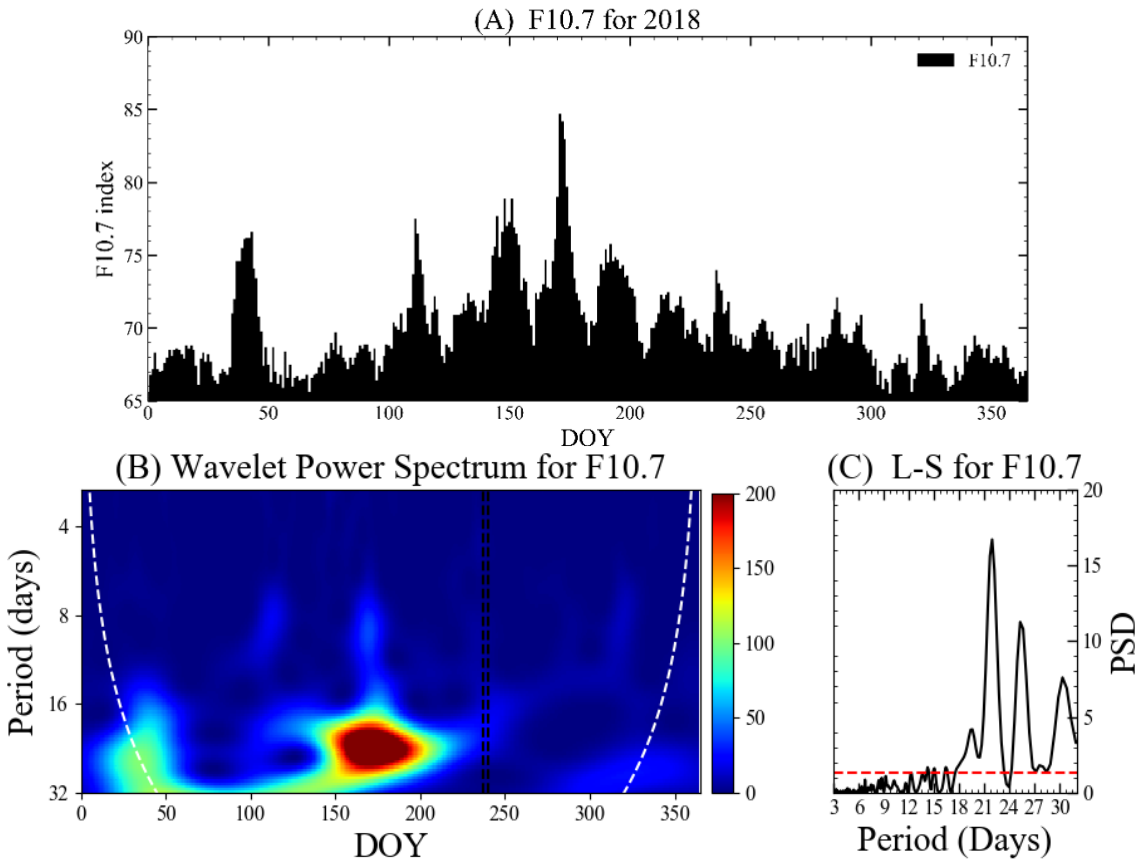

Source: Author

The F10.7 flux results in Figures 47A, 47B, and 47C show strong oscillations in the time series, the wavelet power spectrum, and the Lomb-Scargle Periodogram respectively. 47A shows the solar activity for 2018 with day 171 presenting the highest activity. The period of 16-32 days was the most important presented. In Figure 47B, there is a strong oscillation period at around 21-25 days. It occurred between days 150 to 200. In the Lomb-Scargle Periodogram in Figure 47C, strong periods of oscillation can also be seen between 21-24 days, 24-27 days, and around 29-32 days. These periods are similar to the periods of oscillation presented by the wavelet power spectrum.

In Section 5.2.1, the daytime (12:00 to 15:00 LT) and evening (PRE- 18:00 to 22:00 LT) results from the magnetometer are presented. This is followed by the results from the ionosonde analysis in chapter 4.

5.2.1 Magnetometer

Figure 48 - (A) averaged daily ΔH variation at stations in the Brazilian sector for daytime hours of 12:00 (black), 13:00 (green), 14:00 (blue), and 15:00 (red) LT during 2018 and (B) Same as A but for the African sector in 2018.

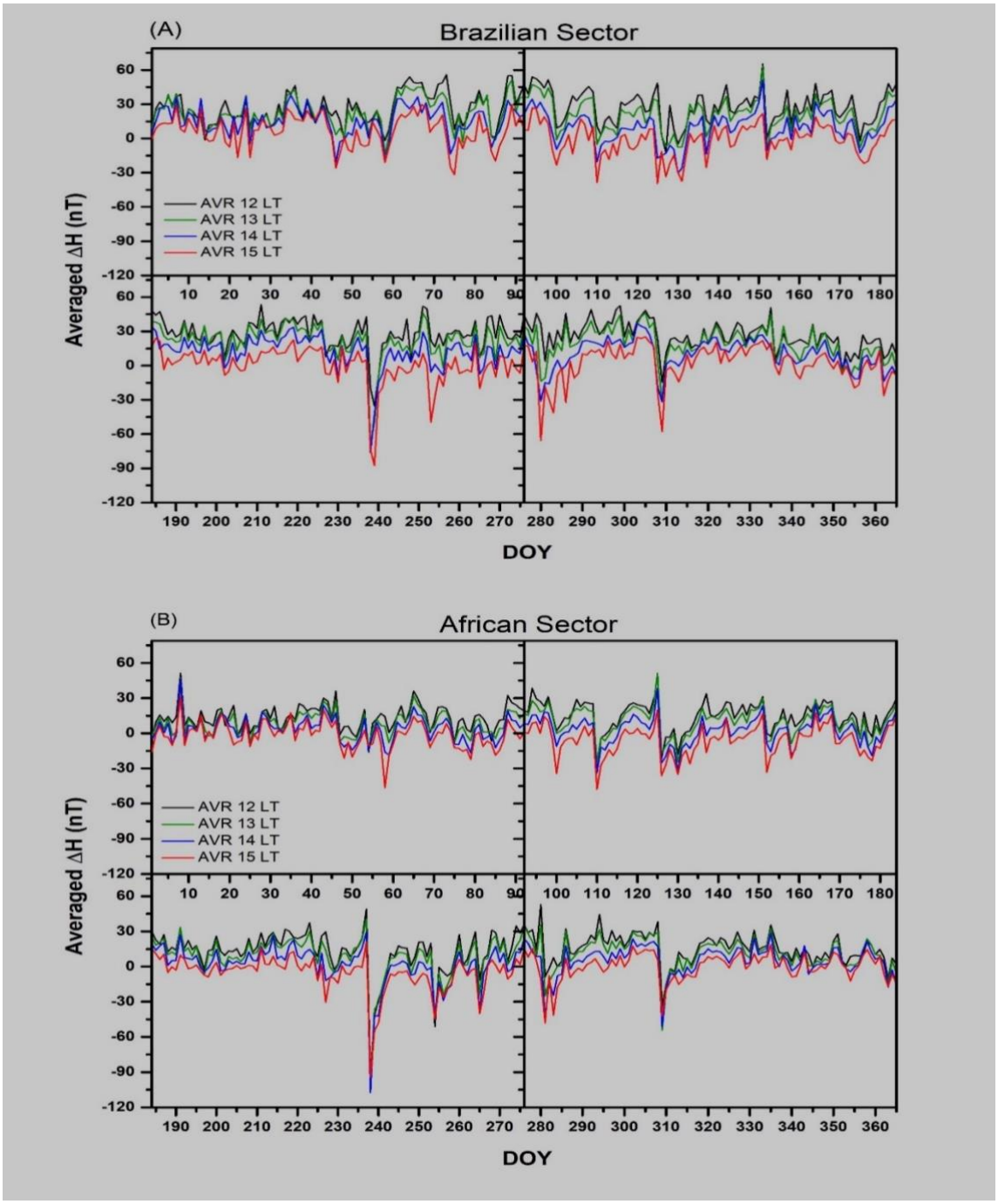

Source: Author

Figure 48A shows the day-to-day variability for the averaged ΔH (ΔH henceforth) component of the magnetic field in the Brazilian sector at the daytime hours of 12:00 (black), 13:00 (green), 14:00 (blue), and 15:00 (red) LT during 2018. The averaging was possible

because from Figure 48 the variability of ΔH for all the stations under study were in phase. Generally, the Brazilian sector showed that the ΔH oscillations tend to be in phase for all the selected daytime hours for 2018. The least intense ΔH(65nT) was at 12:00LT in May whereas the most intense ΔH (-90nT) for this sector was at 15:00LT in August. Figure 48B also shows a day-to-day variability for the averaged ΔH component of the magnetic field in the African sector 12:00, 13:00, 14:00, and 15:00 LT. The results show that all the selected hours for this sector were also in phase throughout 2018. The maximum averaged ΔH amplitude (51nT) was recorded at 13:00LT in May whereas the most intense ΔH (-107nT) variation for this sector was recorded at 14:00LT in August. In both the Brazilian and African sectors, the intensities of ΔH at 12:00LT were consistently less than during the other selected hours. A geomagnetic storm occurred on 25th August, 2018 which corresponded to day 238. This storm attained a Dst of -175nT (occurred at 06:00UT and 07:00UT which is at 03:00LT and 04:00LT in the Brazilian sector and 07:00/08:00LT at TAM and 08:00LT/09:00LT at TSU and HER in the African sector) which Gonzalez et al. (1994) classifies as an intense geomagnetic storm. This occurrence can clearly be seen in the result presented in Figure 48. Apart from the major storm which occurred during this period in both sectors, other significant disturbances and storms (such as on DOY 309 and 280) were also recorded within the course of the year.

The wavelet spectrum of the ΔH intensities for periods at 12:00LT, 13:00LT, 14:00LT, and 15:00LT for the Brazilian and African sectors in 2018 are presented in Figure 49 (A) and (B).

Figure 49 - (A) wavelet spectrum showing the daytime ΔH intensities for periods at 12:00LT, 13:00LT, 14:00LT, and 15:00LT for the Brazilian sector in 2018 and (B) same as A but for the African sector in 2018. The black dashed lines running vertical show the storm period of 2018.The white–dashed curved line depicts the cone of influence (coi).

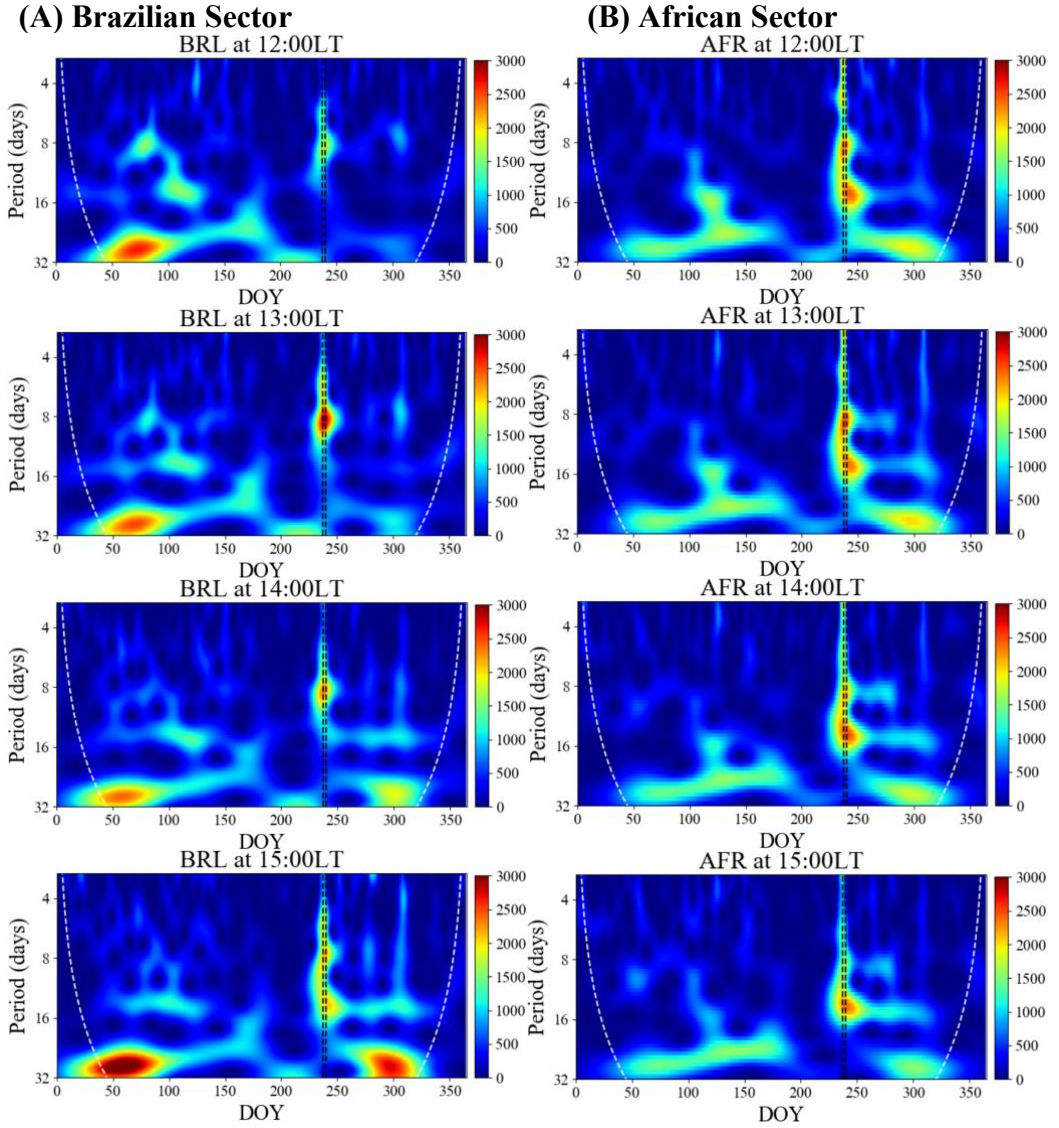

Source: Author

The wavelet analysis in Figure 49 shows different periods present during the selected daytime hours. In Figure 48A, the periods for 12:00LT to 15:00LT in the Brazilian sector is presented. Generally, periods between 3 to 32 days were observed in this sector. The dark red regions show the most intense and significant periods and were seen within all the selected daytime hours although their distribution over the year differed. 25-32 day periods were seen to occur intensely in the Brazilian sector. Figure 49B presents the results of the wavelet analysis for the African sector. Periods between 5-25 days are seen to occur most and at around 262 days in this sector which was around the geomagnetic storm of 2018. Most studies tend to

remove the time of the geomagnetic storm occurrence from the dataset before analysis, however, in this study we considered the storm-time together with the quiet days. Other researchers (e.g., FAGUNDES et al., 2005 and references therein) have also observed these dominant periods. In the African sector however, periods of 5-24 days prevail from day 243 to 267 whereas in the Brazilian sector, periods of 5-16 days prevail from day 243 to 250 and 24-32 days prevail in the 1st, 3rd, and 4th quarters of 2018. Also, considering Figures 49A and 49B in both sectors, we can see that during the most intense ΔH variation which as pointed out to be due to the occurrence of a geomagnetic storm, the wavelet analysis in both sectors presented interesting period ranges for the different hours. An interesting feature was the fact that periods presented here during the daytime were prevailing as can be seen in the period ranges presented by both sectors next. In the Brazilian sector, periods of ~7-12 days at 12:00LT, ~5-15 days at 13:00LT, ~6-14 days at 14:00LT, and ~5-16 days at 15:00LT are presented, respectively. Also, in the African sector during the occurrence of this storm, periods of ~4-20 days at 12:00LT, ~4-18 days at 13:00LT, ~5-16 days at 14:00LT, and ~8-15 days at 15:00LT. However, the Brazilian sector, shows an increasing range interval trend (~5-12 to ~5-16) whereas in the African sector a decreasing range interval trend (~4-20 to ~8-15) in the periods observed as the days progressed. These periods also prevailed for some days after the storm occurred. We interestingly noted that, during the quiet time in the year, these period ranges were usually not present. The periods obtained from the Lomb Scargle for the sectors and their respective times presented in Figure 49 are shown in Figure 50.

Figure 50 - (A) Lomb-Scargle analysis showing the ΔH periodicities (3 to 32 days) for 12:00(black), 13:00(red), 14:00(blue), and 15:00(purple) LT for the Brazilian and African sectors in 2018 (B) Same as A but in the 3 to 24 days.

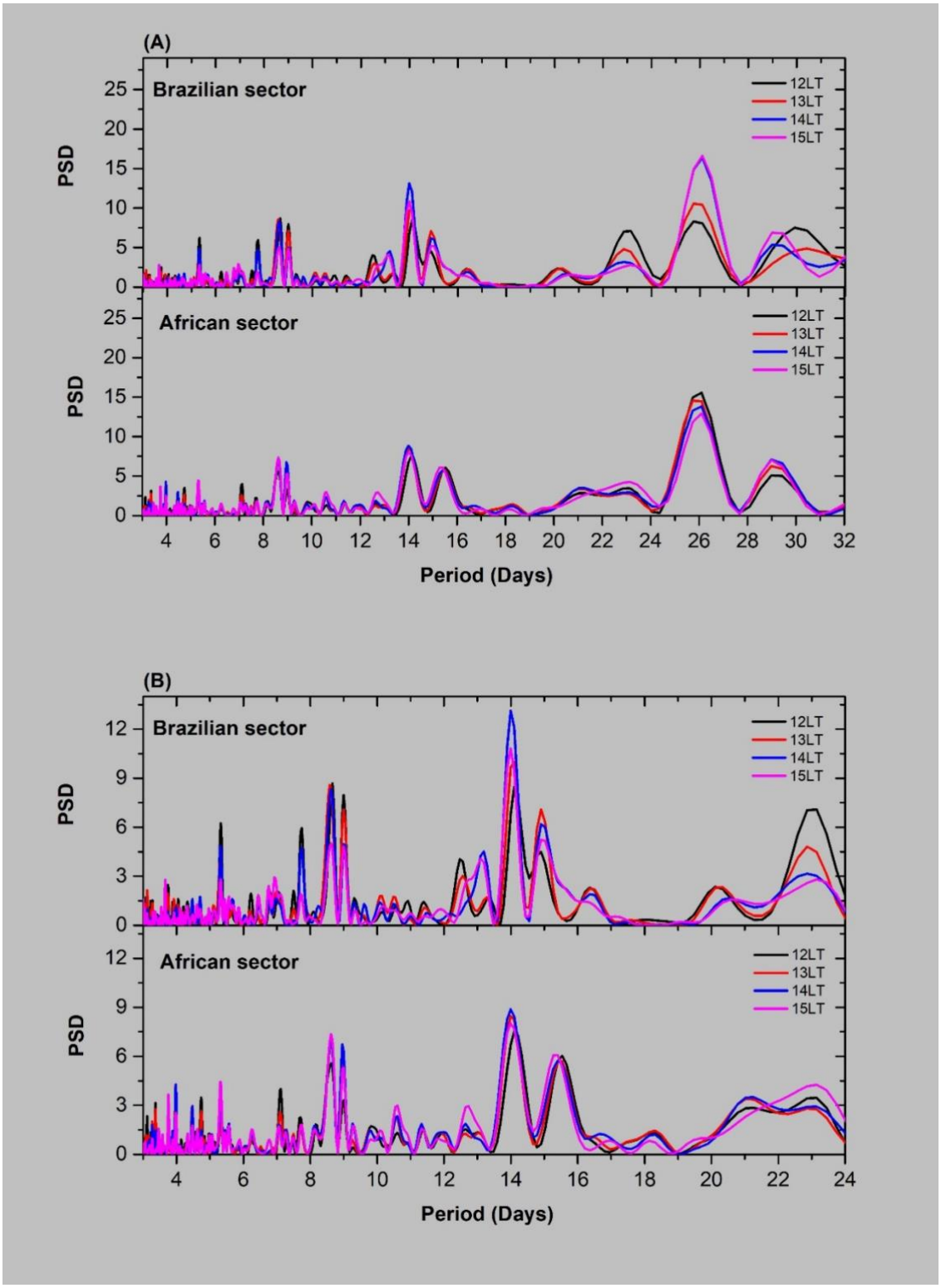

Source: Author

In Figures 50A and 50B, we present the Lomb-Scargle analysis results for the Brazilian and African sectors at 12:00 LT, 13:00 LT, 14:00 LT, and 15:00 LT, respectively. It is seen that the PSD is scaled from 0 to 24 whereas the period (Days) is scaled from 5 to 32 in the aforementioned Figures. This was done to give the full graphical representation of the analyzed dataset taking into consideration all the periods analyzed. The most prominent period range is seen between 24-32 days. These long-term periods of around 24-28 days have been attributed to solar rotation (FAGUNDES et al., 2005). In addition, since a synodic month is 29.5 days, the periods around 29-30 days in Figure 50A and 50B could possibly be due to the moon's rotation. Since our focus here is on the PW periods present in the magnetic field without the effects of the solar and lunar rotations, we zoom-in 50A and 50B by considering periods from 5 to 24 days. We do this by scaling the PSD from 0 to 12 and the period (Days) from 5 to 24. After this scaling is done, the peak periods without the effects of the solar and lunar rotations become more prominent. Figure 50C and 50D presents these results. In both sectors, dominant periods of 5-6, 7-10, 14-16, and 20-24 days are present and in agreement generally. These dominant periods are selected taking into account their significant levels. In the Brazilian sector, within the 5-6-day period, a peak of about 5.3 days is recorded at 12:00 LT whereas in the African sector, there was no significant peak within this range. The recorded 7-10 days period presented peaks of around 7.7 days at 12:00LT in the Brazilian sector and 8.5 days at 12:00LT and 15:00LT in the Brazilian and African sectors respectively. Another peak period recorded around 9 days (this occurred at 12:00LT and 15:00LT in the Brazilian and African sectors respectively) was within the 7-10 days period range. Dominant periods of 12-16 days were also recorded with a peak period of around 14 days occurring in both sectors at 14:00LT. Fagundes et al. (2005) have also attributed the short-term period of around 13.5 to 14 days to the half-solar rotation. However, since the solar rotation period range of about 24-28 days has already been recorded, it is not surprising that the half-solar rotation peak is present. Another peak of interest around 15 days also occurred at 13:00LT in the Brazilian sector whereas a peak of around 15.5 days occurred at 15:00 LT in the African sector. These peaks could possibly be the quasi 16-day wave (Q16DW) or 16-day wave studied by various researchers (e.g., FAGUNDES et al., 2005; FORBES; LEVERONI, 1992; VINEETH et al., 2007). The 20-24 days period range presented a peak around 23 days at 12:00LT in the Brazilian sector whereas, in the African sector the presented periods within this range were not significant. Figure 51 shows the day-to-day variation for selected evening hours in the Brazilian and African sectors.

Figure 51 - (A) averaged daily ΔH variation at stations in the Brazilian sector for the evening (PRE) hours of 18:00 (black line), 19:00 (green line), 20:00 (blue line), 21:00 (yellow line), and 22:00 (red line) LT respectively during 2018 and (B) same as A but for the African sector in 2018.

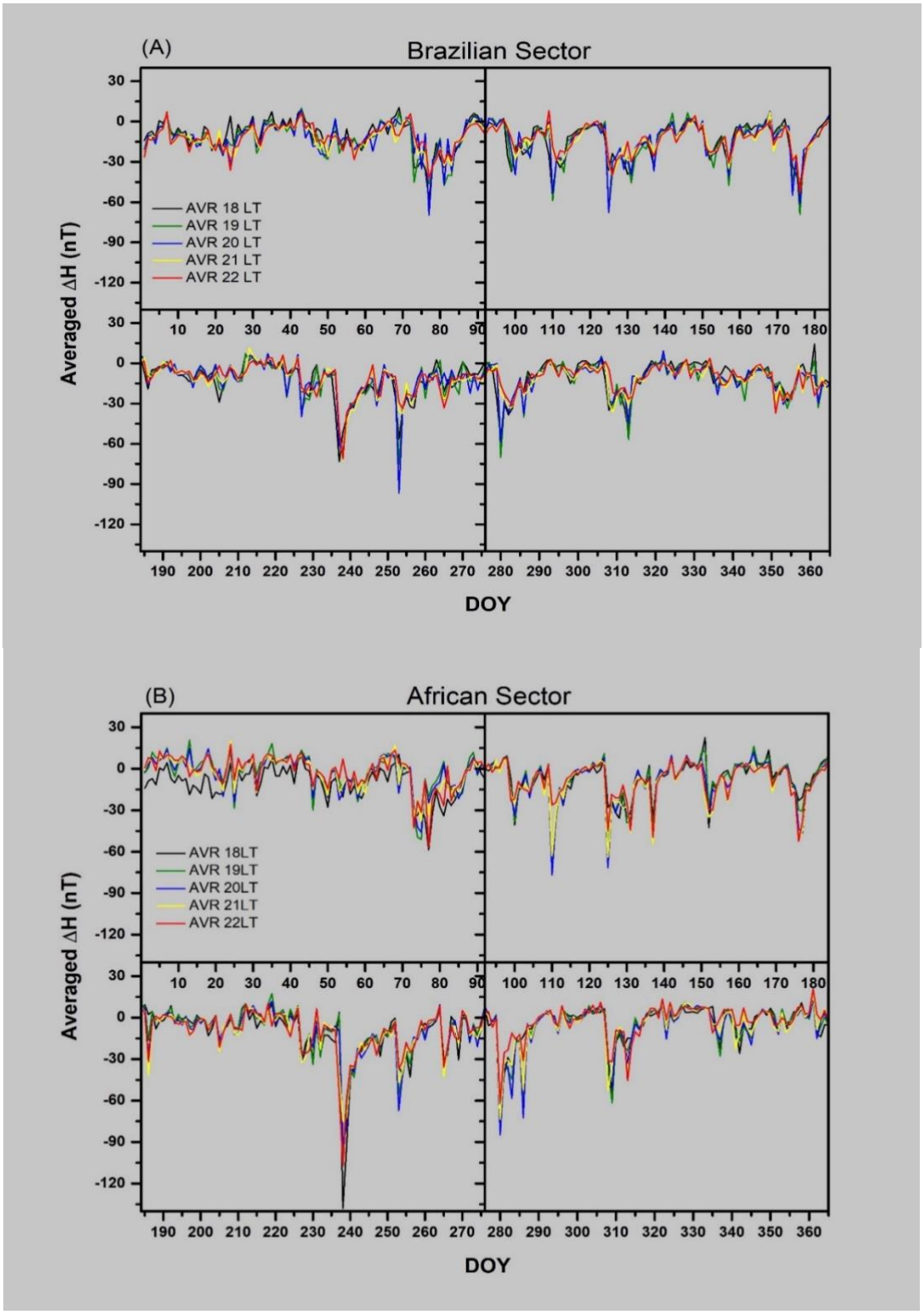

Source: Author

Figure 51 presents the day-to-day variability averaged ΔH component of the magnetic field in the Brazilian and African sectors at the evening (PRE) hours of 18:00 (black line), 19:00 (green line), 20:00 (blue line), 21:00 (yellow line), and 22:00 (red line) LT respectively during 2018. The ΔH variations in both sectors generally show similar wavelike oscillations with some disturbances. These disturbances indicate storms, which occurred during 2018 as this study, considered both quiet and disturbed time variations. The results from the Brazilian sector show similar variations throughout the year. The ΔH variations for all the selected PRE hours at all the stations are seen to be in phase. The least intense ΔH occurred at 22:00LT in April whereas the most intense ΔH (-96nT) for this sector occurred at 20:00LT in September. Figure 51B also shows the day-to-day variability for the averaged ΔH component of the magnetic field in the African sector at the evening hours of the same time interval as Figure 51A. The results show that all the selected hours for this sector are also in phase throughout the entire year. The least intense ΔH was recorded at 18:00LT in May whilst the most intense ΔH for this sector was recorded at 21:00LT in August (during a severe storm, which has been expanded on under the daytime results). Also, comparing the ΔH variations in both sectors, we can see that the least intense and most intense ΔH presented by the African sector happen to be the least intense and most intense ΔH for both sectors. Figure 51 shows the wavelet power spectrum for selected evening hours for the Brazilian and African sectors.

Figure 52 - (A) Wavelet spectrum showing the ΔH intensities for periods at 18:00LT, 19:00LT, 20:00LT, 21:00LT, and 22:00LT for the Brazilian sector in 2018 and (B) same as A but for the African sector in 2018.

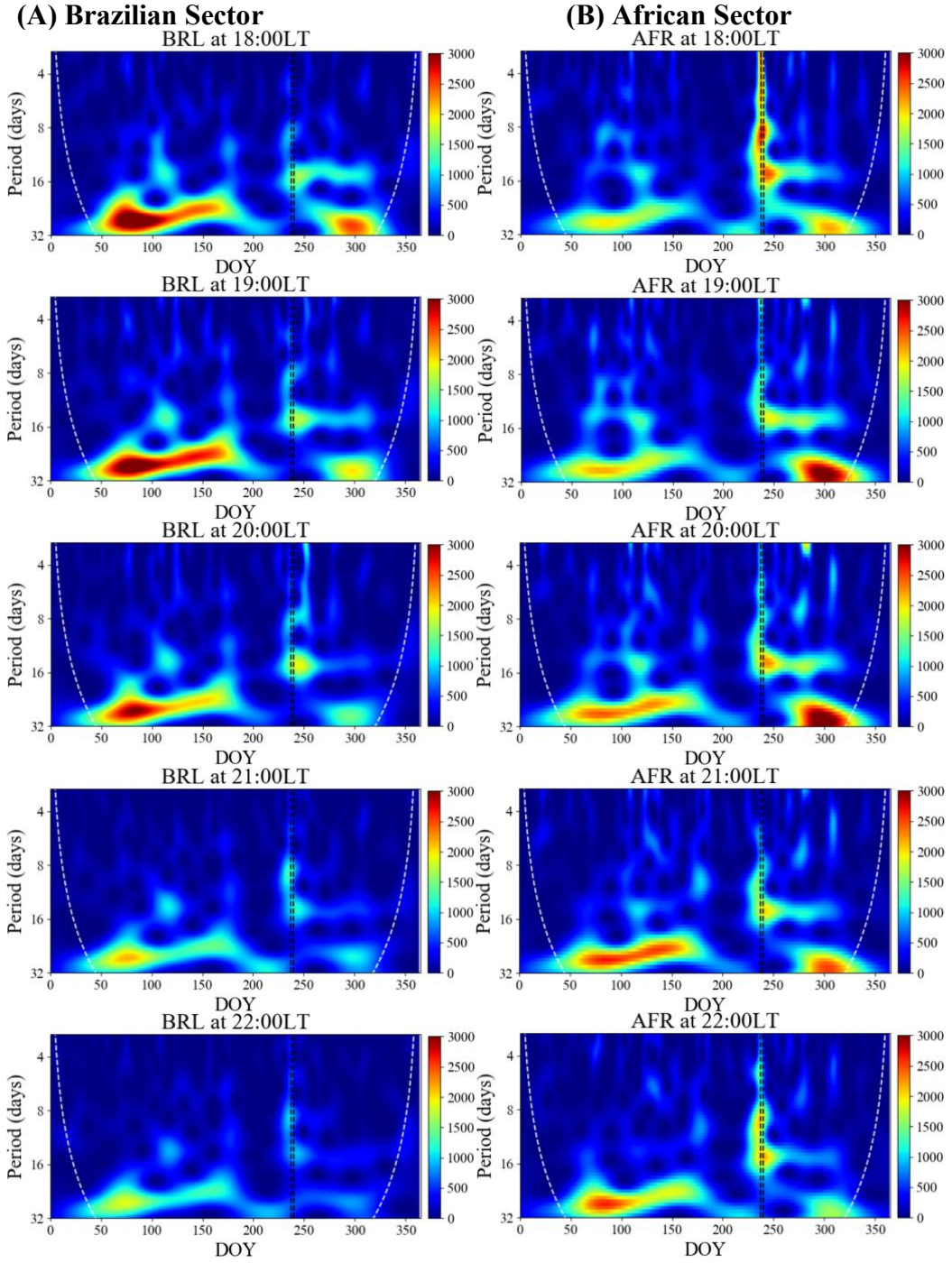

Source: Author

The results of the wavelet analysis in Figure 52 show different periods present during PRE. Figure 52A presents the periods from 18:00LT to 22:00LT in the Brazilian sector. Generally, the occurrence of periods between 5 to 32 days were significant in this sector. The most intense period of around 24 to 32 days occurred at 18:00LT and around days 267 to 342

which is during the winter to spring in this sector. As pointed out earlier, these long-term periods have been attributed to solar rotation (FAGUNDES et al., 2005). Figure 52B shows the results of the wavelet analysis for the African sector. Periods presented during this period are more intense compared to the intensity/strength of periods presented by the Brazilian sector. Very intense periods ranging from 6 to 32 days can be seen from around day 219 to around day 316. In the African sector, the occurrence of some periods presented were more intense. During the geomagnetic storm which is clearly depicted by the sudden downward drop around DOY 237 in Figure 52B, the Brazilian sector presented ~15-16 days at 18:00LT, ∽15 days at 19:00LT, ~15-16 days at 20:00LT, and at 21:00 and 22:00LT, no intense (very dark red regions) period ranges were presented. In the African sector also, ∽4-32 days at 18:00LT, ∽8 days at 19:00LT, ∽8-16 days at 20:00LT, ∽10-16 days at 21:00 LT, and ∽5-26 days at 22:00LT. It can be seen that the African sector presented the longest period range interval during this occurrence. The subsequent Figure, presents the Lomb-Scargle periodogram results for the Brazilian and African sectors during the selected evening hours.

Figure 53 - (A) Lomb-Scargle analysis showing the ΔH periodicities (3 to 32 days) for 18:00 (black), 19:00(red), 20:00(blue), 21:00(purple), and 22:00(green) LT for the Brazilian and African sectors in 2018 (B) Same as A but for 3 to 24 days.

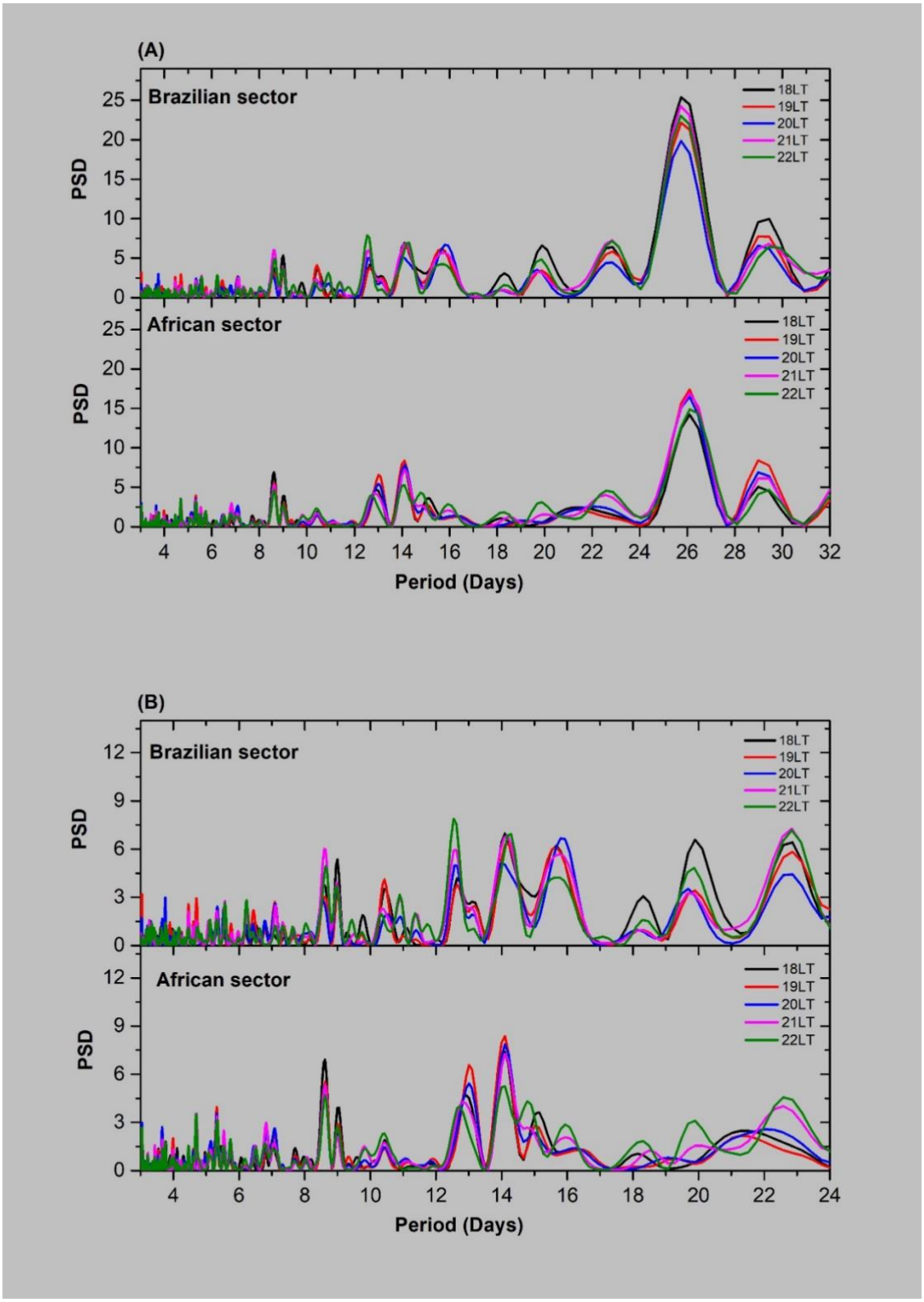

Source: Author

Figures 53A and 53B present the Lomb-Scargle analysis results for the Brazilian and African sectors at 18:00, 19:00, 20:00, 21:00, and 22:00 LT respectively. As elaborated in the results of Figure 53, the same form of scaling was used here and was done for the same reason explained under the Figure 53 result. Here, the most prominent period seen is between 24-32 days (refer to results of Figure 9 for explanation). As mentioned, our main interest is in the PW periods present in the magnetic field, hence, we zoom-in 53A by considering periods from 5 to 24 days as we did for Figure 50B. Figure 53B therefore presents the results. The dominant periods presented after we zoomed-in and considered periods with peaks selected based on the significant levels are 8-10 days, 12-16 days, and 20-24 days. It is worth noting that during the PRE hours in both sectors, the period range of 5-6 days (which was considerably significant during the daytime hours) was not significant hence, we did not consider it. The 8-10 day period range presented peaks of around 8.5 days at 21:00LT in the Brazilian sector and at 18:00LT in the African sector. It also presented another peak at around 9 days at 18:00LT in the Brazilian sector. The 12-16 day period range presented peaks of around 12.5 days at 22:00LT in the Brazilian sector, 13 days at 19:00LT in the African sector, 16 days at 20:00LT in the Brazilian sector, and 14.5 days at 22:00LT and 19:00LT in the Brazilian and African sectors, respectively. Bertoni et al. (2011) reported similar planetary wave-type range of 12-16 days when they studied the occurrence of ionospheric Equatorial Spread-F (ESF) and morphologic features modulated by planetary waves. In addition, the 20-24 day period presented peaks of around 20 days at 18:00LT and another peak at around 23 days at 21:00LT and 22:00LT all in the Brazilian sector. Similar periods were observed in the result of the wavelet analysis and Lomb-Scargle.

Section 5.2.2 presents the results obtained from the ionosonde analysis.

5.2.3 Ionosonde

Results from the ionosonde are shown in the subsequent Figures. We present first the daytime results and then the evening time results. It also gives the results in the order of the time series, the wavelet power spectrum, and then the Lomb-Scargle Periodogram.

Figure 54 - (A) Virtual height showing the daily variation for the daytime hours of 14:00 (black) and 15:00 (red) LT at ARA and (B) Same as A but for SJC in 2018.

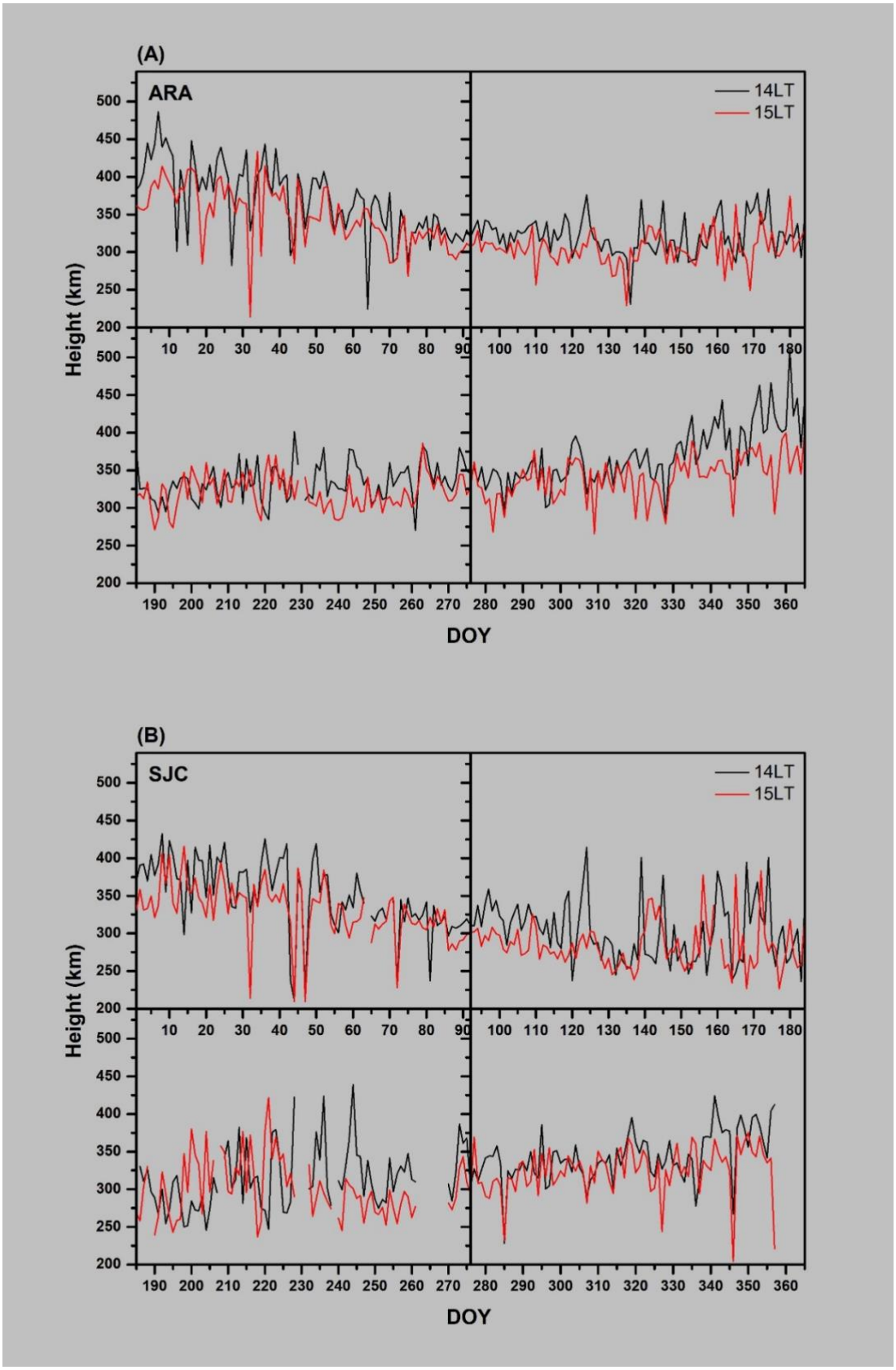

Source: Author

The day-to-day variation of the virtual height of the ionosphere for two daytime hours (14:00 LT and 15:00 LT) are shown in Figure 54. Two stations from the Brazilian sector are presented. Both Figures 54A and 54B show wave activities with ARA recording the highest virtual height attained by the ionosphere at around 510km at 14:00LT whereas SJC recorded the lowest height attained at around 205km at 15:00LT. Generally, both selected hours were in phase at both stations.

Figure 55 - The wavelet spectrum showing the virtual height for daytime period at 14:00LT and 15:00LT in (A) ARA and (B) SJC in the Brazilian sector in 2018.

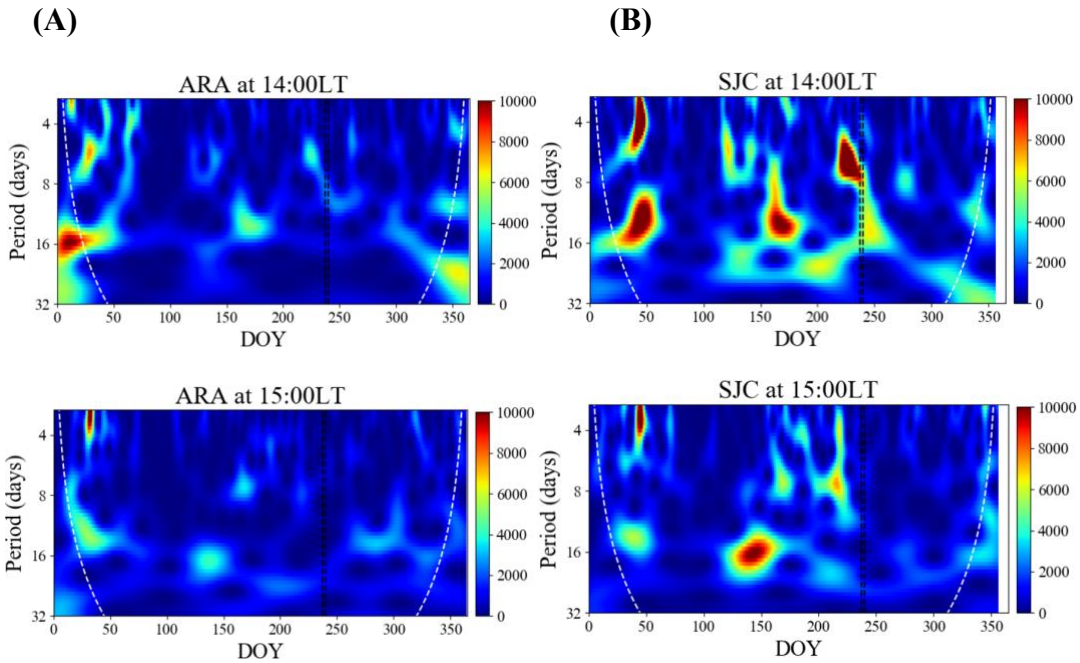

Source: Author

Figure 55 gives the wavelet analysis results for the virtual height for ARA and SJC. It shows the periods for the daytime hours of 14:00LT and 15:00LT. Different periods are seen throughout although there are some, which are more intense. In ARA at 14:00LT, notable periods within the cone of influence are around 5-7 days, 12-18 days, and 10-14 days. For SJC at 14:00LT, the periods from the results are 3-6 days, 7-16days, 7-15 days, and 5-7 days. At 15:00LT at ARA, the most notable periods are around 3-5 days and 7-15 days. SJC at 15:00LT also gives 3-4 days and 14-24 days. There are however other periods present in the spectrum.

Figure 56 - Lomb-Scargle analysis of virtual height periodicities (3 to 32 days) for SJC and ARA at 14:00LT and 15:00LT in 2018.

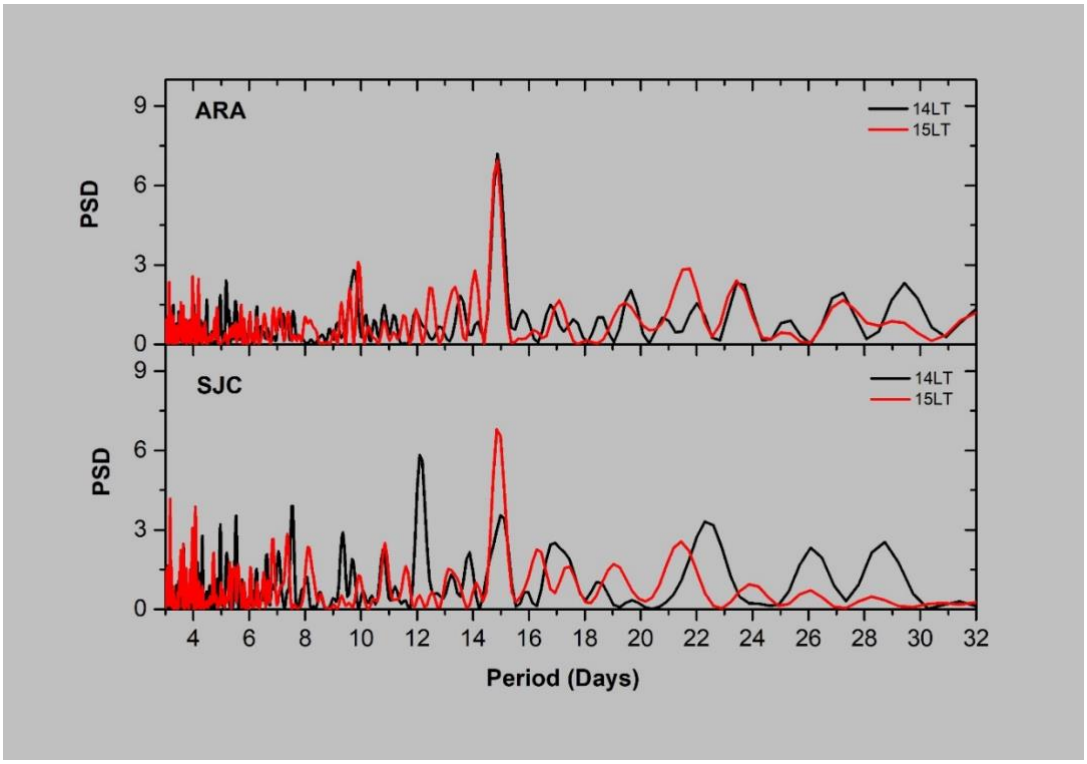

Source: Author

In Figure 56, ARA and SJC both present interesting periods at 14:00LT and 15:00LT. In ARA, both 14:00LT and 15:00LT present strong periods between 14-16 days. In SJC, however, 14:00LT presented a strong period between 12-13 days whereas, 15:00LT presented a strong period between 14-16 days. Other prominent periods were also presented by both stations. Between 14-16 days' periods can be seen at both stations at both selected hours.

Figure 57 - (A) virtual height showing the daily variation for the daytime hours of 18:00 (black) and 19:00 (red) LT at ARA and (B) Same as A but for SJC in 2018.

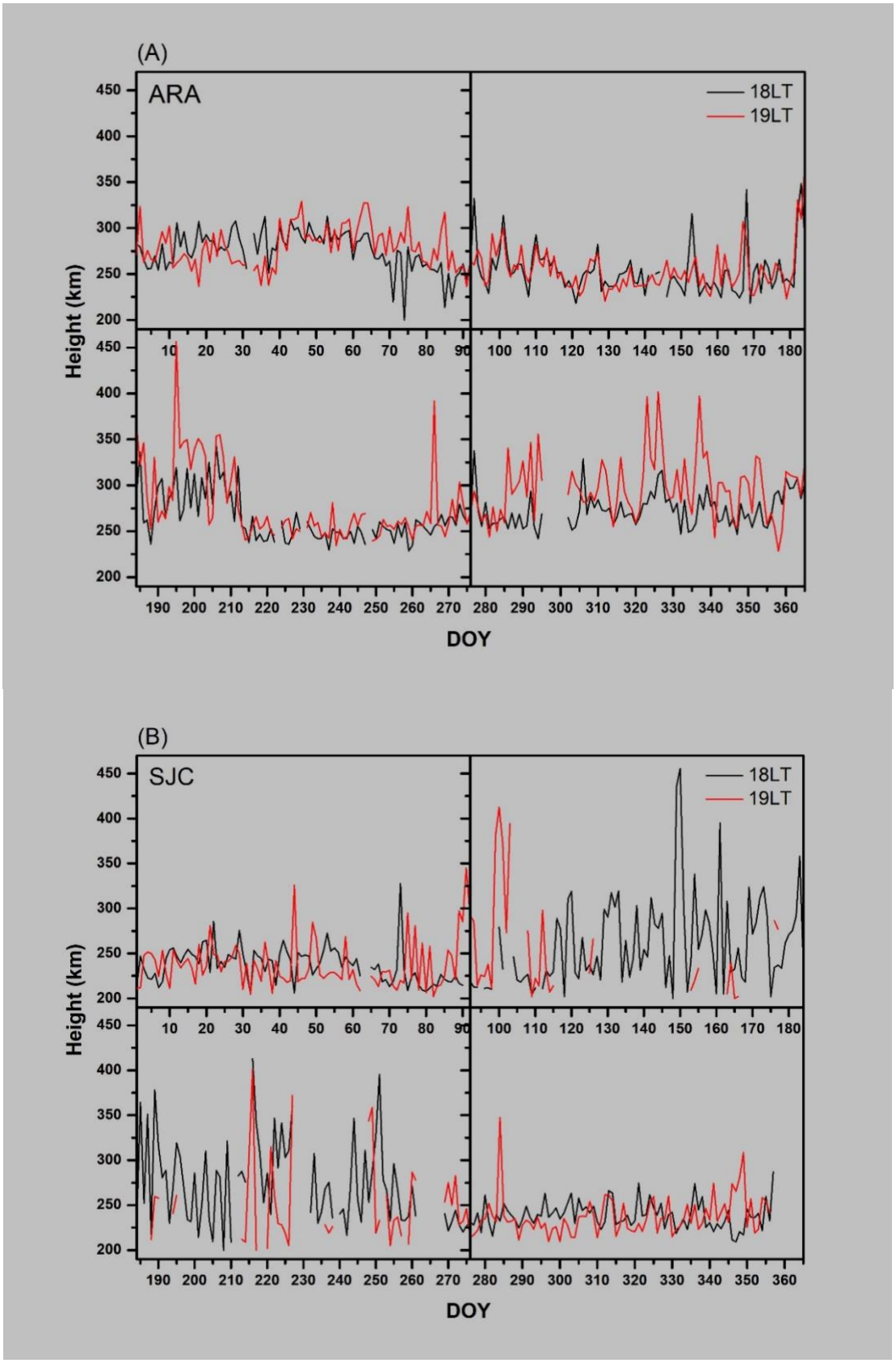

Source: Author

Figure 57 presents a day-to-day variation of the virtual height of the ionosphere for two selected evening hours. ARA and SJC, both in the Brazilian sector are presented. Figure 57A gives the day-to-day variation at 18:00LT and 19:00LT whereas Figure 57B presents the variations at same hours. Variations at both stations show wave activities with ARA and SJC both recording highest virtual height values attained by the ionosphere at around 450km at 19:00LT and 18:00LT respectively whereas SJC recorded the lowest height attained at around 195km at 19:00LT.

Figure 58 - The wavelet spectrum showing the virtual height for evening period at 18:00LT and 19:00 LT in (A) ARA and (B) SJC in the Brazilian sector in 2018.

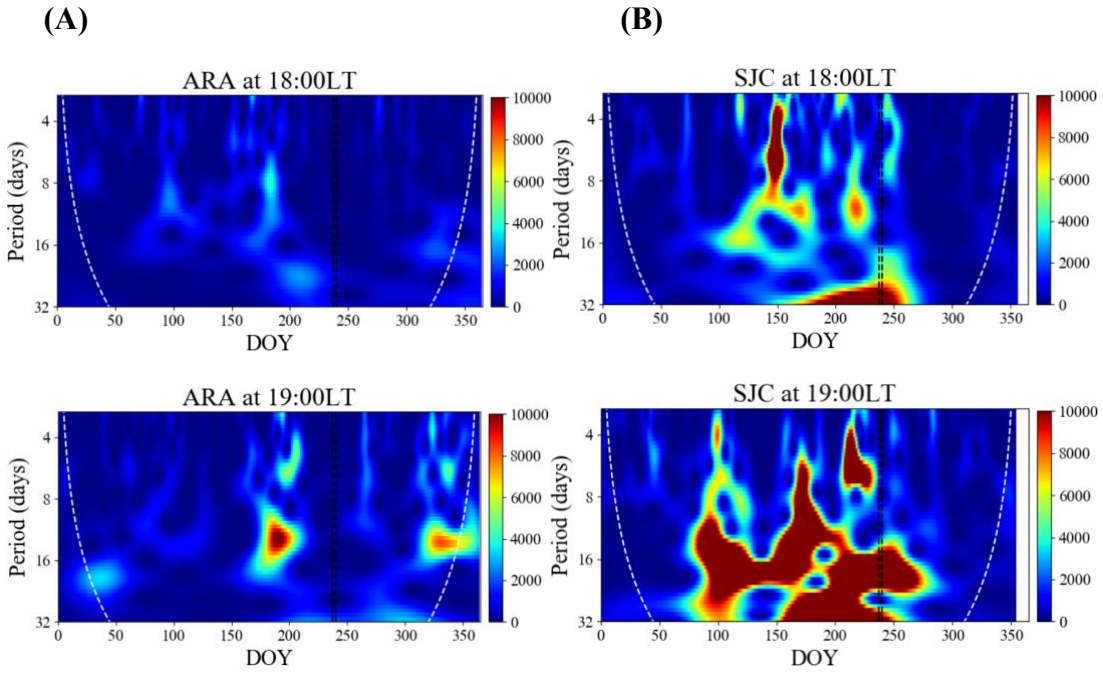

Source: Author

Figure 58 presents the WPS results for the virtual height at ARA and SJC. It shows the periods for two selected evening hours of 18:00LT and 19:00LT. Different periods are seen throughout although there are some, which are more intense. In ARA at 18:00LT, a notable period of about 6-11 days is seen. For SJC at same time, intense periods of around 3-8 days and 26-32 days are presented. Also at 19:00LT at ARA, prominent periods of around 9-17 days and 13-16 days are recorded. At the same time in SJC, prominent periods of around 12-24 days, 8-20days, 4-6 days, and 18-24 days can be seen. The most intense however in this station was around 26-32 days. Other periods are seen scattered throughout the year.

Figure 59 - Lomb-Scargle analysis showing the virtual height periodicities (3 to 32 days) for SJC and ARA at 21:00 LT in 2018 respectively.

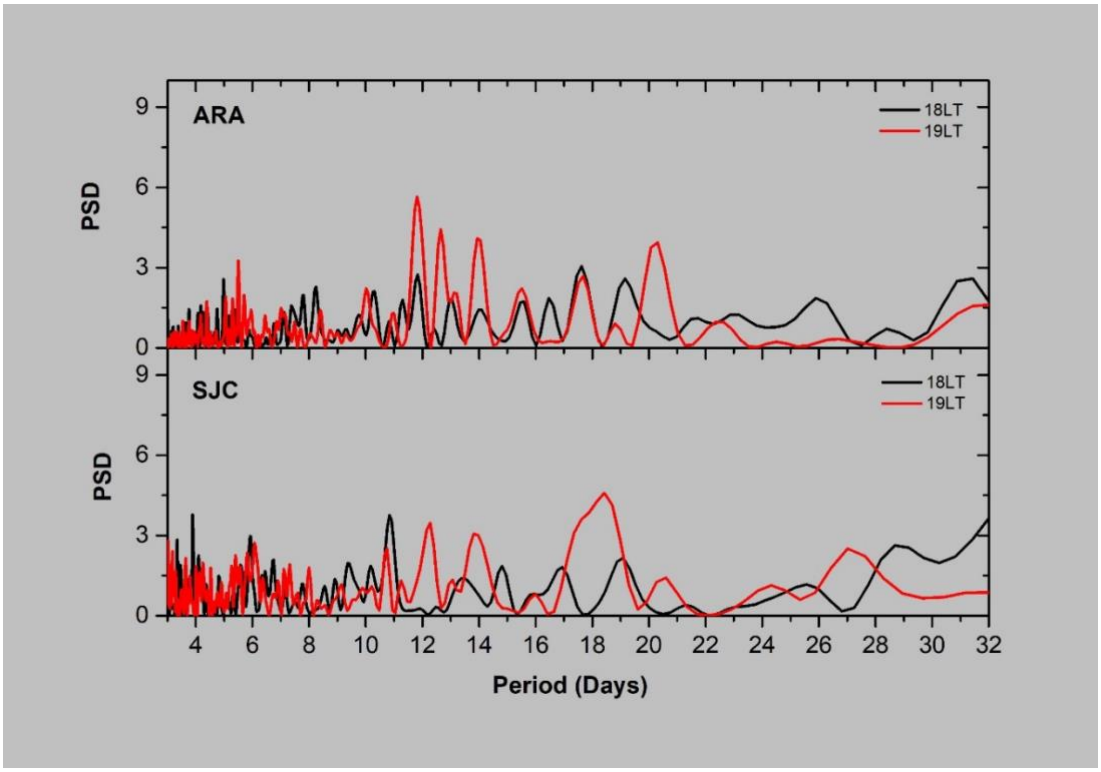

Source: Author

Figure 59 shows ARA and SJC both present interesting periods at 18:00LT and 19:00LT however, at both stations, the periods at 19:00LT were stronger. In ARA, periods of 11-15 days and also 19-21 days all at 19:00LT were recorded. At SJC, periods between 11-15 days and 16-20 days were presented at 19:00LT. At 18:00LT in ARA, periods were presented between 17-19 days and also from around 30-32 days. In SJC, a prominent period was seen between 3-4 days and also between 10-11 days. In SJC also, periods between 27-32 days were seen. At both stations, however, other periods were presented although their peaks were not prominent.

Daily readings taken by the magnetometer of the Earth's geomagnetic field show irregular changes in the geomagnetic field which represent the superposition of spectral components whose amplitudes usually increase with increasing periods (CAMPBELL, 2003). These variations or ripples in the geomagnetic field range from quiet periods to disturbed time depending on the geomagnetic conditions and are also known to originate from different sources such as the ground, ionosphere, magnetosphere, etc. According to Kane (1976), in the ionosphere, dynamo action caused by the wind-driven plasma across the geomagnetic field lines is known to be the major source of geomagnetic field variations. The neutral winds (usually tidal oscillations) and distribution of electric conductivity control this dynamo process and

subsequently the changes in the geomagnetic field. Also in the ionosphere, day-to-day changes in thermospheric winds, the E-region tidal winds, and in the conductivity distribution, as well as the magnetic disturbance induced electric fields and winds, are directly responsible for the widely observed variability of the PRE (ABDU et al., 2003), causing the vertical h´F variations. Furthermore, Fagundes et al. (2009) showed that Traveling Planetary Waves Ionospheric Disturbances (TPWIDs) with periods of days also controlled the strength of the electric field PRE and, therefore push the F layer height slowly up and down, according to the TPWID phase. In this study, we looked at planetary wave-like oscillations presented in the ΔH and the vertical h´F during daytime and PRE hours. The F10.7 flux (proxy to the EUV radiation) which is a good indicator of the solar cycle, was analyzed and the results used in discussing some of the results (in the subsequent sections) obtained in this study, since the variation of the electric current intensities may at times be due to the variation of the solar flux (EUV).

Results presented in Figures 48 and 51 show that the variations of the ΔH field in both sectors during the daytime hours differ from the variations observed during PRE. It further showed that during the daytime hours, the wave-like oscillations presented maximum ΔH variations whereas the oscillations during the PRE presented minimum ΔH variations. In the h´F as presented in Figures 54 and 57, it can be seen that the daytime ionosphere shows an increase in height with wave-like oscillations compared to the PRE ionosphere which presents wave-like oscillations yet presents a decrease in height. This increase during the daytime is known to be due to the ionization that occurs during the daytime whilst around PRE, recombination occurs and this trend was seen at both stations. From both results in Figures 48, 51, 54, and 57, a correlation is therefore seen whereby when the wave-like oscillations in ΔH during the daytime for both sectors increase, an increase is also seen in the h´F (for both ARA and SJC). Consequently, when the wave-like oscillations in ΔH at PRE decrease, the h´F also decreased. Furthermore, in ΔH for both sectors, both the daytime and PRE did not show distinct variations from one season to the other but presented distinct variations only when the geomagnetic field was disturbed. However, results from the h´F in Figures 54A and 54B, presented seasonal variations during the daytime hours. The h´F from summer to Autumn begins to decrease gradually and continues through the winter to early spring. However, from late spring to summer the h´F is seen to begin increasing till the end of the year. The increase in the h´F during the daytime summer months can be attributed to the rate of ionization in the ionosphere which tends to increase and leads to this enhancement in h´F during the daytime summer months. However, during the PRE hours presented in Figures 57A and 57B, this

seasonal variation is absent with generally low and similar h´F variations recorded throughout the year because, during PRE, recombination occurs instead of ionization.

Wavelet analysis of these wave-like oscillations seen in Figures 48, 51, 54, and 57 give rise to the results in Figures 49, 52, 55, and 58. Lomb-Scargle analysis was also used together with the wavelet analysis with the results presented in Figures 50, 53, 56, and 59. In both the ΔH and the h´F fields, there is the presence of planetary wave-type periods for both the daytime and PRE, and these period types have also been observed by other researchers (BERTONI et al., 2011; FAGUNDES et al., 2005; RAMKUMAR et al., 2006; YAMAZAKI; DIÉVAL, 2021), together with other periodicities contributing to the variation in the geomagnetic field and ionosphere. In the ΔH, long-term periods together with other periods can be seen clearly in both analysis types whereas in the h´F these long-term periods were not distinctly visible. It was also noted that the long-term periods registered in the ΔH were stronger compared with the other periods. Between 24-28 days in the ΔH during daytime and PRE, very strong oscillations were observed in both analyses. These long-term periods of about 26-27 (24-28 day in our case) day which Fagundes et al. (2005) have attributed to the influence of solar rotation are one of the significant contributors to day-to-day variations. Around 29-30 days during the daytime and PRE, significant periods seen could be due to possible lunar (moon's rotation) contributions to the geomagnetic field since a lunar month (as mentioned in earlier sections) has a mean period of 29.5 days. This means that the major contributing long-term periodicities as presented by the results, to the day-to-day variations in the geomagnetic field are not solely due to planetary wave-type modulations. Also, results from the wavelet and Lomb-Scargle analysis of the F10.7 index in 2018 (LSA) present three peaks between 20-32 days (Figures 47A and 47B). These peaks correlate well with the periods above 20 days in the ΔH in both sectors during the daytime and PRE hours indicating the relationship between the solar and geomagnetic phenomena. However, in the h´F this correlation was not registered. Ramkumar et al. (2006) have reported similar periods near 21 and 30-days generated in the lower atmosphere (troposphere and lower stratosphere) and have stated that these waves have possible influences on the lower E region ionospheric currents at these periodicities.

Besides the long-term periods present in this study, other periods were also presented. From the ΔH analysis in both sectors, 13-14 days can be seen strongly, especially during the daytime which has been attributed to the half-solar rotation (FAGUNDES et al., 2005). Although these periods presented strong oscillations in the geomagnetic field, they were not strongly seen in the F10.7 solar flux. It is interesting to note that, the Lomb-Scargle

Periodogram analysis of the h´F (ARA and SJC) also showed periods between 13-15 days. Results also from the Lomb-Scargle analysis for the daytime hours in the ΔH is related to the oscillations with periods of 5-6 (XIONG et al., 2006), 7-10, and 14-16 days**.** These periods could be related to the planetary wave-type oscillations (10 and 16 days) with the possible influence of the (possible half solar rotation) periods of 13.5-14 days (FAGUNDES et al., 2005)**.** However, the oscillations with periods of 7-10 and 14-16 days present some slight variations during the daytime where their intensities are higher than during PRE hours. Fagundes et al. (2005) mentioned that planetary wave-type oscillations with periods near 10 and 16 days may propagate from the lower atmosphere to ionospheric heights and combine with the oscillations of 13.5 day induced by the Extreme Ultraviolet (EUV) variations, which are related to the solar rotation. The combined effects of these two sources result in the broad period observed around the dominant period and possibly explain the differences in the range of periods during the day. Also, periods of 7-10 days which occurred during the daytime hours were stronger than similar periods which occurred during the PRE hours in the Brazilian sector. This showed that during the daytime, these periods were more prevailing in this sector. It is known that periods of 5-6 and 7-10 days are either due to geomagnetic disturbances (ALTADILL; APOSTOLOV, 2003) or tropospheric sources (LAŠTOVIČKA et al., 2003). In this study, these ranges of periods are possibly due to geomagnetic activities since they were observed in the ΔH of the geomagnetic field whereas in the ionospheric height, however, these periods could be due to both tropospheric sources and geomagnetic disturbances. However, these periods need further investigation in order to determine and establish their sources.

It is worth noting that, the results of the wavelet analysis and Lomb-Scargle in the ΔH, also present Q8DW (Quasi 8-day wave) in both sectors during the daytime and PRE hours. The Q8DW that was also seen in the ionospheric virtual height (h´F) has been shown by Paulino et al. (2021) to modulate the amplitude of the semidiurnal lunar tide (SLT). The authors concluded that since per literature, the dissipative process into the thermosphere does not permit the direct propagation of these waves into higher heights, then this observed Q8DW oscillation reaching ionospheric altitudes could be due to the propagation of the SLT or E-F region dynamo coupling. Eccles et al. (2011) have further proposed that the 14.5 days (which we have also observed in this study) oscillation could contain the influence of the semidiurnal lunar tide, which is a typical semi-monthly oscillation**.**

Generally, in the ΔH, both the Brazilian and African sectors presented similar periods. This is seen in the Lomb-Scargle analysis (Figures 50 and 53) for both daytime and the PRE.

This result agrees well with PW theory that planetary waves are of a global scale. Also, periods observed in the ΔH and h´F in the Brazilian sector were generally different but some similarities were observed in the periods of 14-16 days during the daytime and also during the PRE. Therefore, despite similar wavelike oscillations observed in both sectors, their intensities were different, indicating some longitudinal differences in PW characteristics.

During the intense geomagnetic storm which occurred from DOY 238-239, the wavelet analysis in the ΔH showed some very interesting results. In the Brazilian sector, the range of the periods showed that the waves prevailed over longer periods during daytime than the periods presented during the PRE which presented very short period ranges. However, 15-16 day periods were present during both daytime and PRE. In the African sector also, the range of the wave periods presented during the evening prevailed over those presented during the daytime. Furthermore, whereas in the Brazilian sector, above 16 days were not distinctly present during both daytime and PRE, periods, the African sector, presented periods above 16 days. It is important to point out that, although these periods were observed during the geomagnetic storm, it is however known that, during geomagnetic storms, the intensity and occurrence of periods are influenced by magnetospheric currents (YAMAZAKI, 2014) hence; the periods cannot be attributed solely to geomagnetic activities**.** In Addition, comparing the periods presented during the daytime and PRE in the African sector (Figures 49B and 52B) and Brazilian sector (Figures 49A and 52A), the African sector presented more intense periods than during the same hours in the Brazilian sector indicating differences in response by both sectors to the geomagnetic storm.

According to Fagundes et al. (2009), investigations on the role of PWs on the day-to-day variability of the ionosphere have been carried out by several researchers, especially in the investigation of equatorial related phenomena such as electric field PRE, etc. They pointed out that, although, these equatorial phenomena have strong E/F region and thermosphere-ionosphere couplings, the physics related to the day-to-day variability is complex, and is difficult to research without the use of simultaneous multi-instruments. In this present work, planetary wave-type oscillations with periods of 3-32 days have been observed in the ΔH component of the geomagnetic field and the h´F during daytime and PRE hours in 2018, which could be possible contributors to the modulation in ΔH and h´F.

5.3 Solar tidal response in the ionosphere to the September 7-11, 2017 intense geomagnetic storm.[3]

On September 7-10, 2017, an intense geomagnetic storm occurred which caused a severe disturbance in the ionosphere. The Dst index reached -122 nT at 02:00 UT on September 8, 2017. Since the Dst was lower than < -100 nT, the storm was classified as intense (GONZALEZ et al., 1994). This storm occurred after X2.2 and X9.3 solar flares on September 6, 2017 (for more details, see FAGUNDES et al., 2020). The terrestrial system was disturbed by a complex interplanetary structure with at least two interplanetary clouds (CMEs) after the occurrence of the two solar flares, making the complexity of the ionospheric response and space weather due to CMEs compelling to investigate (Figure 60).

Figure 60 - Daily variations of the geomagnetic indices Dst, Kp and solar wind speed (Vp), proton density (Np), the interplanetary magnetic field component Bz (IMF-Bz), and interplanetary electric field (IEF_y = - Vp Bz), observed from September 6 to September 10, 2017 (data from GOES in blue and SOHO in red). The yellow vertical lines highlight the sudden storm commencements (SSC).

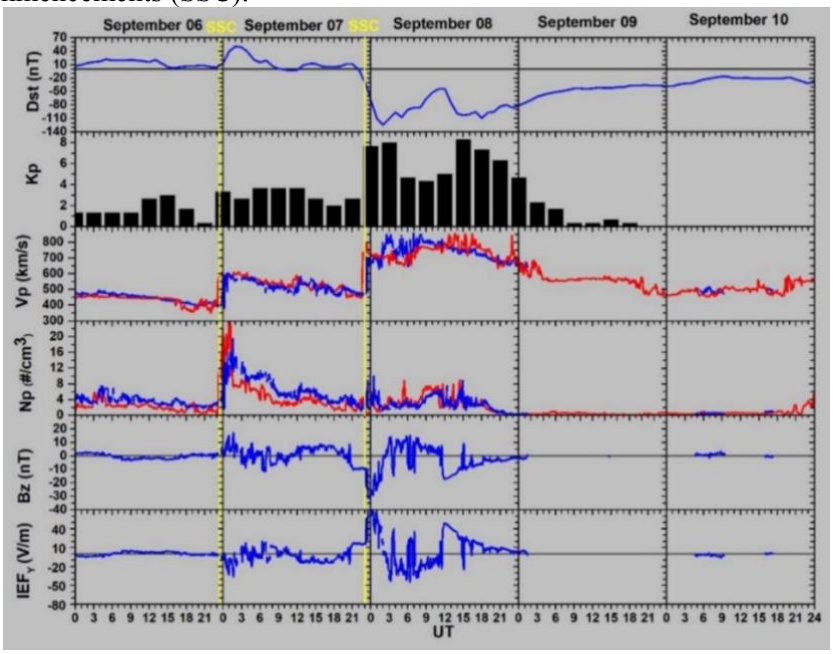

Source: Fagundes et al. (2022)

[3] This section is adapted from the paper published by: P. Fagundes, V. Tsali-Brown, V. Pillat et al. (2022). Ionospheric storm due to solar Coronal mass ejection in September 2017 over the Brazilian and African longitudes, **Advances in Space Research**: https://doi.org/10.1016/j.asr.2022.07.040.

Figure 60 presents the space weather geomagnetic indices Dst and Kp variations (http://wdc.kugi.kyoto-u.ac.jp/) and solar wind parameters Vp, Np, and Bz variations from 06 to 10 September 2017 (http://omniweb.gsfc.nasa.gov/form/omni_min.html). Wu et al. (2019) reported that two interplanetary shocks were recorded during this geomagnetic storm. According to them, the first shock occurred at ~22:41 UT on September 06, 2017 whereas the second shock occurred at 22:48 UT on September 07, 2017. The two SSCs highlighted by the vertical yellow lines on September 06 at 23:43 UT and September 07 at 23:00 UT (https://www.obsebre.es/php/geomagnetisme/vrapides/ssc_2017_d.txt) in Figure 60 are closely related to these two shocks. A strong enhancement in the Dst index can be seen after the first SSC_1. The arrival of the solar wind plasma means there is a simultaneous increase in the wind speed and proton density. However, during this storm, the IMF Bz did not invert (southward) and showed several fluctuations. Due to this, this SSC_1 did not turn into a fully-fledged geomagnetic storm although there was a large energy input. Nevertheless, the interplanetary electric field presented disturbances and an increase in the Kp index. Later, the second SSC_2 took place along with the simultaneous southward inversion of IMF Bz, which turned out to be a strong geomagnetic storm. The onset of the main phase then took place.

Consequently, ionospheric disturbances following the first SSC_1 were expected to be less geo-efficient than the second (SSC_2) since the IMF-Bz was mainly to the north during and after the first SSC_1. However, during the second SSC_2, the IMF-Bz had an incursion southward and IEFy eastward and developed a strong geomagnetic storm main phase, with the Dst reaching -122 nT. Additionally, after the Dst index had reached the minimum value, a ridge in the Dst values was observed which lasted about 10 hours before the recovery phase begun (September 08), indicating the possibility that the CME had an extra third structure.

Researchers like Wu et al. (2019) have suggested that a severe geomagnetic storm would likely be intensified by CME-CME interactions than by a geomagnetic storm caused by a single CME. The solar wind speed (VP) increased from ~400 km/s to ~600 km/s after the first SSC_1 occurred on September 06 and started to decrease slowly. Following the occurrence of the second SSC_2 (07 September), the solar wind increased again from ~500 km/s to ~800 km/s. Furthermore, after the first SSC_1, the proton density (Np) increased from ~4 particles/cm^3 to 15 particles/cm^3, decreased monotonically and had a very small increase after the second SSC_2. The Kp index reached 8 and 8$^+$ on September 08 at 3:00 UT and 15:00 UT in concurrence with the two minima in Dst.

5.3.1 Diurnal, semidiurnal, and terdiurnal solar tidal signatures in geomagnetic field (ΔH) variations over Brazilian and African sectors

In the ionosphere, solar tidal oscillations are a source of geomagnetic field daily variations and are related to ionospheric current systems. Geomagnetic field variations are significantly disturbed during a geomagnetic storm, including the diurnal, semidiurnal, and terdiurnal solar tidal components (ADUSHKIN; RIABOVA; SPIVAK, 2017; ADUSHKIN; SPIVAK; KHARLAMOV, 2017).

To analyze the geomagnetic field disturbances during the storm it was important to know its daily variation during quiet time. Therefore, the geomagnetic ΔH(t) averaged quiet-time (September 1-5 and 16-25, 2017) horizontal component was calculated for all stations used in this investigation. Equation 34 was used to calculate the $\Delta H(t)$ daily variation of the horizontal geomagnetic component,

$$\Delta H(t) = H(t) - H_Q \text{ (midnight LT)} \quad (34)$$

Where H(t) is the daily variation of the observed horizontal component, and H_Q is the average of 5 quietest days during September at midnight LT (DENARDINI et al., 2018; FAGUNDES et al., 2020). Figure 60 is a map showing the 10 stations over the Brazilian and African sectors where the study was carried out. In addition, Table 8 gives further details of these locations. The upper panel in Figure 60B shows the quiet time-averaged variations ΔH calculated for BEL, ARA, EUS, CUI, and CXP (Brazilian sector) and TAM, MBO, TSU, HBK, and HER (African sector) using Equation 34. We present the determined diurnal, semidiurnal, and terdiurnal solar tidal components using wavelet analysis in the second, third, and fourth rows respectively. For further information on this technique (BOLZAN; FRANCO; ECHER, 2020) see section 5.1.1.4 where it has been already addressed. Note that in Figure 61B, the ranges of the y-axis of the diurnal, semidiurnal, and terdiurnal variations are not the same as that of the geomagnetic disturbed time variations (Figure 62). However, it is possible to compare the disturbed and quiet time variations.

Figure 61 - (A) Map showing the 10 magnetometer locations (5 Brazilian and 5 African) used in this study. The Blackline indicates the Magnetic equator. (B) The upper panel shows the daily averaged quiet days (September 1-5 and 16-25, 2017) variations of the geomagnetic ΔH component observed at BEL, ARA, EUB, CUI, and CXP (Brazilian sector), and TAM, MBO, TSU, HBK, and HER (African Sector). Diurnal, semidiurnal, and terdiurnal solar tides components of the geomagnetic ΔH component are shown in the second, third, and fourth rows respectively.

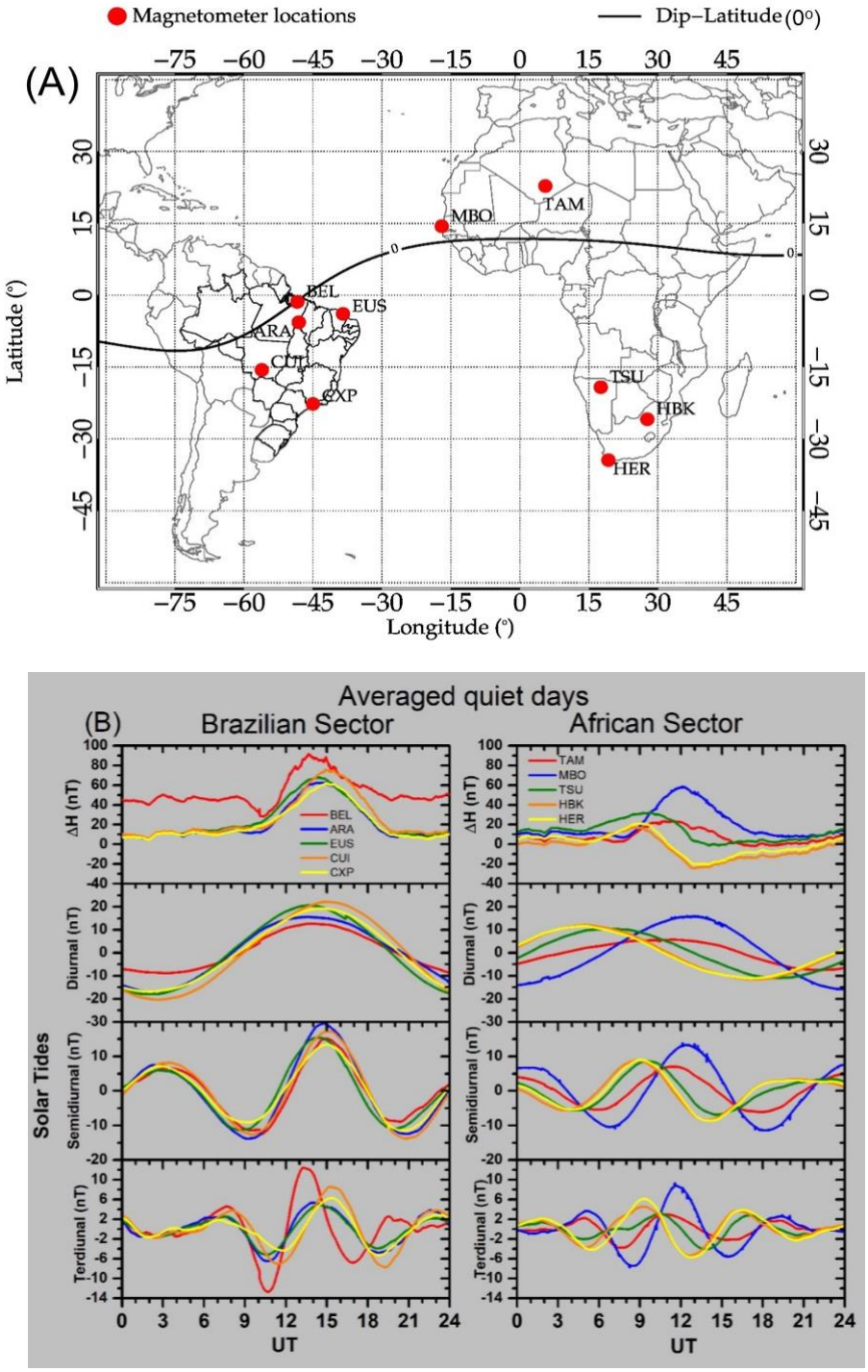

Source: Fagundes et al. (2022)

The stations located near the geomagnetic equatorial region (upper panels - BEL/Brazil and MBO/Africa) present a daily variation with larger amplitudes compared with those stations located at the low latitude and beyond the EIA crest in Figure 61B. The results show that the diurnal and semidiurnal solar tides have the same daily variations and are in phase during quiet time, in the Brazilian sector. However, the African sector presents different daily variations in the diurnal and semidiurnal components. In addition, it is possible to group the daily variations into two, where TAM (NH) and MBO (EQU) are almost in phase and on the other hand, TSU, HBK, and HER (SH) are also almost in phase. In the Brazilian and African sectors, the terdiurnal variations present completely out of phase daily variations. Where each station presented different amplitudes and phases, indicating that the terdiurnal variation was strongly affected by latitude during quiet time.

Table 7- Magnetometer station names, codes, geographic coordinates, and dip-latitudes over the Brazilian and African sectors.

Magnetometer Station Name	Station Codes	Geo. Lat. (+N)	Geo. Lon. (+W)	Dip. Lat. (+N)
Brazilian Sector				
Belem	BEL	-01.4	48.4	-00.5
Araguatins	ARA	-05.6	48.7	-04.1
Eusebio	EUS	-03.9	38.4	-08.4
Cuiaba	CUI	-15.6	56.1	-08.9
Cachoeira Paulista	CXP	-22.7	45.0	-20.5
Magnetometer Station Name	**Station Codes**	**Geo. Lat. (+N)**	**Geo. Lon. (+W)**	**Dip. Lat. (+N)**
African Sector				
Tamanrasset	TAM	22.8	-05.5	14.4
Mbour	MBO	14.4	17.0	04.2
Tsumeb	TSU	-19.2	-17.6	-39.1
Hartebeesthoek	HBK	-25.9	-27.7	-41.9
Hermanus	HER	-34.4	-19.2	-45.9

Source: Fagundes et al. (2022)

It can be seen in Figures 62A and 62B that after the SSC_1 and SSC_2 of the geomagnetic storm (September 07-08, 2017), the geomagnetic disturbance in the ΔH daily variations near geomagnetic equatorial stations, BEL (upper panel, Brazilian sector) and MBO (upper panel, African sector) was higher compared to other locations. On 07 September, BEL in the Brazilian sector recorded the highest ΔH values. They occurred after the SSC_1 with the

ΔH component of around 140nT. This was the highest recorded disturbance value for both sectors although MBO also recorded a disturbance value of around 100nT. The disturbances recorded in the ΔH component at the equatorial stations in both sectors are possibly related to the disturbed equatorial electrojet due to the geomagnetic storm. Comparatively, the low latitude locations over Brazil (ARA, EUS, CUI, and CXP) showed ΔH daily variation similar to the equatorial station BEL. However, in the African sector, TAM presented a similar ΔH daily variation as MBO whereas TSU and HBK presented ΔH daily variations similar to that of HER.

Figure 62 - (A) Daily variation of the ΔH component along with diurnal, semidiurnal, and terdiurnal solar tidal components observed at BEL, ARA, EUB, CUI, and CXP (Brazilian sector) during the main phase on September 07-08, 2017, and recovery phase on September 08-11, 2017. (B) The same as (A) but for TAM, MBO, TSU, HBK, and HER (African sector).

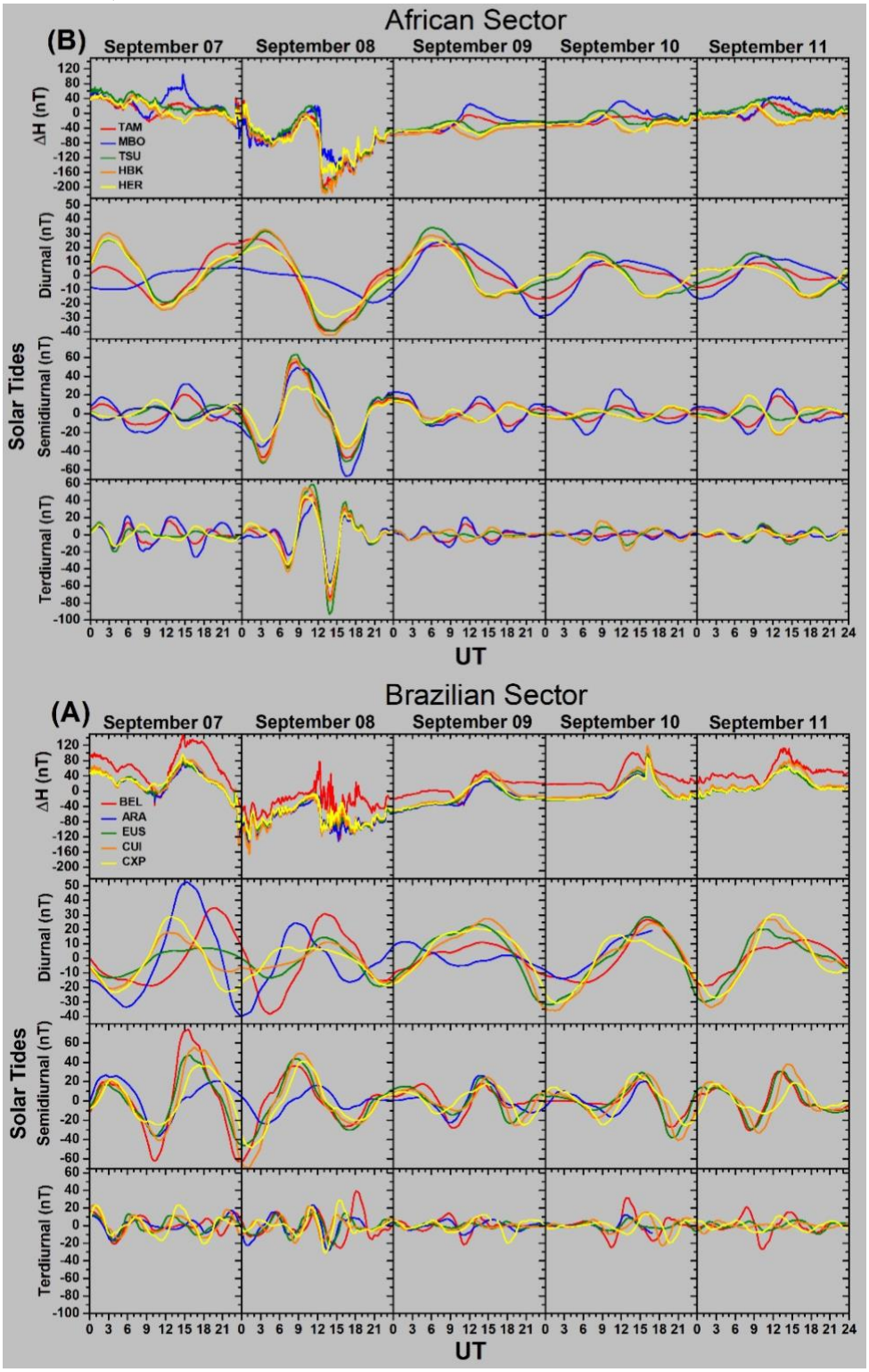

Source: Fagundes et al. (2022)

Results show that on September 08 (Figures 62A and 62B), the ΔH daily variations at all the stations in both the Brazilian and African sectors were in phase. Further, a ridge seen in the Dst index in Figure 60 within the same period was noticed in both sectors. This ridge presented a peak around 12:00UT in both sectors with a negative decent phase noticed afterward. Throughout the geomagnetic storm, the minimum disturbance value recorded was around -210nT, during the negative descent and at HBK. Furthermore, the ΔH variations at all stations presented some ripple-like structures with the most prominent ripples recorded at BEL, which happened to present the highest disturbance on that day. These ripples occurred some hours apart; the first occurring immediately after the second storm and the second occurring, some hours after, coinciding with the ridge which appeared on that day. After the recovery phase was initiated, the ripples persisted for some hours.

The ΔH values gradually returned to their equilibrium state during the recovery phase, which began in the latter part of September 08. However, on September 09, 10, and 11, some disturbances were seen in the geomagnetic field. These disturbances were seen in both the Brazilian and African sectors with the near-equatorial stations' BEL and MBO presenting the highest disturbances in their respective sectors.

Geomagnetic storms sometimes cause disturbances in tidal components and these can cause transitory enhanced variations. The result of this study showed that there was a strong presence of and an enhancement in the diurnal component of the solar tide in the geomagnetic field in both sectors during the disturbed and quiet time. However, during the disturbed time, the enhancement in the diurnal component was stronger compared to quiet time. Furthermore, on September 07 and 08, all the Brazilian stations were out of phase during the disturbed time whereas, in the African sector except MBO, all the stations were in phase during this period. Also, the highest amplitude recorded in the diurnal component was at ARA on September 07 in the Brazilian sector, whilst the least amplitude recorded in this component was in the African sector at HBK on September 08.

During the disturbed and quiet periods in both sectors, there is a strong presence of the semidiurnal component. However, the average semidiurnal component at all the stations during the quiet period in the Brazilian sector was in phase whereas the stations in the African sector were out of phase. Except for ARA, which was out of phase on September 07-08, all the other stations in the Brazilian sector were in phase during the disturbed period. The stations in the African sector however were in phase only on September 08. Furthermore, the highest and

lowest amplitudes for both sectors during the disturbed period were recorded at BEL on September 07 at about 15:00UT and CUI on September 08 at around 01:00UT respectively.
In the Brazilian and African sectors, the terdiurnal components at all the stations during the disturbed and quiet times were out of phase except on September 08, when all the stations in the African sector were in phase. In addition, the maximum-recorded amplitude in both sectors was around 60nT which occurred in TSU at 11:00UT while the minimum amplitude was around -90nT, also occurring in TSU in the African sector at 14:00UT.

Generally, as expected the geomagnetic field during the storm time presented strong enhancements, with the solar diurnal and semidiurnal components showing a strong presence during the same period in both sectors. Furthermore, the geomagnetic field gradually returned to its equilibrium state during the recovery phase, although some disturbances were present during this period. On September 08, except for the diurnal component at MBO, it is interesting to note that, the diurnal, semidiurnal, and terdiurnal components at all the stations in the African sector were in phase. On this day in this sector, all the components also presented the maximum and minimum disturbances.

6 CONCLUSIONS AND SUGGESTIONS FOR FUTURE WORK

This thesis presents and discusses tidal and planetary waves in the ionosphere. The investigations were carried out in the Brazilian and African sectors in the years 2017 and 2018. Solar and lunar tides were investigated using data from the magnetometer and planetary wave-type oscillations were further investigated using data from the magnetometer and the ionosonde. QT and QT+DT seasonal as well as station-to-station variations in both tidal fields were investigated. Also, day-to-day variations with their accompanying periodicities have been investigated in the planetary wave-type field in both the ΔH and $h'F$. Therefore, from the investigations, it is possible to present the main results of this work:

6.1 CONCLUSIONS

6.1.1 Solar Tides

1. Periods relating to solar tides in the geomagnetic field were observed in the two sectors.

2. For all three solar tidal components studied, the diurnal solar tide presented the highest amplitude variations in both the Brazilian and African sectors followed by the semidiurnal amplitudes.

3. The terdiurnal solar tide in both sectors generally presented semiannual variations. The behavior of the terdiurnal solar tide at HER whereby it presented the highest amplitudes was unexpected since it happened to be the station furthest from the geomagnetic equator in this study. We need to investigate further in order to understand and explain this behavior.

4. Seasonally, the maximum diurnal QT and QT+DT amplitude variations for both sectors were recorded in the Brazilian sector during March (autumn) whereas; the African sector recorded the minimum value for both sectors during June and July.

6.1.2 Sudden Stratospheric Warming Event of February 2018

The latitudinal response of the solar tidal components to the major SSW event of 2018 was studied and the conclusions are as follows;

1. Enhancements were observed in the solar tidal components at three selected stations during the SSW event of 2018.

2. TAM in the African low latitude presented stronger enhancements in all three components studied. It was suggested that this could be due to the station's nearness to the geomagnetic equator. Interestingly, HER at the mid-latitude however, presented much stronger enhancement than TSU, also at the low-latitude.

6.1.3 Lunar Tides

1. Periods relating to lunar tides in the geomagnetic field were observed in the two sectors.

2. The highest lunar tide (semidiurnal) amplitude attained in both sectors was in the Brazilian sector during both the QT and QT+DT. Generally, the Brazilian sector registered higher amplitude variations than the African sector.

3. Seasonal and semiannual variations were observed in both the Brazilian and African Sectors. An annual variation was presented by a station in the African sector.

4. An interesting result was observed in the African sector where HER, which is far away from the geomagnetic equator, recorded higher amplitude variations than some stations closest to the geomagnetic equator. We, could, however, not explain this result.

- It is important to state that, the semidiurnal solar tides presented higher amplitudes compared to the semidiurnal lunar tides in both sectors during both the QT and QT+DT, which was expected.

6.1.4 Planetary waves

1. The ΔH of the geomagnetic field and the ionospheric virtual height are organized into one value per day for each hour 12:00LT, 13:00LT, 14:00LT, and 15:00LT (daytime) and 18:00LT, 19:00LT, 20:00LT, 21:00LT, and 22:00LT (evening). This methodology allowed us to determine long-term series of daily ΔH variations independent of tidal components. It was noticed that using this methodology the oscillations in ΔH were neither flat nor random but oscillated with specific periods of days that are related to PW. However, this methodology of using one value per day for each hour allowed us to identify waves with periods of 3 days and over.

2. Using wavelet and Lomb-Scargle techniques, planetary waves with periods between 3 to 32 days in the ΔH (in the Brazilian and African sectors) and the virtual height (Brazilian sector) of the ionosphere were recorded. The ΔH of each period was a little different for each sector, but the main periods were presented in both sectors. In addition, some of these periods were seen in the virtual height results. This agreed well with the theory that these planetary waves have a global scale and contribute to the day-to-day variability of the geomagnetic field and the ionosphere.

3. Long-term periods (26-28 day) and 29-30 day (synodic month has a mean period of 29.5 day) were found to contribute to the day-to-day variability in both the Brazilian and African sectors during the daytime and evening (PRE). However, these long-term periods were not prominent and were sometimes barely present in the ionospheric virtual height. A correlation was further found to exist between the F10.7 solar flux periods between 20-32 days and the long-term periods of 20-32 days in the ΔH component.

4. The dominant short-term period of 7-10 days, which we can term as the 10-day period (KOHSIEK; GLASSMEIER; HIROOKA, 1995) in both sectors during the daytime, was stronger than during evening (PRE). Periods of 7-10 day, 12-16 day, 20-24 day, and 25-32 day waves present in the daytime in the Brazilian sector agreed with periods present in the African sector with differences only in their intensity. Also, periods of 8-10 day, 12-16 day, 20-24 day, and 25-32 day waves presented during PRE in both

sectors were in agreement. In addition, short-term periods of 13-14 day waves were found to contribute significantly in both sectors in both ΔH and the ionospheric virtual height.

5. Peak periods presented at 13-16 days during some of the selected hours could be the quasi-16-day wave (Q16DW) studied by various researchers. However further analysis needs to be carried out to confirm this.

6. During the storm time, both sectors presented significant periods for the selected hours understudy with periods prevailing for days in the African sector during the daytime than in the Brazilian sector. It is however important to note that, these periods are influenced by the magnetospheric currents, hence were solely not due to planetary waves.

6.1.5 Solar tidal response in the ionosphere to the September 7-11, 2017 intense geomagnetic storm

Using networks of magnetometers, the ionospheric response to the September 7-11, 2017 intense geomagnetic storm was investigated. The main conclusions of this investigation regarding the tidal components have been summarized as follows:

1. The ΔH component variations in the Brazilian and African sectors were disturbed during the main phase and also during the Dst ridge on September 08, 2017, as compared with the quiet geomagnetic period. The diurnal, semidiurnal, and terdiurnal ΔH components daily variation and intensity were disturbed during the geomagnetic storms on September 07-08, 2017. The ΔH component variations in the American and African sectors showed different responses due to geomagnetic storms suggesting the presence of longitudinal dependence.
2. There were strong positive ionospheric storm effects during the geomagnetic storm main phase (September 07 and 08, 2017) and during the Dst ridge on September 08, 2017. The positive ionospheric storm effects occurred both in the Brazilian and African sectors.

6.2 SUGGESTIONS FOR FUTURE WORK

This work aims to contribute to the understanding of studies regarding atmospheric tides, planetary waves, and their behavior in the ionosphere during geomagnetically disturbed (storm) and quiet days and during other geophysical events. However, to better understand the electrodynamic processes related to the coupling of the ionosphere-thermosphere system and to know the sources of the waves observed further studies are needed. Therefore, some recommendations for future work are to study the:

- lunar tides during the SSW event that occurred in order to observe their behavior as it is known that lunar tides are affected and respond well during SSWs;

- sources of the waves (solar, lunar tidal, and planetary) that were observed in the ionosphere. This would help us gain more understanding into the dynamics of the waves;

- planetary wave response during the SSW event since they are known to be indicators to this event;

- solar tides, lunar tides, and planetary waves observed in this study in the EEJ.

REFERENCES

ABADI, P.; OTSUKA, Y.; TSUGAWA, T. Effects of pre-reversal enhancement of E B drift on the latitudinal extension of plasma bubble in Southeast Asia. **Earth, Planets and Space**, v. 67, n. 1, p. 1–7, 2015.

ABDU, M. A. et al. Equatorial evening prereversal electric field enhancement and sporadic E layer disruption: A manifestation of E and F region coupling. **Journal of Geophysical Research: Space Physics**, v. 108, n. A6, 2003.

ABDU, M. A. et al. Planetary wave signatures in the equatorial atmosphere–ionosphere system, and mesosphere-E-and F-region coupling. **Journal of Atmospheric and Solar-Terrestrial Physics**, v. 68, n. 3–5, p. 509–522, 2006.

ABDU, M. A. Equatorial spread F development and quiet time variability under solar minimum conditions. **94.20. dj; 94.20. dt; 96.60. qd**, 2012.

ADUSHKIN, V. V; RIABOVA, S. A.; SPIVAK, A. A. Lunar–solar tide effects in the Earth's crust and atmosphere. **Izvestiya, Physics of the Solid Earth**, v. 53, p. 565–580, 2017.

ADUSHKIN, V. V; SPIVAK, A. A.; KHARLAMOV, V. A. **A new method of testing of the Earth's free oscillations on the basis of geomagnetic variation analysis**. Doklady Earth Sciences. **Anais**...2017.

AKASOFU, S.-I.; CHAPMAN, S. On the asymmetric development of magnetic storm fields in low and middle latitudes. **Planetary and Space Science**, v. 12, n. 6, p. 607–626, 1964.

ALTADILL, D.; APOSTOLOV, E. M. Time and scale size of planetary wave signatures in the ionospheric F region: Role of the geomagnetic activity and mesosphere/lower thermosphere winds. **Journal of Geophysical Research: Space Physics**, v. 108, n. A11, 2003.

AMBRIZZI, T.; HOSKINS, B. J. Stationary Rossby-wave propagation in a baroclinic atmosphere. **Quarterly Journal of the Royal Meteorological Society**, v. 123, n. 540, p. 919–928, 1997.

AUSTRALIAN SPACE WEATHER FORECASTING CENTRE. **Ionosonde**.

BALDWIN, M. P. et al. Sudden stratospheric warmings. **Reviews of Geophysics**, v. 59, n. 1, p. e2020RG000708, 2021.

BARTELS, J.; JOHNSTON, H. F. Geomagnetic tides in horizontal intensity at Huancayo, Part II. **Terrestrial Magnetism and Atmospheric Electricity**, v. 45, n. 4, p. 485–512, 1940a.

BARTELS, J.; JOHNSTON, H. F. Geomagnetic tides in horizontal intensity at Huancayo. **Terrestrial Magnetism and Atmospheric Electricity**, v. 45, n. 3, p. 269–308, 1940b.

BEER, T. Atmospheric waves. **New York**, 1974.

BERTONI, F. C. P. et al. Equatorial spread-F occurrence observed at two near equatorial stations in the Brazilian sector and its occurrence modulated by planetary waves. **Journal of atmospheric and solar-terrestrial physics**, v. 73, n. 4, p. 457–463, 2011.

BLUME, C.; MATTHES, K.; HORENKO, I. Supervised learning approaches to classify sudden stratospheric warming events. **Journal of the atmospheric sciences**, v. 69, n. 6, p. 1824–1840, 2012.

BOLZAN, M. J. A.; FRANCO, A. M. S.; ECHER, E. A wavelet based method to remove the long term periodicities of geophysical time series. **Advances in Space Research**, v. 66, n. 2, p. 299–306, 2020.

BROWN, G. M.; WILLIAMS, D. C. Pressure variations in the stratosphere and ionosphere. **Journal of Atmospheric and Terrestrial Physics**, v. 33, n. 9, p. 1321–1328, 1971.

BRUNT, D. **Physical and dynamical meteorology**. [s.l.] Cambridge University Press, 2011.

BUTLER, S. T.; SMALL, K. A. The excitation of atmospheric oscillations. **Proceedings of the Royal Society of London. Series A. Mathematical and Physical Sciences**, v. 274, n. 1356, p. 91–121, 1963.

CAHILL JR, L. J. Inflation of the inner magnetosphere during a magnetic storm. **Journal of Geophysical Research**, v. 71, n. 19, p. 4505–4519, 1966.

CAMPBELL, W. H. **Introduction to geomagnetic fields**. [s.l.] Cambridge University Press, 2003.

CHANG, L. C.; LIU, J.-Y.; PALO, S. E. Propagating planetary wave coupling in SABER MLT temperatures and GPS TEC during the 2005/2006 austral summer. **Journal of Geophysical Research: Space Physics**, v. 116, n. A10, 2011.

CHAPMAN, S. The semidiurnal oscillation of the atmosphere. **Quarterly Journal of the Royal Meteorological Society**, v. 50, n. 211, p. 165–195, 1924.

CHAPMAN, S.; BARTELS, J. Geomagnetism, vol. II: Analysis of the data, and physical theories. **Geomagnetism**, 1940.

CHAPMAN, S.; LINDZEN, R. S. **Atmospheric tides: thermal and gravitational**. [s.l.] Springer Science & Business Media, 1969. v. 15

CHAU, J. L. et al. Equatorial and low latitude ionospheric effects during sudden stratospheric warming events: Ionospheric effects during SSW events. **Space Science Reviews**, v. 168, p. 385–417, 2012.

CHEN, P.-R. Two-day oscillation of the equatorial ionization anomaly. **Journal of Geophysical Research: Space Physics**, v. 97, n. A5, p. 6343–6357, 1992.

CHEN, Y.-W.; MIYAHARA, S. Analysis of fast and ultrafast Kelvin waves simulated by the Kyushu-GCM. **Journal of atmospheric and solar-terrestrial physics**, v. 80, p. 1–11, 2012.

COHEN, J.; JONES, J. Tropospheric precursors and stratospheric warmings. **Journal of climate**, v. 24, n. 24, p. 6562–6572, 2011.

CURRIE, R. G. Lunar terms in the geomagnetic spectrum at Hermanus. **Journal of Atmospheric and Terrestrial Physics**, v. 37, n. 3, p. 439–446, 1975.

DAUBECHIES, I. **Ten lectures on wavelets**. [s.l.] SIAM, 1992.

DE MORAES, J. F. et al. **Evidence of the lunar tide in the ionosphere**. 15th International Congress of the Brazilian Geophysical Society & EXPOGEF, Rio de Janeiro, Brazil, 31 July-3 August 2017. **Anais**...2017.

DENARDINI, C. M. et al. The embrace magnetometer network for South America: Network description and its qualification. **Radio Science**, v. 53, n. 3, p. 288–302, 2018.

DENARDINI, C. M. et al. Ionospheric scale index map based on TEC data during the Saint Patrick magnetic storm and EPBs. **Space Weather**, v. 18, n. 9, p. e2019SW002330, 2020.

DOODSON, A. T. The harmonic development of the tide-generating potential. **Proceedings of the Royal Society of London. Series A, Containing Papers of a Mathematical and Physical Character**, v. 100, n. 704, p. 305–329, 1921.

ECCLES, V. et al. Lunar atmospheric tidal effects in the plasma drifts observed by the Low-Latitude Ionospheric Sensor Network. **Journal of Geophysical Research: Space Physics**, v. 116, n. A7, 2011.

ECCLES, J. V; ST. MAURICE, J. P.; SCHUNK, R. W. Mechanisms underlying the prereversal enhancement of the vertical plasma drift in the low-latitude ionosphere. **Journal of Geophysical Research: Space Physics**, v. 120, n. 6, p. 4950–4970, 2015.

ELFORD, W. G. A study of winds between 80 and 100 km in medium latitudes. **Planetary and Space Science**, v. 1, n. 2, p. 94–101, 1959.

ELHAWARY, R.; FORBES, J. M. Planetary wave variability of Sq currents. **Journal of Geophysical Research: Space Physics**, v. 121, n. 11, p. 11–316, 2016.

EMBRACE. **Magnetometer-About, Estudo e monitoramento Brasileiro clima espacial,**.

FAGUNDES, P. R. et al. Observations of F layer electron density profiles modulated by planetary wave type oscillations in the equatorial ionospheric anomaly region. **Journal of Geophysical Research: Space Physics**, v. 110, n. A12, 2005.

FAGUNDES, P. R. et al. F layer postsunset height rise due to electric field prereversal enhancement: 1. Traveling planetary wave ionospheric disturbance effects. **Journal of Geophysical Research (Space Physics)**, v. 114, n. A12, p. A12321, 2009.

FAGUNDES, P. R. et al. Ionospheric disturbances in a large area of the terrestrial globe by two strong solar flares of September 6, 2017, the strongest space weather events in the last decade. **Advances in Space Research**, v. 66, n. 7, p. 1775–1791, 2020.

FAGUNDES, P. R. et al. Ionospheric storm due to solar Coronal mass ejection in September 2017 over the Brazilian and African longitudes. **Advances in Space Research**, v. 71, n. 1, p. 46–66, 2022.

FARGE, M. Wavelet transforms and their applications to turbulence. **Annual review of fluid mechanics**, v. 24, n. 1, p. 395–458, 1992.

FEJER, B. G. et al. Lunar-dependent equatorial ionospheric electrodynamic effects during sudden stratospheric warmings. **Journal of Geophysical Research: Space Physics**, v. 115, n. A8, 2010.

FORBES, J. M. Tidal and planetary waves. **The upper mesosphere and lower thermosphere: A review of experiment and theory**, v. 87, p. 67–87, 1995.

FORBES, J. M.; LEVERONI, S. Quasi 16-day oscillation in the ionosphere. **Geophysical Research Letters**, v. 19, n. 10, p. 981–984, 1992.

FORBES, J. M.; PALO, S. E.; ZHANG, X. Variability of the ionosphere. **Journal of Atmospheric and Solar-Terrestrial Physics**, v. 62, n. 8, p. 685–693, 2000.

FORBES, J. M.; ZHANG, X. Quasi 2-day oscillation of the ionosphere: A statistical study. **Journal of Atmospheric and Solar-Terrestrial Physics**, v. 59, n. 9, p. 1025–1034, 1997.

FORBES, J. M.; ZHANG, X. Lunar tide in the F region ionosphere. **Journal of Geophysical Research: Space Physics**, v. 124, n. 9, p. 7654–7669, 2019.

FRIEDMAN, J. S. et al. Longitude variations of the solar semidiurnal tides in the mesosphere and lower thermosphere at low latitudes observed from ground and space. **Journal of Geophysical Research: Atmospheres**, v. 114, n. D11, 2009.

FRITTS, D. C. Gravity wave-tidal interactions in the middle atmosphere: Observations and theory. **The upper mesosphere and lower thermosphere: a review of experiment and theory**, v. 87, p. 121–131, 1995.

GARFINKEL, C. I.; BENEDICT, J. J.; MALONEY, E. D. Impact of the MJO on the boreal winter extratropical circulation. **Geophysical Research Letters**, v. 41, n. 16, p. 6055–6062, 2014.

GELLER, M. A.; SCHOEBERL, M. R. **Calculation of the lunar diurnal atmospheric tide**. [s.l: s.n.].

GHOSH, P. et al. Day-to-day variation of pre-reversal enhancement in the equatorial ionosphere based on GAIA model simulations. **Earth, Planets and Space**, v. 72, n. 1, p. 1–8, 2020.

GONZALEZ, W. D. et al. What is a geomagnetic storm? **Journal of Geophysical Research: Space Physics**, v. 99, n. A4, p. 5771–5792, 1994.

GOODY, R. M. The influence of radiative transfer on the propagation of a temperature wave in a stratified diffusing atmosphere. **Journal of Fluid Mechanics**, v. 9, n. 3, p. 445–454, 1960.

GOSSARD, E. E.; HOOKE, W. H. Waves in the atmosphere: atmospheric infrasound and gravity waves-their generation and propagation. **Atmospheric Science**, v. 2, 1975.

GREENHOW, J. S.; NEUFELD, E. L. Winds in the upper atmosphere. **Quarterly Journal of the Royal Meteorological Society**, v. 87, n. 374, p. 472–489, 1961.

GURUBARAN, S.; RAJARAM, R. Signatures of equatorial electrojet in the mesospheric partial reflection drifts over magnetic equator. **Geophysical research letters**, v. 27, n. 7, p. 943–946, 2000.

HALDOUPIS, C.; PANCHEVA, D. Planetary waves and midlatitude sporadic E layers: Strong experimental evidence for a close relationship. **Journal of Geophysical Research: Space Physics**, v. 107, n. A6, p. SIA–3, 2002.

HARRIS, T. J. A long-term study of the quasi-two-day wave in the middle atmosphere. **Journal of atmospheric and terrestrial physics**, v. 56, n. 5, p. 569–579, 1994.

HARRIS, T. J.; VINCENT, R. A. The quasi-two-day wave observed in the equatorial middle atmosphere. **Journal of Geophysical Research: Atmospheres**, v. 98, n. D6, p. 10481–10490, 1993.

HAURWITZ, B. Die tägliche Periode der Lufttemperatur in Bodennähe und ihre geographische Verteilung. **Archiv für Meteorologie, Geophysik und Bioklimatologie, Serie A**, v. 12, p. 426–434, 1962.

HAURWITZ, B. Atmospheric Tides: These oscillations are caused by the gravitational pull of sun and moon and by the sun's thermal effects. **Science**, v. 144, n. 3625, p. 1415–1422, 1964.

HAURWITZ, B.; COWLEY, D. The lunar barometric tide, its global distribution and annual variation. **pure and applied geophysics**, v. 77, p. 122–150, 1969.

HOCKE, K. **Tidal variations in the high-latitude E-and F-region observed by EISCAT**. Annales Geophysicae. **Anais**...1996.

HORNE, J. H.; BALIUNAS, S. L. A prescription for period analysis of unevenly sampled time series. **The Astrophysical Journal**, v. 302, p. 757–763, 1986.

HOSKINS, B. J.; KAROLY, D. J. The steady linear response of a spherical atmosphere to thermal and orographic forcing. **Journal of the atmospheric sciences**, v. 38, n. 6, p. 1179–1196, 1981.

HOUGH, S. S. V. On the application of harmonic analysis to the dynamical theory of the tides.—Part II. On the general integration of Laplace's dynamical equations. **Philosophical Transactions of the Royal Society of London. Series A, Containing Papers of a Mathematical or Physical Character**, n. 191, p. 139–185, 1898.

HUANG, K. M. et al. Nonlinear coupling between quasi 2 day wave and tides based on meteor radar observations at Maui. **Journal of Geophysical Research: Atmospheres**, v. 118, n. 19, p. 10–936, 2013.

IMO. **INTERMAGNET Magnetic Observatories**.

INTERMAGNET. **International Real-time Magnetic Observatory Network**.

JACOBI, C. et al. The CPW-TEC project: Planetary waves in the middle atmosphere and ionosphere. **Advances in Radio Science**, v. 5, p. 393–397, 2007.

JONES, M. W.; JONES, J. G. Tidal effects in the ionospheric F-layer. **Journal of Atmospheric Sciences**, v. 7, n. 1, p. 14–20, 1950.

KANE, R. P. Geomagnetic field variations. **Space Science Reviews**, v. 18, n. 4, p. 413–540, 1976.

KATO, S. Horizontal Wind Systems in the ionospheric E region Deduced from the Dynamo Theory of the Geomagnetic Sq variation Part II. Rotating Earth. **Journal of geomagnetism and geoelectricity**, v. 8, n. 1, p. 24–37, 1956.

KERTZ, W. **Die thermische Erregungsquelle der atmosphärischen Gezeiten**. [s.l: s.n.].

KOHSIEK, A.; GLASSMEIER, K. H.; HIROOKA, T. **Periods of planetary waves in geomagnetic variations**. Annales geophysicae. **Anais**...1995.

KONDRAT'YEV, K. Y. **Radiative heat exchange in the atmosphere**. [s.l.] Elsevier, 2013.

KUO, H. L. The thermal interaction between the atmosphere and the earth and propagation of diurnal temperature waves. **Journal of the Atmospheric Sciences**, v. 25, n. 5, p. 682–717, 1968.

KUTIEV, I. et al. Solar activity impact on the Earth's upper atmosphere. **Journal of Space Weather and Space Climate**, v. 3, p. A06, 2013.

LAMB, H. Hydrodynamics. **Aufl., Cambridge: Univ. Press1879–1932**, v. 427, 1932.

LAPLACE, P. S. **Traité de mécanique céleste**. [s.l.] de l'Imprimerie de Crapelet, 1799. v. 1

LAŠTOVIČKA, J. Observations of tides and planetary waves in the atmosphere-ionosphere system. **Advances in Space Research**, v. 20, n. 6, p. 1209–1222, 1997.

LAŠTOVIČKA, J. et al. **Persistence of the planetary wave type oscillations in foF2 over Europe**. Annales Geophysicae. **Anais**...2003.

LAŠTOVIČKA, J. Forcing of the ionosphere by waves from below. **Journal of Atmospheric and Solar-Terrestrial Physics**, v. 68, n. 3–5, p. 479–497, 2006.

LEOVY, C. Radiative equilibrium of the mesosphere. **Journal of Atmospheric Sciences**, v. 21, n. 3, p. 238–248, 1964.

LIMA, L. M. et al. Sudden stratospheric warming effects on the mesospheric tides and 2-day wave dynamics at 7 S. **Journal of atmospheric and solar-terrestrial physics**, v. 78, p. 99–107, 2012.

LINDZEN, R. S. Thermally driven diurnal tide in the atmosphere. **Quarterly Journal of the Royal Meteorological Society**, v. 93, n. 395, p. 18–42, 1967.

LIU, H.-L. Variability and predictability of the space environment as related to lower atmosphere forcing. **Space Weather**, v. 14, n. 9, p. 634–658, 2016.

LOMB, N. R. Least-squares frequency analysis of unequally spaced data. **Astrophysics and space science**, v. 39, p. 447–462, 1976.

MAEDA, H. Horizontal Wind Systems in the Ionospheric E Region Deduced from the Dynamo Theory of the Geomagnetic Sq Variation Part I. Non-rotating Earth. **Journal of geomagnetism and geoelectricity**, v. 7, n. 4, p. 121–132, 1955.

MAEDA, H.; FUJIWARA, M. Lunar ionospheric winds deduced from the dynamo theory of geomagnetic variations. **Journal of Atmospheric and Terrestrial Physics**, v. 29, n. 8, p. 917–936, 1967.

MANSON, A. H. et al. Climatologies of semi-diurnal and diurnal tides in the middle atmosphere (70–110 km) at middle latitudes (40–55). **Journal of Atmospheric and Terrestrial Physics**, v. 51, n. 7–8, p. 579–593, 1989.

MANSON, A. H. et al. **Arctic tidal characteristics at Eureka (80° N, 86° W) and Svalbard (78° N, 16° E) for 2006/07: seasonal and longitudinal variations, migrating and non-migrating tides**. Annales Geophysicae. **Anais**...2009.

MATSUSHITA, S. Solar quiet and lunar daily variation fields. Em: **International Geophysics**. [s.l.] Elsevier, 1967. v. 11p. 301–424.

MENDILLO, M. et al. Modelling F2-layer seasonal trends and day-to-day variability driven by coupling with the lower atmosphere. **Journal of Atmospheric and Solar-Terrestrial Physics**, v. 64, n. 18, p. 1911–1931, 2002.

NEWTON, I. Philosophiæ naturalis principia mathematica (Mathematical principles of natural philosophy). **London (1687)**, v. 1687, p. 1687, 1687.

NYASSOR, P. K. **A study on the generation and propagation of concentric gravity waves over Brazil**. São José dos Campos: INPE, , 2021.

OBERHEIDE, J. et al. Dynamical meteorology| atmospheric tides. 2015.

ONWUMECHILLI, C. A.; ALEXANDER, N. S. Variations in the geomagnetic field at Ibadan, Nigeria—II Lunar and luni-solar variations in H and Z. **Journal of Atmospheric and Terrestrial Physics**, v. 16, n. 1–2, p. 115–123, 1959.

PANCHEVA, D. et al. Evidence of a role for modulated atmospheric tides in the dependence of sporadic E layers on planetary waves. **Journal of Geophysical Research: Space Physics**, v. 108, n. A5, 2003.

PANCHEVA, D.; ALBERCA, L. F.; LA MORENA, B. A. Simultaneous observation of the quasi-two-day variations in the lower and upper ionosphere over Europe. **Journal of atmospheric and terrestrial physics**, v. 56, n. 1, p. 43–50, 1994.

PAULINO, A. R. et al. The lunar tides in the mesosphere and lower thermosphere over Brazilian sector. **Journal of Atmospheric and Solar-Terrestrial Physics**, v. 133, p. 129–138, 2015.

PAULINO, A. R. et al. **Variability of the lunar semidiurnal tidal amplitudes in the ionosphere over Brazil**. Annales Geophysicae. **Anais**...2021.

PAULINO, A. R.; BATISTA, P. P.; CLEMESHA, R. Lunar tides in the mesosphere and lower thermosphere over Cachoeira Paulista (22.7° S; 45.0° W). **Journal of atmospheric and solar-terrestrial physics**, v. 78, p. 31–36, 2012.

PAULINO, A. R. S. **Estudo global da maré lunar na média atmosfera através de medidas por satélite**. São José dos Campos: INPE, , 2013.

PEDATELLA, N. M. Observations and simulations of the ionospheric lunar tide: Seasonal variability. **Journal of Geophysical Research: Space Physics**, v. 119, n. 7, p. 5800–5806, 2014.

PEDATELLA, N. M. et al. Impact of semidiurnal tidal variability during SSWs on the mean state of the ionosphere and thermosphere. **Journal of Geophysical Research: Space Physics**, v. 121, n. 8, p. 8077–8088, 2016.

PEDATELLA, N. M. et al. Analysis and hindcast experiments of the 2009 sudden stratospheric warming in WACCMX+ DART. **Journal of Geophysical Research: Space Physics**, v. 123, n. 4, p. 3131–3153, 2018.

PEDATELLA, N. M.; FORBES, J. M. Evidence for stratosphere sudden warming-ionosphere coupling due to vertically propagating tides. **Geophysical Research Letters**, v. 37, n. 11, 2010.

PEDATELLA, N. M.; LIU, H.-L.; RICHMOND, A. D. Atmospheric semidiurnal lunar tide climatology simulated by the Whole Atmosphere Community Climate Model. **Journal of Geophysical Research: Space Physics**, v. 117, n. A6, 2012.

PILLAT, V. G. et al. A computational tool for ionosonde CADI's ionogram analysis. **Computers & geosciences**, v. 52, p. 372–378, 2013.

PILLAT, V. G.; GUIMARÃES, L. N. F. Identificação de traços ionosféricos em ionogramas para ionossondas localizadas em baixas latitudes e região equatorial utilizando lógica nebulosa. [s.d.].

PRÖLSS, G. W. Density perturbations in the upper atmosphere caused by the dissipation of solar wind energy. **Surveys in Geophysics**, v. 32, p. 101–195, 2011.

RAJA RAO, K. S.; JEEVANANDA REDDY, S. Variation of lunar and solar geomagnetic tides with sunspot and geomagnetic activity. **pure and applied geophysics**, v. 111, p. 2291–2299, 1973.

RAMKUMAR, T. K. et al. Observational evidences on the influences of tropical lower atmospheric~ 20 day oscillation on the ionospheric equatorial electrojet. **Journal of atmospheric and solar-terrestrial physics**, v. 68, n. 3–5, p. 523–538, 2006.

RAO, J. et al. The stratospheric sudden warming event in February 2018 and its prediction by a climate system model. **Journal of Geophysical Research: Atmospheres**, v. 123, n. 23, p. 13–332, 2018.

RAO, K. S. R.; SIVARAMAN, K. R. Lunar geomagnetic tides at Kodaikanal. **Journal of Geophysical Research**, v. 63, n. 4, p. 727–730, 1958.

RAYLEIGH, LORD. XVII. On the vibrations of an atmosphere. **The London, Edinburgh, and Dublin Philosophical Magazine and Journal of Science**, v. 29, n. 177, p. 173–180, 1890.

RAYNER, J. N. Spectral Analysis. Em: SMELSER, N. J.; BALTES, P. B. (Eds.). **International Encyclopedia of the Social & Behavioral Sciences**. Oxford: Pergamon, 2001. p. 14861–14864.

REDDY, C. A. The equatorial electrojet. **Pure and Applied Geophysics**, v. 131, p. 485–508, 1989.

RIABOVA, S.; SPIVAK, A. **Features of atmospheric tide according to the Geophysical observatory Mikhnevo**. IOP Conference Series: Earth and Environmental Science. **Anais**...2019.

RISHBETH, H.; MENDILLO, M. Patterns of F2-layer variability. **Journal of Atmospheric and Solar-Terrestrial Physics**, v. 63, n. 15, p. 1661–1680, 2001.

ROSSBY, C.-G. Relation between variations in the intensity of the zonal circulation of the atmosphere and the displacements of the semi-permanent centers of action. **J. mar. Res.**, v. 2, p. 38–55, 1939.

SABINE, E. V. On the lunar atmospheric tide at St. Helena. **Philosophical Transactions of the Royal Society of London**, n. 137, p. 45–50, 1847.

SANDFORD, D. J. et al. The lunar tides in the Antarctic mesosphere and lower thermosphere. **Journal of atmospheric and solar-terrestrial physics**, v. 69, n. 17–18, p. 2219–2237, 2007.

SANDFORD, D. J.; MULLER, H. G.; MITCHELL, N. J. Observations of lunar tides in the mesosphere and lower thermosphere at Arctic and middle latitudes. **Atmospheric Chemistry and Physics**, v. 6, n. 12, p. 4117–4127, 2006.

SCARGLE, J. D. Studies in astronomical time series analysis. II-Statistical aspects of spectral analysis of unevenly spaced data. **Astrophysical Journal, Part 1, vol. 263, Dec. 15, 1982, p. 835-853.**, v. 263, p. 835–853, 1982.

SCHLAPP, D. M. Lunar daily geomagnetic variations at Tucson. **Geophysical Journal International**, v. 55, n. 1, p. 183–191, 1978.

SCHLAPP, D. M.; MALIN, S. R. C. Some features of the seasonal variation of geomagnetic lunar tides. **Geophysical Journal International**, v. 59, n. 1, p. 161–170, 1979.

SIDDIQUI, T. A. et al. **On the variability of the semidiurnal solar and lunar tides of the equatorial electrojet during sudden stratospheric warmings**. Annales Geophysicae. **Anais**...2018.

SIEBERT, M. Atmospheric tides. Em: **Advances in geophysics**. [s.l.] Elsevier, 1961. v. 7p. 105–187.

SMITH, A. K.; PERLWITZ, J. Middle atmosphere| planetary waves. 2015.

STENING, R. J. Lunar effects in the F region of the ionosphere. **Journal of Geophysical Research: Space Physics**, v. 91, n. A4, p. 4581–4584, 1986.

STENING, R. J. et al. Experiments with a lunar atmospheric tidal model. **Journal of Geophysical Research: Atmospheres**, v. 102, n. D12, p. 13465–13471, 1997.

STENING, R. J.; FEJER, B. G. Lunar tide in the equatorial F region vertical ion drift velocity. **Journal of Geophysical Research: Space Physics**, v. 106, n. A1, p. 221–226, 2001.

STENING, R. J.; RASTOGI, R. G. Variations of the lunar geomagnetic tide in the Indian region. **Journal of atmospheric and solar-terrestrial physics**, v. 64, n. 4, p. 471–477, 2002.

STENING, R. J.; VINCENT, R. A. A measurement of lunar tides in the mesosphere at Adelaide, South Australia. **Journal of Geophysical Research: Space Physics**, v. 94, n. A8, p. 10121–10129, 1989.

SUGIURA, M. **Hourly values of equatorial Dst for the IGY. Annual International Geophysical Year, vol. 35**. Pergamon, New York, , 1964.

TAKAHASHI, H. et al. Evidence on 2–4 day oscillations of the equatorial ionosphere h′ F and mesospheric airglow emissions. **Geophysical Research Letters**, v. 32, n. 12, 2005.
TAPPING, K. F. The 10.7 cm solar radio flux (F10. 7). **Space weather**, v. 11, n. 7, p. 394–406, 2013.

TARPLEY, J. D. The ionospheric wind dynamo—I: Lunar tide. **Planetary and Space Science**, v. 18, n. 7, p. 1075–1090, 1970.

TARPLEY, J. D. The O1 component of the geomagnetic lunar daily variation. **Journal of geomagnetism and geoelectricity**, v. 23, n. 2, p. 169–179, 1971.

TARPLEY, J. D.; BALSLEY, B. B. Lunar variations in the Peruvian electrojet. **Journal of Geophysical Research**, v. 77, n. 10, p. 1951–1960, 1972.

THAYAPARAN, T. The terdiurnal tide in the mesosphere and lower thermosphere over London, Canada (43 N, 81 W). **Journal of Geophysical Research: Atmospheres**, v. 102, n. D18, p. 21695–21708, 1997.

THOMSON, W. 2. On the thermodynamic acceleration of the Earth's rotation. **Proceedings of the Royal Society of Edinburgh**, v. 11, p. 396–405, 1882.

TITHERIDGE, J. E. Winds in the ionosphere—A review. **Journal of Atmospheric and Terrestrial Physics**, v. 57, n. 14, p. 1681–1714, 1995.

TORRENCE, C.; COMPO, G. P. A practical guide to wavelet analysis. **Bulletin of the American Meteorological society**, v. 79, n. 1, p. 61–78, 1998.

TUNG, K. K.; LINDZEN, R. S. A theory of stationary long waves. Part I: A simple theory of blocking. **Monthly Weather Review**, v. 107, n. 6, p. 714–734, 1979.

VIAL, F.; FORBES, J. M. Monthly simulations of the lunar semi-diurnal tide. **Journal of Atmospheric and Terrestrial Physics**, v. 56, n. 12, p. 1591–1607, 1994.

VIEIRA, F. et al. Ionospheric disturbances over the American and African sectors due to the 2019 major Sudden Stratospheric Warming (SSW 2019), under low solar activity conditions. **Journal of Atmospheric and Solar-Terrestrial Physics**, v. 240, p. 105945, 2022.

VINEETH, C. et al. Atmosphere-Ionosphere coupling observed over the dip equatorial MLTI region through the quasi 16-day wave. **Geophysical research letters**, v. 34, n. 12, 2007.

VOLLAND, H. **Atmospheric tidal and planetary waves**. [s.l.] Springer Science & Business Media, 1988. v. 12

WOOLLINGS, T. et al. Associations between stratospheric variability and tropospheric blocking. **Journal of Geophysical Research: Atmospheres**, v. 115, n. D6, 2010.

WU, C.-C. et al. The 04–10 September 2017 Sun–Earth connection events: solar flares, coronal mass ejections/magnetic clouds, and geomagnetic storms. **Solar Physics**, v. 294, p. 1–19, 2019.

XIONG, J. et al. Planetary wave-type oscillations in the ionosphere and their relationship to mesospheric/lower thermospheric and geomagnetic disturbances at Wuhan (30.6 N, 114.5 E). **Journal of atmospheric and solar-terrestrial physics**, v. 68, n. 3–5, p. 498–508, 2006.

YAMAZAKI, Y. Solar and lunar ionospheric electrodynamic effects during stratospheric sudden warmings. **Journal of Atmospheric and Solar-Terrestrial Physics**, v. 119, p. 138–146, 2014.

YAMAZAKI, Y. Solar and lunar daily geomagnetic variations and their equivalent current systems observed by Swarm. **Earth, Planets and Space**, v. 74, n. 1, p. 99, 2022.

YAMAZAKI, Y.; DIÉVAL, C. Modeling of Planetary Wave Influences on the Pre-reversal Enhancement of the Equatorial F Region Vertical Plasma Drift. **Space Weather**, v. 19, n. 4, p. e2020SW002685, 2021.

YAMAZAKI, Y.; MAUTE, A. Sq and EEJ—A review on the daily variation of the geomagnetic field caused by ionospheric dynamo currents. **Space Science Reviews**, v. 206, n. 1–4, p. 299–405, 2017.

YIĞIT, E. et al. A review of vertical coupling in the Atmosphere–Ionosphere system: Effects of waves, sudden stratospheric warmings, space weather, and of solar activity. **Journal of Atmospheric and Solar-Terrestrial Physics**, v. 141, p. 1–12, 2016.

YIĞIT, E. **Atmospheric and Space Sciences: Ionospheres and Plasma Environments: Volume 2**. [s.l.] Springer, 2017.

YIZENGAW, E.; CARTER, B. A. **Longitudinal, seasonal and solar cycle variation in lunar tide influence on the equatorial electrojet**. Annales Geophysicae. **Anais**...2017.

ZECHMEISTER, M.; KÜRSTER, M. The generalised Lomb-Scargle periodogram-a new formalism for the floating-mean and Keplerian periodograms. **Astronomy & Astrophysics**, v. 496, n. 2, p. 577–584, 2009.

ZHANG, X.; FORBES, J. M. Lunar tide in the thermosphere and weakening of the northern polar vortex. **Geophysical Research Letters**, v. 41, n. 23, p. 8201–8207, 2014.

APPENDIX

APPENDIX A – SOLAR TIDAL COMPONENTS FOR FEBRUARY 2018

The solar tidal components obtained from the analysis in section 4.1.3 are presented in this section.

A.1 DIURNAL TIDE

Figure A.1

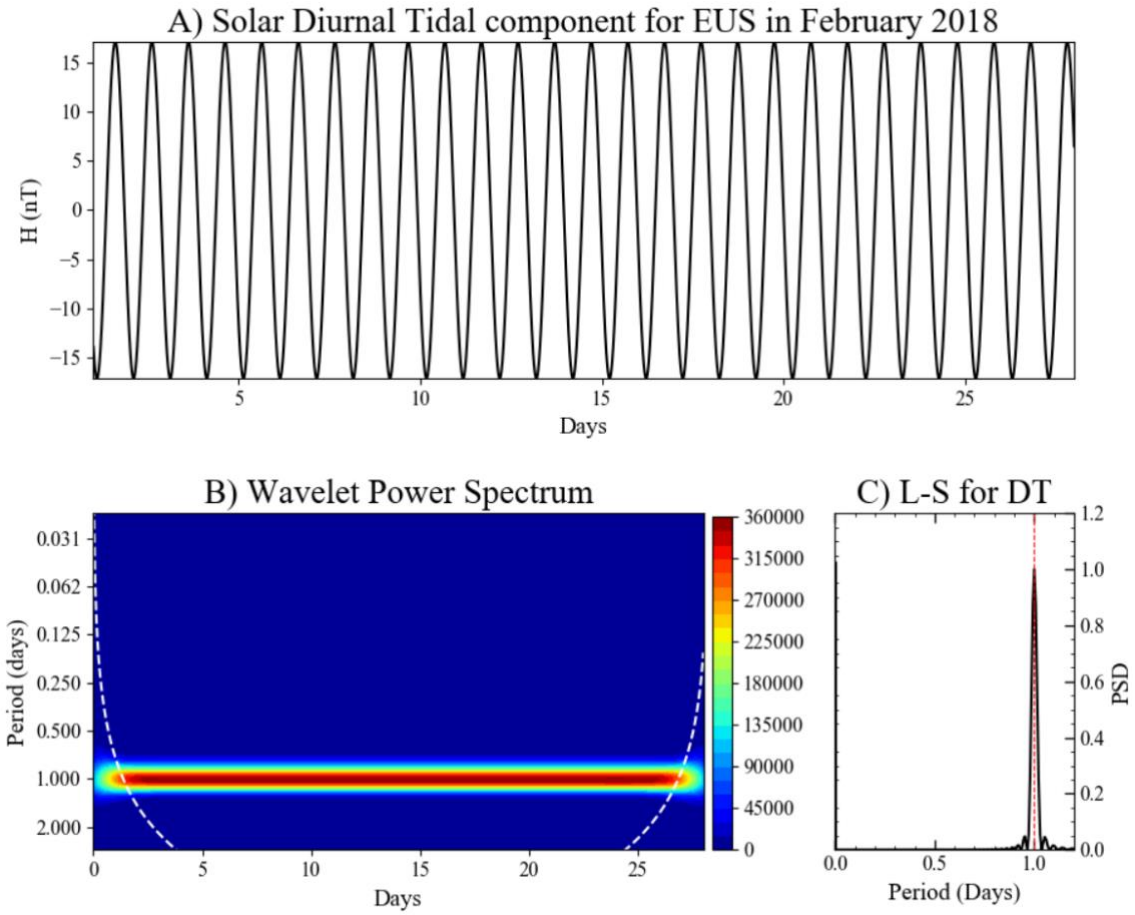

Source: Author

A.2 SEMIDIURNAL TIDE

Figure A.2

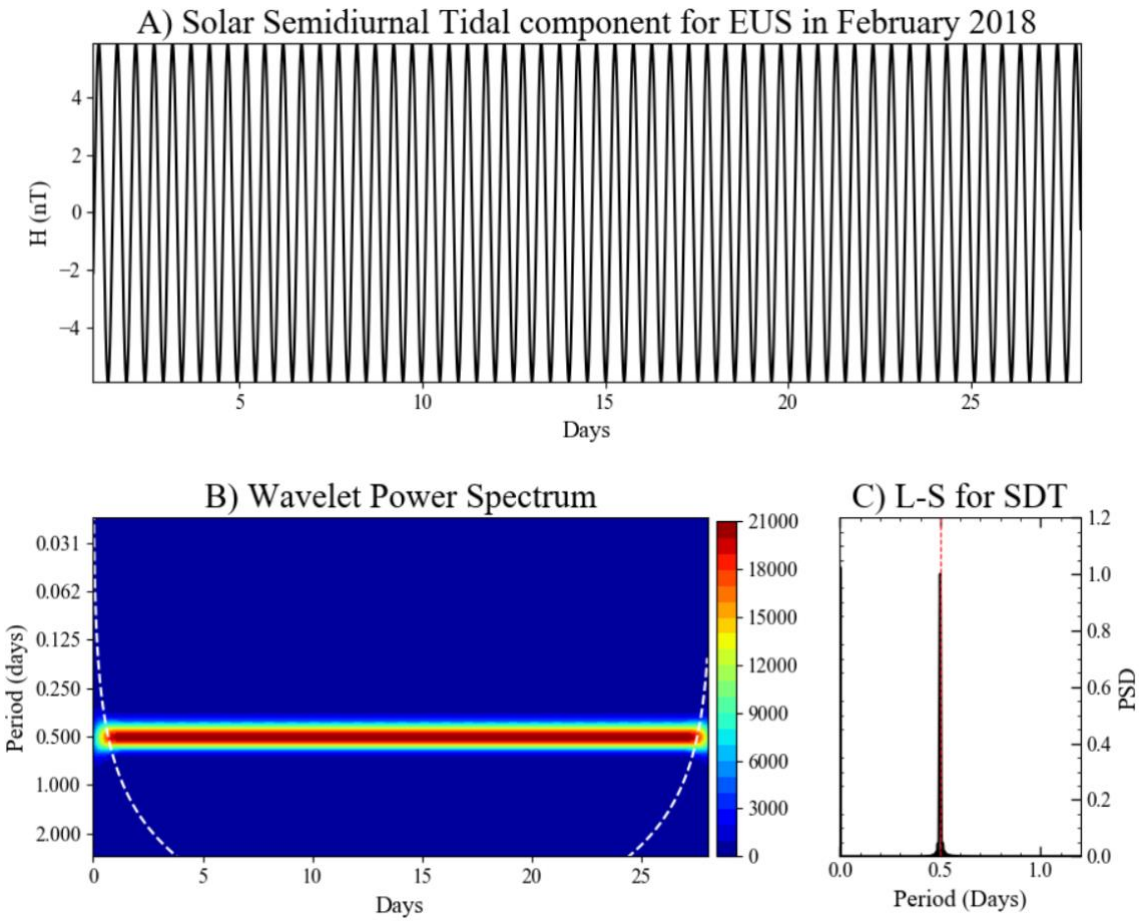

Source: Author

A.3 TERDIURNAL TIDE

Figure A.3

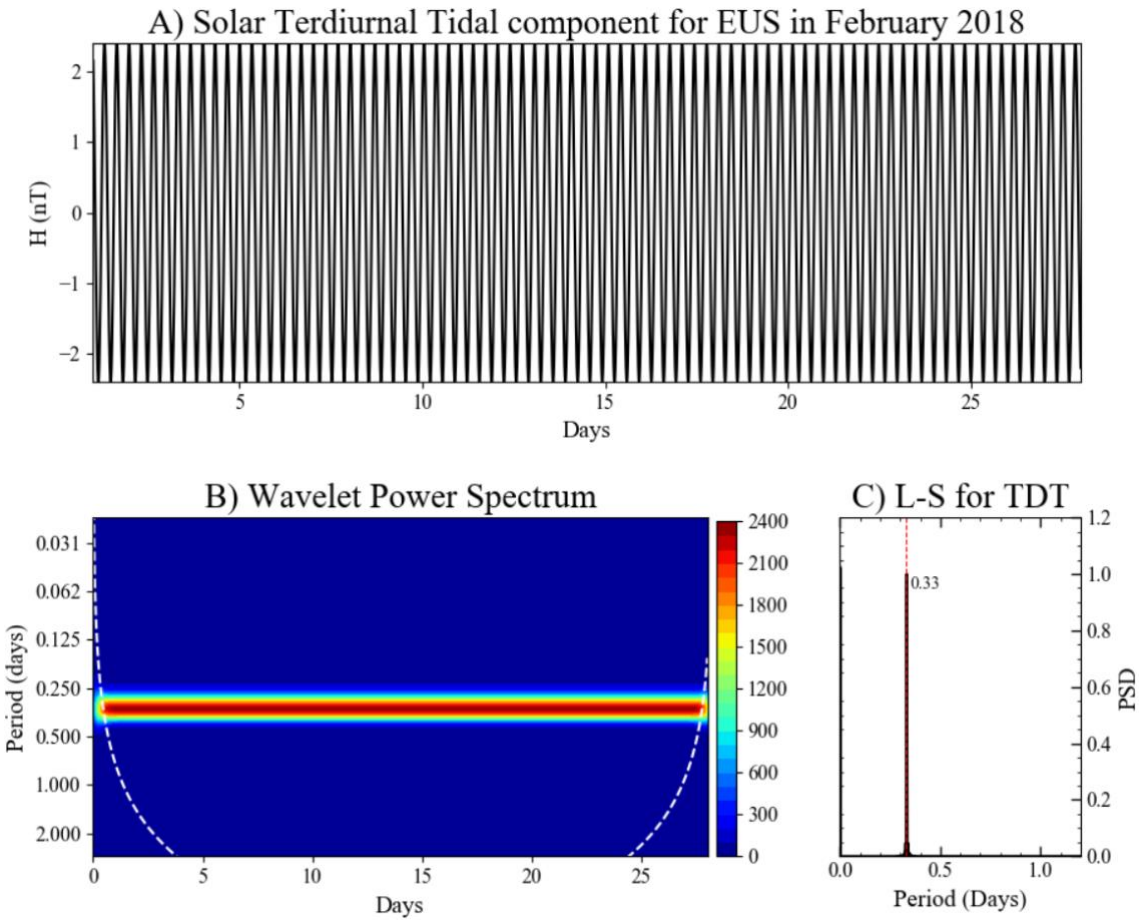

Source: Author

APPENDIX B – PERIODICITIES AT 3 STATIONS (AVERAGED) IN 2018

The LS for the ΔH daily average variation at evening (18:00LT) from September to December 2018 the (A) Brazilian and (B) African sectors from the wavelet analysis in section 4.1.4 are presented in this section.

B.1 BRAZILIAN SECTOR

LS Periodograms of averaged dataset from EUS, SLZ, and SJC at 18LT are shown in Figures B.1 A, B, C, and D.

Figure B.1

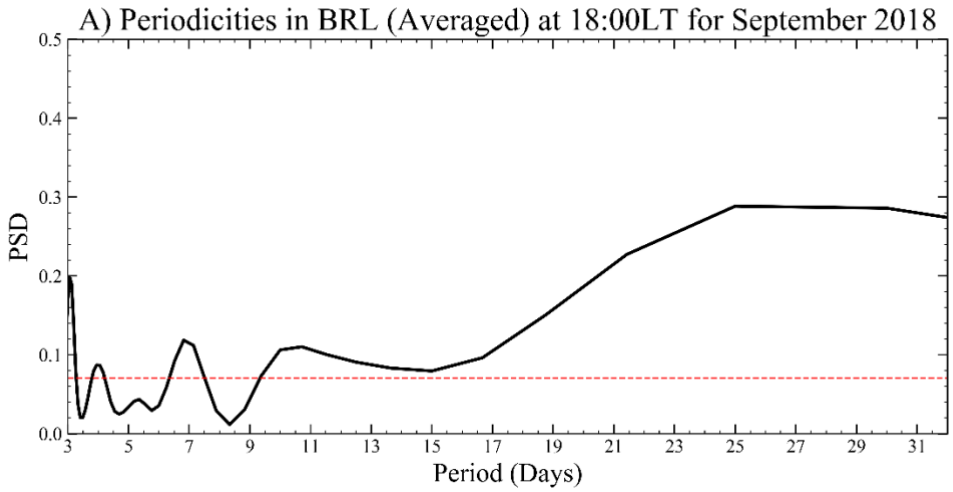

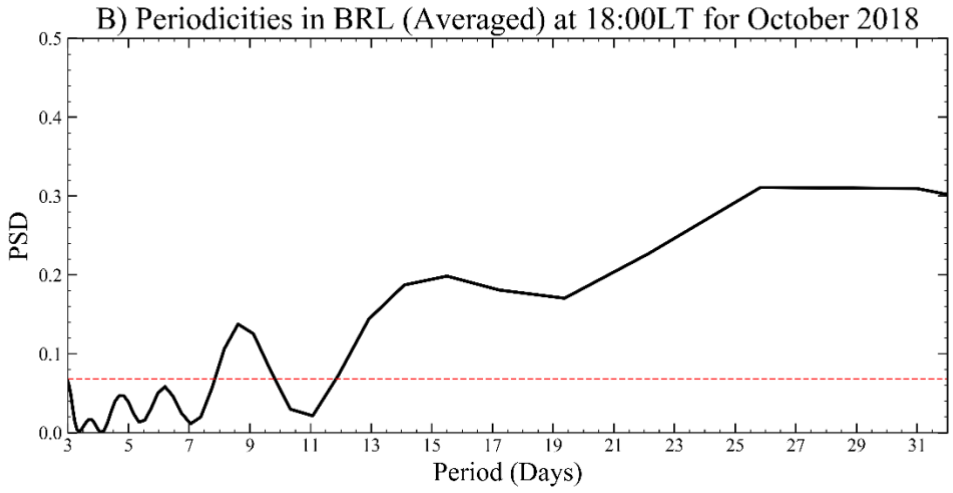

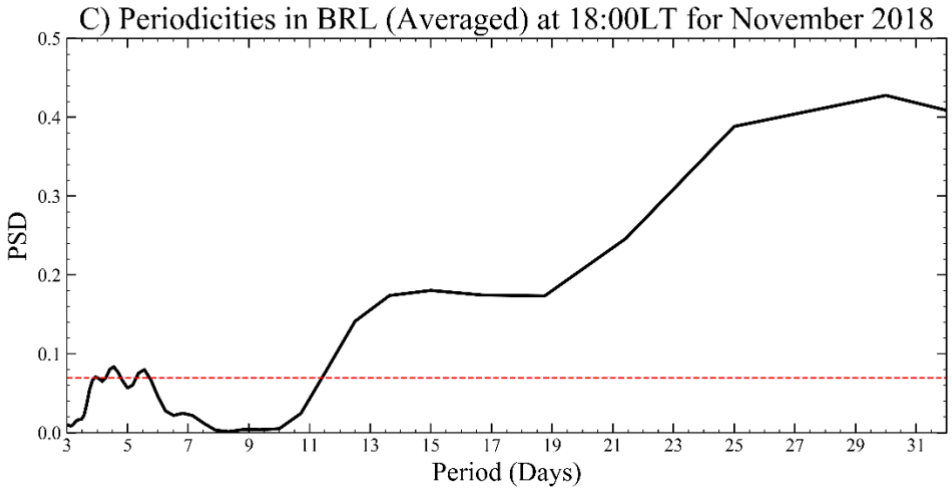

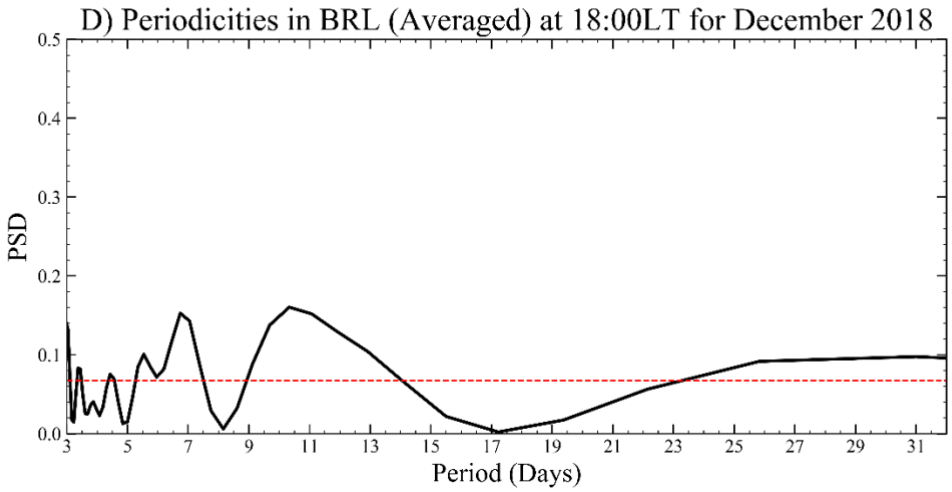

Source: Author

B.2 AFRICAN SECTOR

LS Periodograms of averaged dataset from TAM, TSU, and HER at 18LT are presented in Figures B.2 A, B, C, and D.

Figure B.2

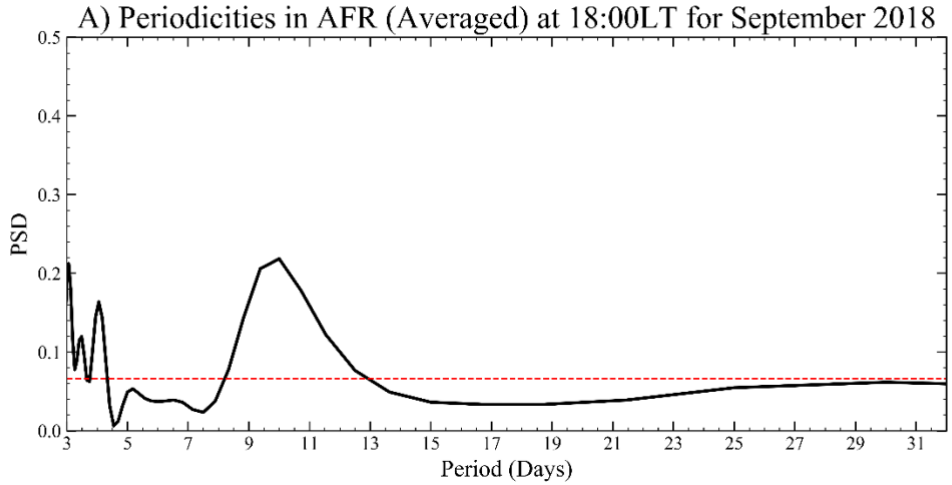

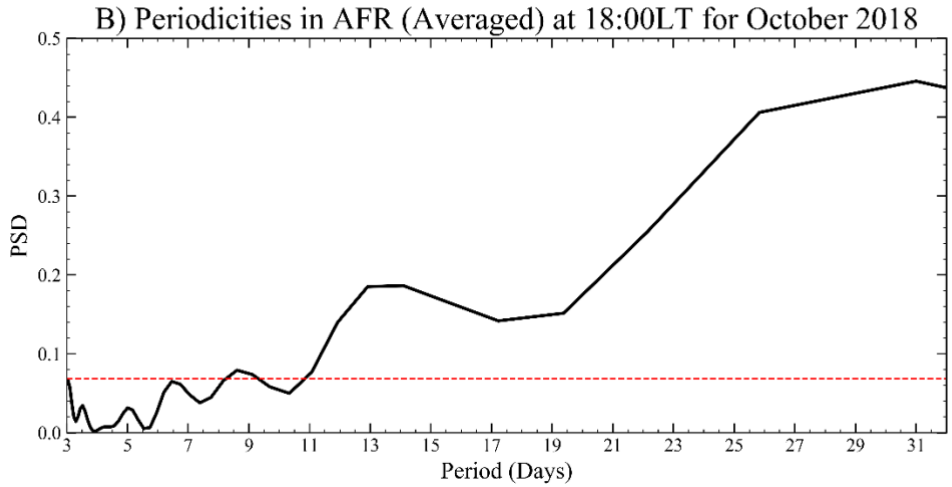

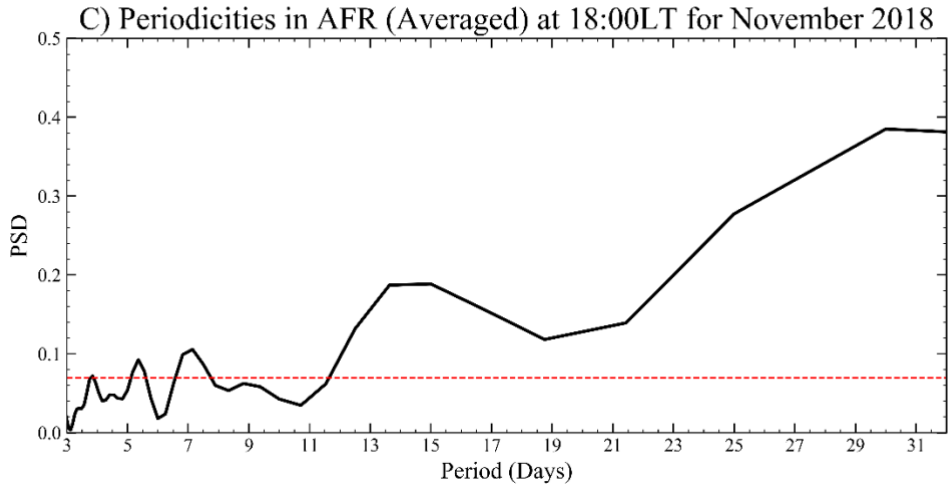

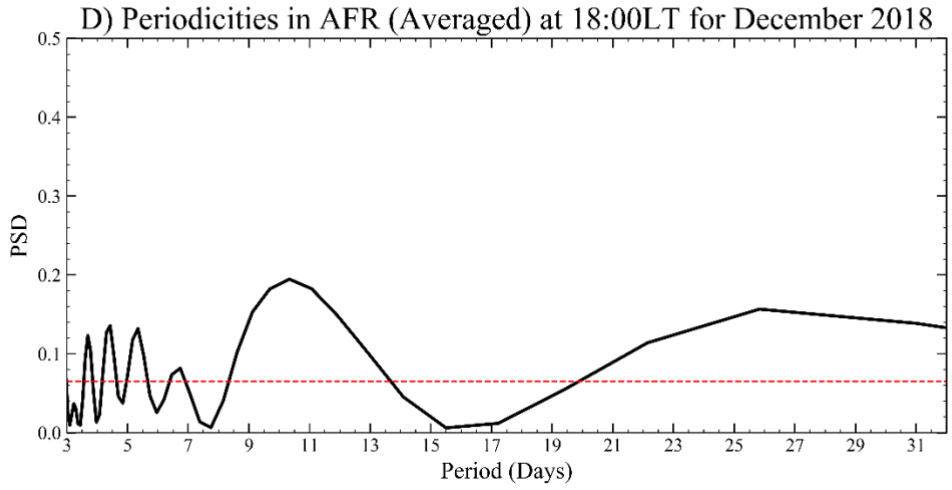

Source: Author